Relationships Between Structure, Dynamics, and Flow in Sheared Amorphous Materials

Kevin Lawrence Galloway

A DISSERTATION
in
Mechanical Engineering and Applied Mechanics
Presented to the Faculties of the University of Pennsylvania
in
Partial Fulfillment of the Requirements for the
Degree of Doctor of Philosophy
2022

Supervisors of Dissertation:

Paulo E. Arratia, Professor of Mechanical Engineering and Applied Mechanics

Douglass J. Jerolmack, Professor of Earth and Environmental Science & Mechanical Engineering and Applied Mechanics

Graduate Group Chairperson:

Jennifer R. Lukes, Professor of Mechanical Engineering and Applied Mechanics

Dissertation Committee:
Paulo E. Arratia, Professor of Mechanical Engineering and Applied Mechanics
Douglass J. Jerolmack, Professor of Earth and Environmental Science & Mechanical Engineering and Applied Mechanics
Robert Carpick, Professor of Mechanical Engineering and Applied Mechanics
Danielle Bassett, Professor of Bioengineering

Relationships Between Structure, Dynamics, and Flow in Sheared Disordered Materials

COPYRIGHT

2022

Kevin Lawrence Galloway

To Nana

ACKNOWLEDGEMENTS

I would like to express my deepest appreciation to my advisor, Professor Paulo Arratia, whose creativity, unparalleled support, and practical suggestions cannot be overstated. I also want to extend my deepest gratitude to my second advisor, Professor Doug Jerolmack for his profound belief in my work. I am grateful to the faculty of the Mechanical Engineering department; particularly Professor Celia Reina for her fantastic lectures and mastery of details. I also wish to thank the Mechanical Engineering department staff, particularly Maryeileen Griffith and Peter Litt for assisting in my transition to and from graduate school.

Special thanks to the wonderful group of students and postdocs that I have been lucky to be a part of while at the University of Pennsylvania. In particular I thank Dr. Sebastien Kosgodagan Acharige, Dr. David Gagnon, and Dr. Boyang Qin for instilling thoughtfulness and a joy of exploring reality *via* science. In addition I appreciate Ranjiangshang Ran for his boundless vigor and superb ideas, Bryan Torres Maldonado for his inspiring patience and discipline, and Juliette Sardin for making Penn brighter and more rewarding. I thank Nakul Deshpande for his sense of humor and wit.

I have been lucky to have many phenomenal collaborators outside of the Mechanical Engineering department and the Arratia and Jerolmack groups. Professor Arjun Yodh deserves many repeated thanks for his wisdom and curiosity, which have opened entire avenues of research that I would have not explored had it not been for him. I am indebted to Professor Danielle Basset and Dr. Erin Teich for their methodical approach to data exploration, from which I learned a great deal.

I thank my parents and brother for a lifetime of love and support. I thank my fiancee Olivia for always believing in me when I doubted myself.

ABSTRACT

RELATIONSHIPS BETWEEN STRUCTURE MEMORY AND FLOW IN SHEARED AMORPHOUS MATERIALS

Kevin Lawrence Galloway
Paulo Arratia

Amorphous solids, those composed of haphazardly arranged constituents, are found everywhere from our windows as silicate glass, in the ground and foundations as mud and concrete, and our grocery stores as granular piles of oranges. Even though they can be found over a huge range of length scales, it remains a challenge to systematically design their mechanical properties using knowledge of their microstructure. In this thesis, I investigate the link between the microstructure and the mechanical properties of a-thermal solids. First, I probe the particle trajectories for chaotic signatures that relate to bulk rheology. Particles are confirmed to exhibit chaotic, Brownian like motion during cyclic shear, even though the particles are large enough that thermal motion is negligible. I also find that, the average area traced by returning particles is proportional to the amplitude of strain, which could be useful for *in situ* measurements in industrial, granular, mixing applications. Next, I examine the interconnection between particle dynamics and the arrangements of the constituents. I calculate the characteristic time for particles to shift past each other, called relaxation time, and the configurational entropy of the system in excess of a reference ideal gas. I show that the relaxation time at any given instant is related to the excess entropy a quarter shear cycle later, which implies that the dynamics of particles shape the eventual structure. This means it is possible to take a snapshot of particle positions and infer its mechanical past. Finally, I focus on the interplay between particle positions and bulk yield by using concepts from kinetics, thermodynamics, statistical mechanics, and shear transformation zone theory. I establish a relationship between excess entropy and energy dissipation and uncover a novel definition for the yield transition based on memory signatures within the microstructure. Using these observations, I derive a phenomenological model that links the microstructure to bulk rheology that is physically informed and whose parameters are all quantitatively measurable. This dissertation elucidates how the statistics of particle configurations and dynamics give rise to the macroscopic transition from elasticity to plasticity during yield of amorphous, a-thermal solids.

Contents

Acknowledgments **iv**

Abstract **v**

List of Tables **viii**

List of Figures **ix**

1 Introduction **1**
1.1 Introduction and motivation 1
1.2 Background 7
1.2.1 Suspension rheology and interfacial colloids 7
1.2.2 Models and insights linking microstructure to bulk behavior . 14
1.3 Thesis Overview 22

2 A statistical connection between the dynamics of individual particles and the onset of yield **24**
2.1 Introduction 24
2.2 Methods 27
2.3 Results 32
2.4 Discussion and Conclusions 41
2.5 Appendix 43

3 The system wide link between particle arrangements and their dynamical responses **46**
3.1 Introduction 46
3.2 Results and Discussion 48
3.3 Conclusion 58
3.4 Methods 59
3.4.1 Interfacial stress rheometer 59
3.4.2 Sample preparation 59
3.4.3 Affine and nonaffine particle motions 60
3.4.4 Calculation of $\langle|\dot{\Gamma}|\rangle_{\delta t}$ 61
3.4.5 Evaluation of Δt and t_d 61

4 The relation between system composition and its stress response throughout yield 62
4.1 Introduction 62
4.2 Results 64
4.3 Conclusion 74
4.4 Methods 75
4.4.1 Experiments 75
4.4.2 Simulations 77
4.5 Appendix 78
4.5.1 Discussion of systems 78
4.5.2 Scaling of imposed force and non-affine events 78
4.5.3 Experimental potentials 79
4.5.4 Phenomenological derivation 82

5 Summary & Perspectives 94
5.1 Summary 94
5.2 Future recommendations 96
5.3 Perspectives 98

Bibliography 99

List of Tables

2.1 A summary of the properties of the systems presented here, including dispersity, particle size ratios, sizes of particles, area fractions, Φ. . . 29

3.1 Summary of colloidal monolayers. σ: particle diameter, ϕ: packing fraction, d: mean interparticle separation, Γ_{max}: strain amplitude . . 48

4.1 A summary of the properties of the systems presented, including variety of inter-particle force, particle dispersity, particle sizes, spatial density of particles, ϕ, and simple area fractions of particles, Φ. We note, particles are point particles in simulations, C; hence, diameters are not defined in system C. 76

List of Figures

1.1 Elasticity of many materials relative to their density. Glass has a high elasticity but yields at low strains. Adapted from [7] 2

1.2 Demonstration of the difference between crystalline and amorphous materials. a) Particles within a crystal align in repeating patterns. Particles within a polycrystal align with their neighbors within grains. Grains have boundaries. Particles within amorphous packings do not align. b) An example of grains and grain boundaries within a metallic alloy. Micrograph created by Edward Pleshakov and generously published on wikimedia [49]. c) An example of an amorphous microstructure formed in a metallic alloy [225]. 3

1.3 a-d) Example images of amorphous packings ranging in size from tens of nanometers to centimeters. a) Chalk placed between containment walls and acted upon by gravity. Image taken by the author. b) An image of sand grains placed in the public domain on wikimedia [48]. c) An image of an interfacial colloidal suspension [107]. d) A packing of silica nanoparticles coated with alumina [50]. e) A compendium of amorphous materials and their yield stress plotted against Young's modulus [50]. Approximately, a 3% yield strain is shown to hold across many orders of magnitude. 5

1.4 The hitchhiker's guide to complex fluids by Gareth McKinley [145]. The subclass of amorphous solids resides in the lower left sector. . . . 8

1.5 a) An example schematic of a cone and plate rheometer. The fluid resides between the cone and plate. The cone rotates, deforming the fluid. Either the strain is imposed and the torque is measured, or *visa-versa*. G'' and G' are calculated *via* the methods outlined in the text. Reproduced from [136]. b-c) Example G'' and G' as a function of frequency ω. Reproduced from [136]. 9

1.6 An example schematic of an interfacial stress rheometer. A magnetic rod sits between two walls at a water-air interface. The rod is pushed axially by an oscillating magnetic field generated by two Helmholtz Coils. The displacement of the needle is measured from below with a microscope. The rheological properties are calculated from the known imposed force, and the measured displacement using the methods described in the text. Reproduced from [35]. 11

1.7 An example of the greater free volume available to crystalline grains versus an amorphous packing. An illustration of how crystals have a higher entropy and a higher maximum density. Reproduced from [122]. 15
1.8 a-c) Examples of the chaotic motions that non-Brownian particles within an amorphous packing exhibit when undergoing shear deformation. a) Simulations of a-thermal cyclically sheared amorphous packings. Reproduced from [180] b) Experiments of non-Brownian colloidal particles at an interface undergoing cyclic shear. Reproduced from [106]. 16
1.9 a) The load-density-jamming phase-state diagram for amorphous materials. Along the temperature-density plane, glass exists at high density and low temperature. Once temperature is raised or density falls a glass will melt. Crystallization of glasses will occur at various rates. Along the load-density plane a similar phenomenon is observed: a packing will become un-jammed with increasing load or decreasing density. Reproduced from [126]. b) Over many tens of thousands of cyclic shear cycles the density of an amorphous solid composed of non-Brownian hard spheres will plateau to the value of random close packing. However, after hundreds of thousands of further cycles, the density will begin to increase again. c) As the density increases past the random close pack, crystals are observed forming homogeneously within the amorphous solid. Reproduced from [186] 17
1.10 Example packings and their corresponding radial distribution functions. a) Within the radial distribution function, a crystal has narrow peaks at positions determined by the pattern. b) An amorphous material has much more position variation around first neighbors and second neighbors. Gasses have very high variance in positions and display no layering of particles. Adapted from [40]. 21

2.1 Schematic of the system and background of data. a) Diagram of the interfacial stress rheometer including oil/water contact line pinned at the two glass walls and the axially displacing needle. b) A top view schematic with a description of coordinates and the idealized displacement field, $\delta(y,t)$. Also shown is an image of the particle microstructure representing about 1/24th of a total image. The vertical edge is $250\mu m$ long. Crystallized grain clusters may be observed, surrounded by expansive amorphous boundaries. c) Storage, G', and loss modulus, G", as a function of strain amplitude γ_0, both showing inflection at the classic yield point of ~3% (- - -). d) Characterization of the fraction of particles displaying irreversible and reversible non-affine events. The total number of reversible and irreversible events diverge at the yield point. 28

2.2 Probability density function comparisons of particle displacement after a) half cycles and b) whole cycles over a range of strain amplitude. a) Particles fall within a small displacement below yield, slowly transition to a bi-modal distribution near yield, and finally nearly all particles escape above yield. A threshold (- - -) is included, found previously in simulation studies, $0.1a = 1.15\mu m$. Inset: visual representation of when half cycles and whole cycles are taken relative to strain, γ_0. b) A separate transition is present, well above yield. Inset- the average displacement of particles that are to the right relative to strain amplitude over half and whole cycles. 30

2.3 Characterization of half cycle displacement vectors by x-y displacement Poincarè sections for three strain amplitudes. An additional attractor develops with increasing strain amplitude. Strain is increased from below yield (top), to near yield (middle), to above yield (bottom). Below yield, most particles return to their original position as expected from Fig. 2.2. Above yield, many particles do not return; their paths back to the origin are cut short, ending at periodic, chaotic points centered on the x-axis. These points grow outward with strain amplitudes above yield (~3%). This can be seen in detail for all strain amplitudes in a video within the Supplemental Information. 32

2.4 Above yield trajectories (γ_0 =6.8%). Trajectories are black with a red plus, (+), at the beginning of the cycle. For reference, local displacement is offset above in blue (–). a-b) Trajectories dominated by mechanical noise. c) A low area example of a trajectory with arc length equal to the expected displacement ($L_N = 0$). d) A high area example of a trajectory with $L_N = 1.0$. 33

2.5 Inverse normalized arc-lengths ($1/L_N$) and enclosed area (color bar) compared with the mean particle position between the needle and the wall. Irreversible particles are shown in black. a) Below yield the system is dominated by reversibly elastic, and irreversibly plastic particle trajectories. All trajectories have $1/L_N < 1.0$, indicating that trajectories are long relative to the displacement field. This means they are dominated by mechanical noise. b) Near yield, plastically reversible particles emerge near the needle. Overall the $1/L_N$ shifts nearer to one (especially the plastically reversible particles) indicating a transition to low mechanical noise relative to affine displacements. c) Particles in the middle of the channel are exclusively plastically irreversible. Plastically reversible particles reach $1/L_N \sim 1.0$ indicating that these trajectories are completely dominated by background displacement, while simultaneously enclosing high area. It is worth noting that not a single particle is observed to have a $1/L_N >> 1.0$. 34

2.6 A direct view of the efficiency space described. Normalized arc-length, L_N, is plotted against Enclosed area, A_e. Above yield clusters emerge that correspond to the reversibly plastic, in addition to the reversibly elastic cluster. Colored clouds of points demonstrate the HDBSCAN clustering algorithm employed for our data. Here, the strain amplitude is 6.8% 36
2.7 a) Cartoon representation of different particle trajectories corresponding to those shown in Fig. 2.4. b&c) Chord diagram representations of particle's inter-cycle transitions between apparent clusters within Fig. 2.5a&c. Widths of cords at either end represent the log of the numbers of particles transitioning from that state. Color of each cord corresponds to the state that has more particles transitioning. b) Below yield for both the half cycles and whole cycles there is no presence of the reversible plastic cluster. c) Above yield, half cycles exhibit a reversibly plastic cluster, whereas the whole cycles do not. The reversibly and irreversibly plastic states do not exchange particles. 38
2.8 Trends in average enclosed area and normalized arc-length as a function of strain amplitude. a) With increasing strain amplitude, average enclosed area, $\langle A_e \rangle$ grows rapidly. With strain amplitude, average normalized arc-length, $\langle L_N \rangle$, drops monotonically toward an asymptote at unity. b) Taking the square root of the ratio, $\langle A_e \rangle / \langle L_N \rangle$ we find a linear collapse between three colloidal systems of various amounts of disorder. Moreover, this collapse passes through unity at the yield point ($\gamma_0 \sim 0.3$). 39
2.9 a) Horizontal and vertical axis are a Poincarè section well above yield. Color represents a binned average of the remainder of half cycle count divided by two, shifted so that even numbers of half cycles are blue and odd half cycles are red. The left half of the attractor is composed of even half cycles and the right is made up of odd half cycles. Therefore particles must be oscillating between both points. b) The range in the the displacement of the needle in the direction normal to shear plotted against cycle, τ, for all strain amplitudes. The average difference between the highest and lowest displacement is about one here. $C = 1.04 \pm 0.15 \mu m [95\%]$ is shown as a dashed gray line (-). 44

3.1 (a) Schematic of the interfacial stress rheometer. A sinusoidal magnetic force is imparted to the interface-bound magnetic needle, which in turn introduces oscillatory shear stress at the oil-water interface. The parallel and perpendicular directions with respect to the needle motion are defined as the x- and y-axis, respectively. (b) Micrograph of bi-disperse colloidal particles at the oil-water interface from sample A. (c) Sixfold bond orientation order, ψ_6, measured from particles in (b). Colors help to indicate the lattice director (orientation) as a guide for the eye to help discern ordered and disordered domains. Dots with large size indicates $|\psi_6| > 0.9$, and small dot size indicates $|\psi_6| < 0.9$. The scale bars in (b) and (c) are 100μm. (d) A pair correlation function, $g(x, y)$, measured from particle positions in (b) exhibits strong anisotropy due to ordered domains. 49

3.2 Dynamics in sample A (a) Instantaneous shear rate, $\dot{\Gamma}(t)$, versus time, t. The solid line is the sinusoidal fit, $\dot{\Gamma}(t) = 0.096\sin(\omega t)$. (b) The self-part of the intermediate scattering function, $F_s(\tau)$, measured at the two times indicated by same-color circles (green, blue) in (a). The dashed and solid lines are fits using Eq. 3.2, with $\tau_\alpha = 0.5$ and 2.3 sec and $\beta = 1.3$ and 1.5 at $t = 16.3$ and 18.8 sec, respectively. (c) Relaxation rate, $\tau_\alpha^{-1}(t)$, versus time, t (red circles). The magnitude of shear rate, $|\dot{\Gamma}(t)|$, is also plotted (blue triangles) for phase-shift comparison. (d), The measured relaxation time, $\tau_\alpha(t + \Delta t)$, versus time-averaged shear rate, $\langle|\dot{\Gamma}(t)|\rangle_{\delta t}$, from three experiments with different $\Gamma_{\max}$ values. The solid line is the best fit using $\tau_\alpha \sim (1 + \langle|\dot{\Gamma}|\rangle_{\delta t}/0.0017)^{-1.4}$. 52

3.3 (a) Measured $g(r)$ from data taken at $t = 16.7$ and 19.2 s. The insets show the enlarged plots of the first (left inset), and the second and third peaks (right inset) of $g(r)$, respectively. (b) $S_2(t)$ versus t. $\tau_\alpha(t)$ is also plotted for comparison. The black and green arrows indicate $t = 16.7$ and 19.2 s, respectively. (c) $\tau_\alpha(t - t_d)$ is plotted versus time delay, $t_d(t) \simeq 0.3\tau_\alpha(t)$. 54

3.4 Delayed relaxation time, $\tau_\alpha(t - t_d)$, as a function of the excess entropy, $-S_2(t)$, measured from sample A with 3 different $\Gamma_{\max}$. Inset shows same data measured from sample B and C. The three data sets are fit using Eq. 3.5 with $c = 3.9 \pm 0.2(solid\ line)$, $1.0 \pm 0.1(dash - dotline)$, and $1.4 \pm 0.1(dashedline)$ for sample A, B, and C, respectively. 55

4.1 **Overview of structure, dynamics, and response.** We characterize the disordered solid bulk response to cyclic stress from evolving configurations of individual constituent particles. (a) Image of ~40,000 particles. Part of the raw image is shown (left). The scale bar is 200μm. Detected particle positions are also shown (right). For illustration, color indicates $D^2_{min,C}$, which quantifies the degree to which a particle has followed a non-affine returning trajectory (blue), or a non-affine escaping trajectory (red). The particles in this image are experiencing yield (γ_0 ~ 15.7%). (b) Quantification of the fractions of particles escaping and returning averaged over all stress cycles versus total strain amplitude. Error bars are standard deviation. Returning events rapidly increase near the yield point (γ_0 ~ 3.0%). (c) The number of particles, $Z(r)$ within a radius, r of a reference particle. The radius is expressed in units of a, the average distance between neighboring particles. Vertical dashed lines indicate the limit of the first shell of neighboring particles. Inset: radial distribution function, $g(r)$. (d) The measured strain of the material versus the imposed stress throughout a cycle. Both stress and strain are averaged stroboscopically over 25 cycles. The different ellipses correspond to separate runs at different imposed stress amplitudes. Here, the area enclosed is a result of the lag between stress and strain, which in turn quantifies the energy dissipated from the material. . 66

4.2 **Memory within microstructure.** Microstructural anisotropy reveals signatures of memory. Below yield, anisotropic orientation remains unchanged regardless of shear direction. Orientation quantifies stored memory. Above yield, anisotropic orientation reverses freely to match the direction of shear, indicating a loss of memory. (a) Radial distribution function, g(x,y,t) at a time corresponding to one quarter of the way through a shearing cycle. We fit an ellipse to the first neighbor ring. This ellipse stretches and reorients over time indicating changes in structural anisotropy of the sample. Two elliptic fits are shown at two times, t=1.25 (—) and 1.75 [cycles] (**- - -**). (b) Orientation of the sample microstructure over time as a function of strain amplitude. With increasing strain amplitude, the microstructure reorients to match the stretching axis. It first reorients completely at the yield point (3.2%). (c) Elongation quantified by the ratio of ellipse major and minor axis lengths (m/n) over time. Below yield, elongation oscillates directly with the strain; above yield, elongation oscillates with twice the frequency of strain perturbation. In b & c data are averaged strobscopically over 25 cycles. 68

4.3 **Entropy and material memories.** Variation of entropy provides means for predicting system response to a given strain amplitude. (a) Excess entropy, with the mean value subtracted, follows a sinusoidal response. Below yield, its oscillation frequency is the shear cycle frequency. At yield, the excess entropy signal has components at both the driving frequency and twice the driving frequency: the material is beginning to forget its initial state. Above yield, the entropy response oscillates almost exclusively at twice the shear cycle frequency. Black dots indicate experimental data. Red lines are fits to equation 4.1 with T as the only fitting parameter. The experimental data are averaged stroboscopically over 25 cycles. (b) Amplitudes associated with the first and second harmonics are present within the s_2 signals. Note, that the second and first harmonic amplitudes cross each other at the yield point, $\gamma_0 = 3\%$, designated by the vertical dashed line (- - -). 69

4.4 **Imposed force, microstructural excess entropy, and rheology**. a) The imposed force amplitude, F_0, normalized by the elastic force capacity, F^*, is plotted versus the excess entropy harmonic ratio, H_{s_2} (in both mono-disperse and bi-disperse experiments). A fit of the data suggests a parabolic relationship (p-value:3.14x10^{-13}, and r^2:0.989), corroborating equation 4.2. Inset: log-log. b) The increase in the ratio of loss and storage moduli, (G''/G') versus strain amplitude in both the mono-disperse and bi-disperse experiments (same legend for mono-disperse and bi-disperse experiments as panel a). Yield is signaled by the rapid increase in parameter values at about 0.03 strain amplitude. Inset: data from simulations employing Hertzian and Lennard-Jones interaction potentials. In both cases, markers are measured values and lines are predictions of equation 4.3. c) Left and right hand sides of equation 4.3. Notably, all parameters are measured. The solid diagonal line (—, slope of 1.0) represents equation 4.3. The slope of the best fit to the data is 0.981, p-value:4.43x10^{-26}, and r^2:0.944. 71

4.5 **Interfacial Stress Rheometer** Sketch of interfacial stress rheometer (ISR). Dense colloidal monolayer sits on water-oil interface that is bounded by two upright parallel glass walls. A thin magnetic needle cyclically shears the monolayer using Helmholtz coils. Accurate rheometry is obtained by tracking needle position as a function of forcing; particle tracking is used to characterize material microstructure. 79

4.6 **Disorder increasing left to right** Crystalline regions visualized via sixfold bond orientation order, Ψ_6, measured from particle positions. Size of crystals decreases from left to right, indicating an increase in disorder. Colors help to indicate the lattice director (orientation) as a guide for the eye to help discern ordered and disordered domains. Dots with large size indicate $|\Psi_6| > 0.9$, and small dot size indicates $|\Psi_6| < 0.9$. (Scale bars: $100\mu m$). a) Mono-disperse, dipole-dipole, experimental system B. b) Bi-disperse, dipole-dipole, experimental system A. c) Bi-disperse, Hertzian, simulation system D. d) Bi-disperse, Lennard-Jones, simulation system C. 80

4.7 **Imposed force scales with dissipative events.** Within the linear rheology regime studied, the fraction of particles undergoing non-affine, disspative events scales linearly with the imposed force on the system. The dashed lines (- - -) are added to guide the eye. 81

4.8 **Novel system and ensemble definitions.** A schematic of the central concepts used in the derivation: particle cages as microstates, chemical potential, and cage pressure. a) Each set of particles and their nearest neighbors, known as cages, are observable microstates of a system consistent with statistical mechanics of small systems [90]. In this way, ensembles are composed of copies of nearest neighbor cages, each subjected to the same shear state. b) A demonstration of the concept of chemical potential within this cage-microstate definition. The energy stored in a cage *via* particle interactions changes as a particle is squeezed in or out of a cage. See the accompanying Supplementary Video. c) The total energy, e_i, within cage i can be measured systematically as the total energy stored by the central particle, i, with its neighbor particles, j. Similarly the cage pressure can be calculated as the total force stored between a central particle, i, and its neighbors, j. 82

4.9 **Additional thermodynamic relations.** Demonstration of available thermodynamic definitions and Maxwell relations. a) Definition of cage pressure, F^*. b) The Maxwell relation for the double derivative of energy, E, with respect to entropy, S_2, and number of rearranging particles, N_D. Dashed lines (- - -) are equation 4.24. Solid lines (—) are fits for demonstration. 90

4.10 **Hints of kinetics.** Demonstration of an empiric, equation of state-like proportionality, which captures the kinetic relationship between temperature, T, and the fraction of particles that leave a cage, f_d. . . 91

4.11 **Memory erasure measured by thermodynamical information.** Using Landauer's principle is is possible to calculate the minimum energy required to erase a stored memory. In this plot we compare the minimum energy of erasure to the cage strain energy, $E_{strain}/S_{erasure}$, relative to the strain amplitude that the system undergoes. A peak above one near the yield point quantifies memory erasure and mirrors how close to equilibrium the system is in the cage ensemble approach. 92

Chapter 1

Introduction

1.1 Introduction and motivation

How does matter manage to flow or deform? We are taught early on that there are two distinct types of matter that all sub-types fall neatly into: fluids and solids. Fluids are materials that continuously (and noticeably) deform under an applied shear stress [151, 122]. Life requires fluids; humans live within the atmosphere, consume aqueous solutions, and are composed of a fascinating array of fluids [89]. In addition, a myriad of industrial processes require fluids; e.g. generation of electricity from heated steam [58] and the formation of many industrial products like concrete and steel [208]. Conversely, solids have been with humans from the dawn of time; we often, but not always, live on solid ground [101]. In addition, tools are made from solids such as stone, iron, bronze, and more recently steel and silicone [208]. Indeed, the built environment is composed of solids: factories, furniture, electronic devices, and much of the rest of the things we interact with every day. Solids are the opposite of fluids; they will come to rest under an applied shear. When the shear is removed elasticity returns the solid to the prior state [189].

While this solid-fluid juxtaposition is often useful, the fact is everything flows [17]; many materials flow so very slowly that it goes unnoticed in everyday life [56, 68]. The rate of flow depends on the amount of shear stress the material is subjected to.

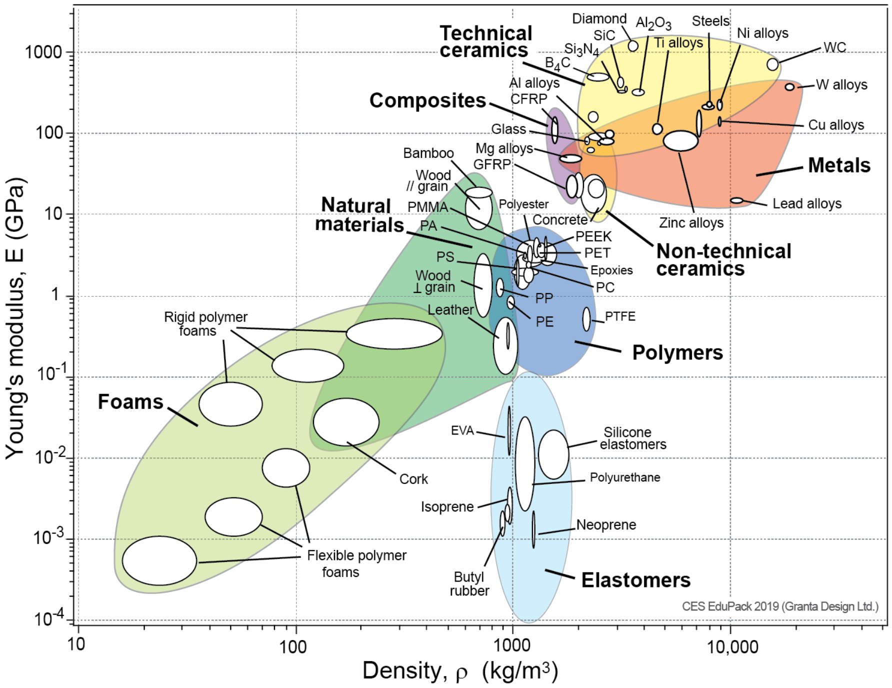

Figure 1.1: Elasticity of many materials relative to their density. Glass has a high elasticity but yields at low strains. Adapted from [7]

Above an accumulated stress threshold, flow becomes dominant, and elasticity falls by the wayside. This transition between solid-like and fluid-like behavior is called yield. Yield can occur vanishingly fast, like water flowing down a waterfall, or over extraordinarily long-time frames, such as a hill flattening over centuries[56, 68]. Many engineering applications reside between these time scales: the settling of concrete foundations [184], the creeping of plastic materials in everyday devices like cars [136], and the slow warping of load bearing wood within our houses [102, 160]. The length of time over which yield occurs depends on how quickly stress accumulates and how much the material can resist that stress. Known as plasticity, yield can also occur locally within a material, leaving other portions unscathed. Strength and ductility are both important mechanical properties related to yield. Many materials for instance display immense strength, but yield at low strain. Other materials have very little strength, but can deform elastically over vast strains before plasticity sets in. As

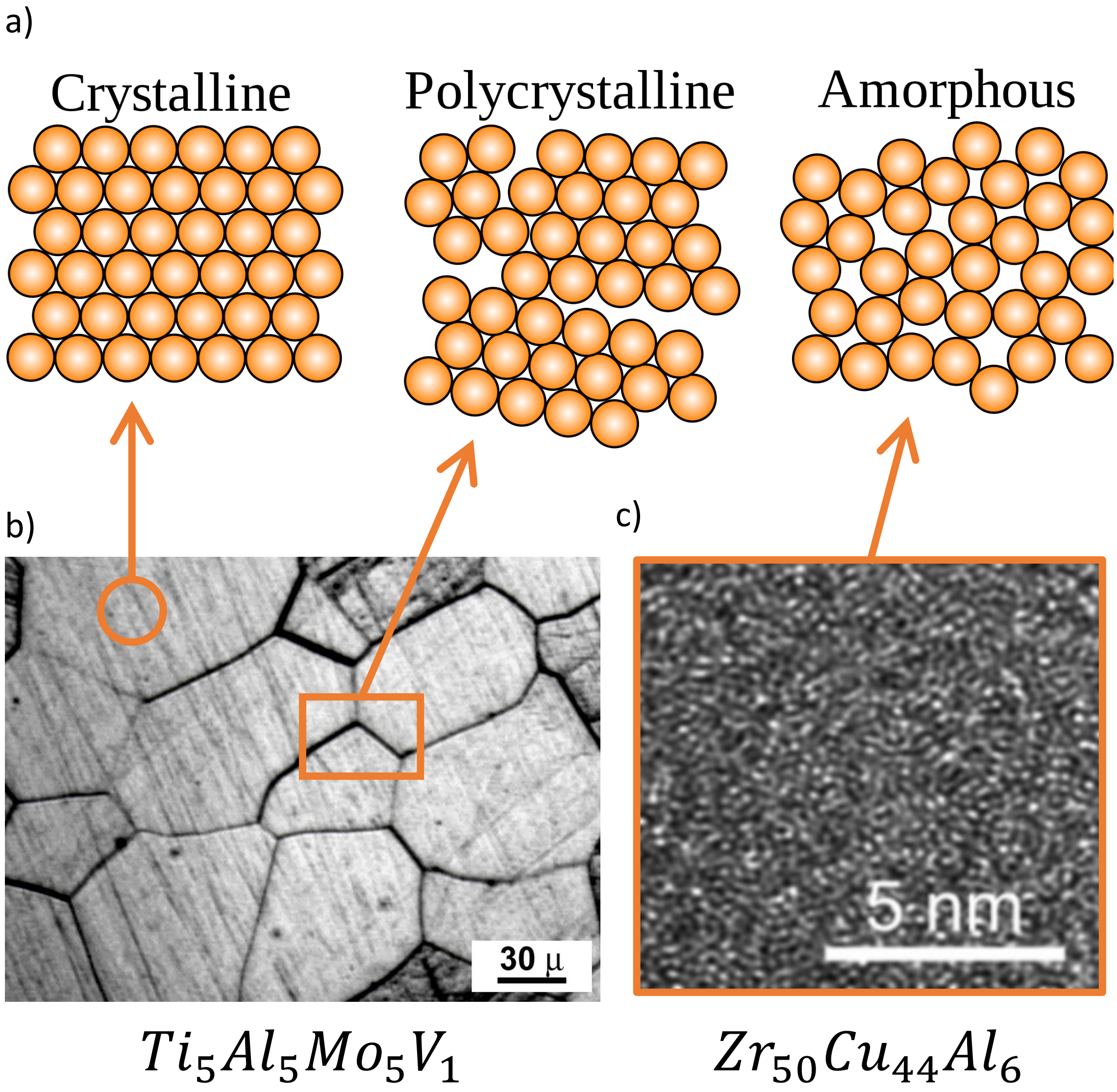
a)
Crystalline
Polycrystalline
Amorphous
b)
c)
30 μ
5 nm
$Ti_5Al_5Mo_5V_1$
$Zr_{50}Cu_{44}Al_6$

Figure 1.2: Demonstration of the difference between crystalline and amorphous materials. a) Particles within a crystal align in repeating patterns. Particles within a polycrystal align with their neighbors within grains. Grains have boundaries. Particles within amorphous packings do not align. b) An example of grains and grain boundaries within a metallic alloy. Micrograph created by Edward Pleshakov and generously published on wikimedia [49]. c) An example of an amorphous microstructure formed in a metallic alloy [225].

shown in Figure 1.1, scientists and engineers have characterized the properties of material classes.

An enormously fruitful pursuit has been the search for ways to tune the bulk mechanical response of materials by modifying the underlying micro-structure. Crystalline materials, such as steel, ice, diamond, and silicon are a well-known example [192] that is also useful for introducing some of the ideas investigated in this thesis. Within crystals the constituent particles form repeating structures. In practice, these structures tend not to be perfect. Defects arise that allow for the tuning of the material properties; some defects resist yield and ductility, while others accommodate yield and brittleness. Dislocations, which constitute an abrupt, linear mismatch within a crystal, accommodate local plasticity and yield on the bulk scale. During yield, dislocations physically travel through the material. Most other defects tend to disturb the movement of dislocations and make the material stronger. Boundaries between crystalline grains (fig. 1.2a&b), where the patterns change orientation, tend to also impede the transition of dislocations, and make for stronger, yet more brittle materials [192].

One of the major engineering advances of the 20th century was to use knowledge of microstructural defects to systematically design the properties of steel [192]. As liquid steel cools, crystals nucleate throughout. Eventually as they grow, they contact and form boundaries. Generally, the lower the cooling temperature, the more grains appear, so that a steel cooled fast will have many small grains and be much stronger, but more brittle. A steel cooled slowly will have many large grains and be more ductile. The prevalence of grain boundaries impedes the translation of dislocations and causes brittleness and high strength. By controlling the grain boundaries, strength and ductility can be traded with each other for particular applications. Crystalline solids offer an example of the power of understanding the link between microstructure and bulk mechanical properties. Knowledge about the microstructure of still other classes of materials, aside from crystals, has also been harnessed for great mechanical effect. Plastic [136] is an example. Another example is fibrous materials [102, 160]. There are however materials whose microstructures remain mysterious, such as amorphous solids.

Amorphous (also called disordered) solids are everywhere; they are found in the

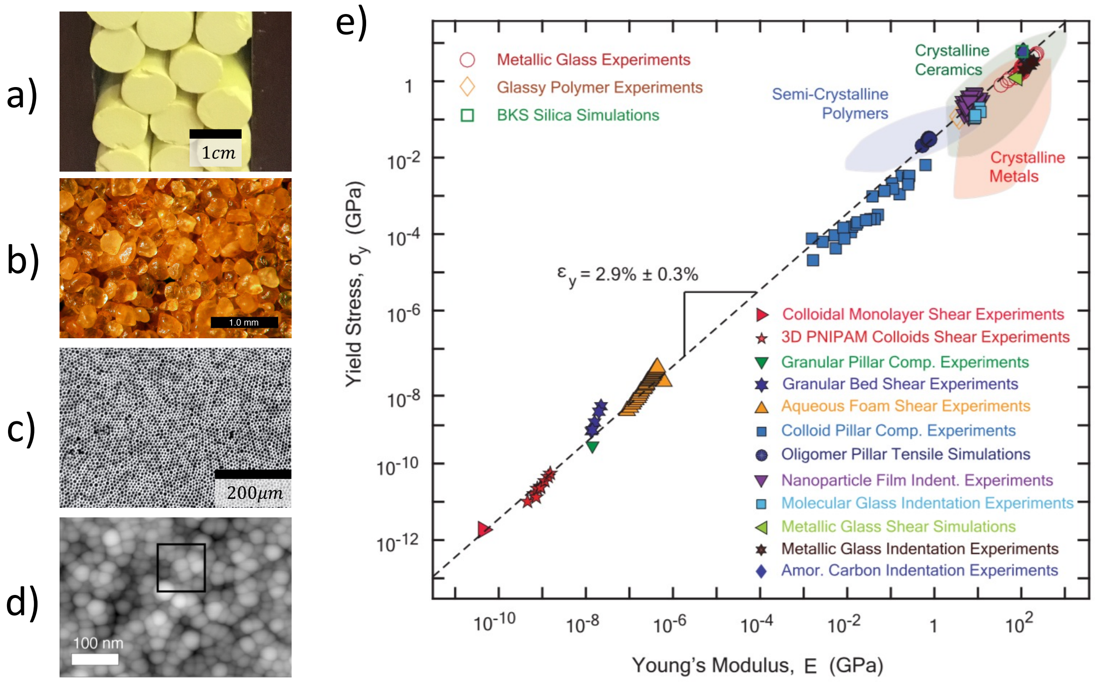

Figure 1.3: a-d) Example images of amorphous packings ranging in size from tens of nanometers to centimeters. a) Chalk placed between containment walls and acted upon by gravity. Image taken by the author. b) An image of sand grains placed in the public domain on wikimedia [48]. c) An image of an interfacial colloidal suspension [107]. d) A packing of silica nanoparticles coated with alumina [50]. e) A compendium of amorphous materials and their yield stress plotted against Young's modulus [50]. Approximately, a 3% yield strain is shown to hold across many orders of magnitude.

ground beneath our feet as mud [101]; appear in our roads in the form of concrete [97]; are present at the beach as sand dunes [12]; they compose the pills in our medicine cabinets [41]; finally, they even are in our foods [153, 28], such as chocolate [25]. Amorphous solids are not only ubiquitous, but also comprise an incredibly vast swath of mass: the total weight of concrete alone is greater than half the total weight of all known life [64]. Amorphous solids are found over a huge range of length scales, from the atomic to the granular world [50] (Fig. 1.3). Over at least the last fifty years, vigorous research has been dedicated to trying to systematically design the bulk response of amorphous solids based on microstructure. In contrast to crystals, amorphous solids exhibit no repeating pattern (fig. 1.2a&c) within the microstructure. The lack of crystalline grains means that amorphous solids tend to be stronger than their crystalline counterparts, but they fail at lower deformations. Also, they fail suddenly and without warning [50]. As a result, if amorphous solids could be designed systematically, they could be used in applications involving high loads.

There are at least two types of amorphous solid. Disorder can be achieved when the constituents have a wide range of sizes, making a crystalline pattern impossible or very unlikely. This variety of disorder is often found in granular materials, such as sand [74] and other naturally occurring particulates. A second type of disorder occurs when an amorphous material is very rapidly or haphazardly formed. This disorder can occur when dumping marbles of the same size into a container. To use the steel example from above, it can also occur when cooling a liquid extremely rapidly, such that there is simply no time for crystals to nucleate to appreciable sizes. Martensitic steel, formed from molten steel in just minutes, is strong but brittle and nearly amorphous, composed of vanishingly small crystals [192]. Fully amorphous steel alloys have been achieved recently [129]. Silicate glass is a similar example [53]. These examples are achieved by fast, random-like formation that leads to systems with no discernible, geometric patterns. Moreover, each particle finds itself constrained by its neighbors, so that they cannot slip past each other as easily as crystalline particles do. Amorphous materials tend to be very strong and very brittle because there is no mechanism for dislocations. Strength is advantageous, but in most applications amorphous materials cannot be utilized because brittle failure is catastrophic. If there was a well understood way to design the microstructure of amorphous materials, strength could be traded for ductility as is done with crystalline solids.

Without identifiable analogues of dislocations and defects, it is very difficult to design disordered solids [50]. Scientists have classified many potential local microstructural signatures for yield [185]. There are two categories that each method falls under. First, are those that classify based only on where particles are relative to each other as a means of teasing out which particles are more mobile (Shear Transformation Zone theory)[66, 67]. Second, are those that seek out correlations in particle motions to identify particles that are strongly influenced by each other (Mode Coupling Theory)[100, 34, 139]. In this way, both implicitly stem from the idea that local interactions are key to the emergence of plasticity, instead of merely a configurational pattern. Both Shear Transformation Zone and Mode Coupling Theory have had success in identifying locations within a material where local plasticity occurs [185], but so far it remains a challenge to identify *a-priori*, with a snapshot, where those local events may take place. Designing disordered materials remains difficult.

Here I review recent work on the relationships between a material's constituents, their interactions, their configurations, and bulk mechanical response. I discuss recent experiments, simulations, and theory that illuminate the connection between microstructure and macroscopic response. Finally, I identify challenges that remain and present my thesis. Herein, I investigate statistical methods for linking system wide particulate configurations and kinematics to the bulk mechanical response of sheared a-thermal materials.

1.2 Background

1.2.1 Suspension rheology and interfacial colloids

Rheology and oscillation

Rheology, the study of complex mechanical behavior, has been investigated for at least 100 years [22]. Materials with a complex microstructure, such as mud [101], suspensions[122], polymer melts [136], and foods [28] often exhibit complex mechanical behavior. As a result, apparatuses have been developed to systematically measure the response of materials to deformations. There is an extraordinarily large set of possible material responses and a huge number of types of complex materials (see Figure 1.4). The degree of viscosity and elasticity, as well as shear thinning and shear thickening (non-linearity of viscosity) can be measured in detail using a rheometer (Fig. 1.5a) so that materials can be selected for applications. Here I specifically in-

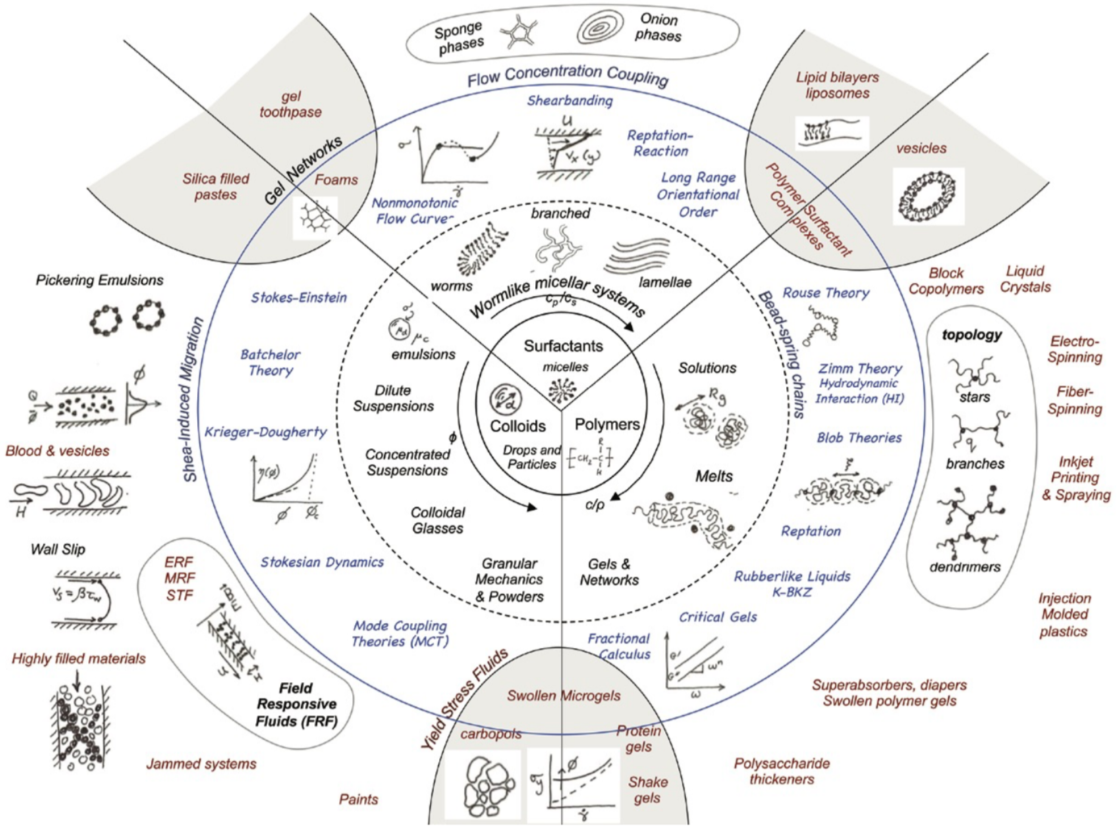
Sponge phases
Onion phases
Flow Concentration Coupling
Shearbanding
Reptation-Reaction
Long Range Orientational Order
Nonmonotonic Flow Curve
gel toothpase
Silica filled pastes
Gel Networks
Foams
Lipid bilayers liposomes
vesicles
Polymer Surfactant Complexes
Block Copolymers
Liquid Crystals
branched
worms
lamellae
Wormlike micellar systems
c_p/c_s
Surfactants
micelles
Colloids
Polymers
Drops and Particles
c/p
ϕ
Pickering Emulsions
Stokes-Einstein
Batchelor Theory
Krieger-Dougherty
Shea-Induced Migration
emulsions
Dilute Suspensions
Concentrated Suspensions
Colloidal Glasses
Solutions
Melts
Rouse Theory
Bead-spring chains
Zimm Theory Hydrodynamic Interaction (HI)
Blob Theories
Reptation
Rubberlike Liquids K-BKZ
Critical Gels
topology
stars
branches
dendrimers
Electro-Spinning
Fiber-Spinning
Inkjet Printing & Spraying
Injection Molded plastics
Blood & vesicles
H
Wall Slip
Highly filled materials
ERF MRF STF
Field Responsive Fluids (FRF)
Stokesian Dynamics
Mode Coupling Theories (MCT)
Granular Mechanics & Powders
Gels & Networks
Fractional Calculus
Yield Stress Fluids
Swollen Microgels
carbopols
Protein gels
Shake gels
Jammed systems
Paints
Superabsorbers, diapers Swollen polymer gels
Polysaccharide thickeners

Figure 1.4: The hitchhiker's guide to complex fluids by Gareth McKinley [145]. The subclass of amorphous solids resides in the lower left sector.

troduce how elasticity and viscosity are measured in experiments using a rheometer (Fig. 1.5b). I then outline the history, from invention to refinement, of the type of rheometer used in this thesis.

Both the stress within a deformed elastic solid or viscous fluid follows linear equations, known as constitutive relations [122]. Hooke's law for elasticity is $\tau = E\gamma$, where τ is the stress (typically τ indicates shear but σ indicates compression or extension), E is the elastic property intrinsic to a particular solid, and γ is the strain of the system. Conversely, Newton's law of Viscosity is $\tau = \mu\dot{\gamma}$, where μ is the viscous property intrinsic to a particular fluid and $\dot{\gamma}$ is the strain rate. Notice that the primary difference is the derivative of strain. A further intricacy is that some viscous materials have viscosity, μ, that changes with shear rate, such that $\mu = \mu(\dot{\gamma})$. There are several types of these non-Newtonian materials. For example, shear thickening

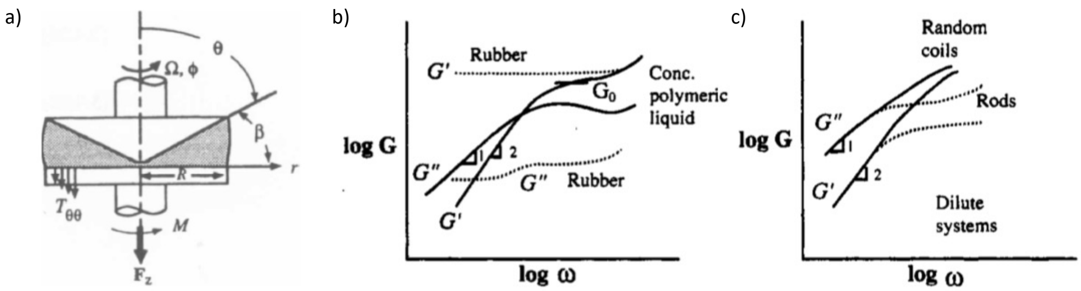

Figure 1.5: a) An example schematic of a cone and plate rheometer. The fluid resides between the cone and plate. The cone rotates, deforming the fluid. Either the strain is imposed and the torque is measured, or *visa-versa*. G'' and G' are calculated *via* the methods outlined in the text. Reproduced from [136]. b-c) Example G'' and G' as a function of frequency ω. Reproduced from [136].

fluids have a viscosity that increases with strain rate [136]. A generalized version of these equations exists that describes both a material's elasticity and viscosity as real and imaginary components respectively, when a material is subjected to sinusoidal deformation:

$$\tau = G^* \gamma, \tag{1.1}$$

where G^* is the complex (shear) modulus and σ and γ are the sinusoidal stress and strain respectively. When a sinusoidal stress, $\tau = \tau_0 sin(\omega t)$, is imposed the resulting strain lags as $\gamma = \gamma_0 sin(\omega t + \delta)$, where δ is the lag time. A material that is fully elastic has a lag of zero radians, whereas a fully viscous material has a lag of $\pi/2$ radians. A material with both elasticity and viscosity has a δ in between zero and $\pi/2$ radians. This can be described using the complex plain as:

$$\tau_0 e^{i\omega t} = G^*(\omega, \gamma_0) \gamma_0 e^{i\omega t - i\delta(\omega, \gamma_0)}, \tag{1.2}$$

where $G^* = G' + iG''$. Equation 1.2 simplifies to

$$G^*(\omega,\ \gamma_0) = \frac{\tau_0}{\gamma_0} e^{i\delta(\omega, \gamma_0)}. \tag{1.3}$$

The angle within this space describes the proportion of viscosity relative to elasticity as: $tan(\delta) = G''/G'$. Equation 1.3 allows for the full characterization of complex fluids and amorphous solids by measuring the changes in G'' and G' with frequency ω and the imposed stress amplitude τ_0.

Many “squishy” materials have been characterized using equation 1.3 [136, 122]. However, until recently, it was very difficult to image the microstructure of a material undergoing shear. Today, it remains challenging to image three-dimensional microstructure during relatively high shear rates. 3D scans are generated by rapidly acquiring many 2D slices, each separated by small distances, and composed into a stack. For high shear rates it simply is not possible to create a complete stack before the particles move appreciably between the beginning of the imaging process and the end. Because of this challenge, 2D colloidal suspensions at interfaces between fluids are phenomenal systems to study; only one image is required to characterize the microstructure of a 2D suspension.

Rheology of an interface

Interfacial colloidal systems are studied as a model for atomic systems [36]. Direct applications are also useful because the intricate chemistry of colloid-laden interfaces and clean interfaces arises in many applications such as cellular biology, food, and oil recovery [222]. A dedicated rheometer that measures the mechanical properties of interfaces was developed at the University of Pennsylvania [202]. Further refinement followed [222, 35, 182, 105, 70, 214] (Fig. 1.6). In these interfacial stress rheometers (ISR), a magnetic needle is placed at the interface between oil and water or air and water. Two boundary walls pin the interface at either side of the needle. The needle is driven axially by a known external magnetic field, created by a pair of Helmholtz coils. The displacement of the needle is measured *via* the microscope. With measured displacement and imposed force it is possible to calculate G^* for the interface. Instrument corrections are also required, based on the restoring force of the background magnetic field and the inertia of the needle. A descriptive force balance

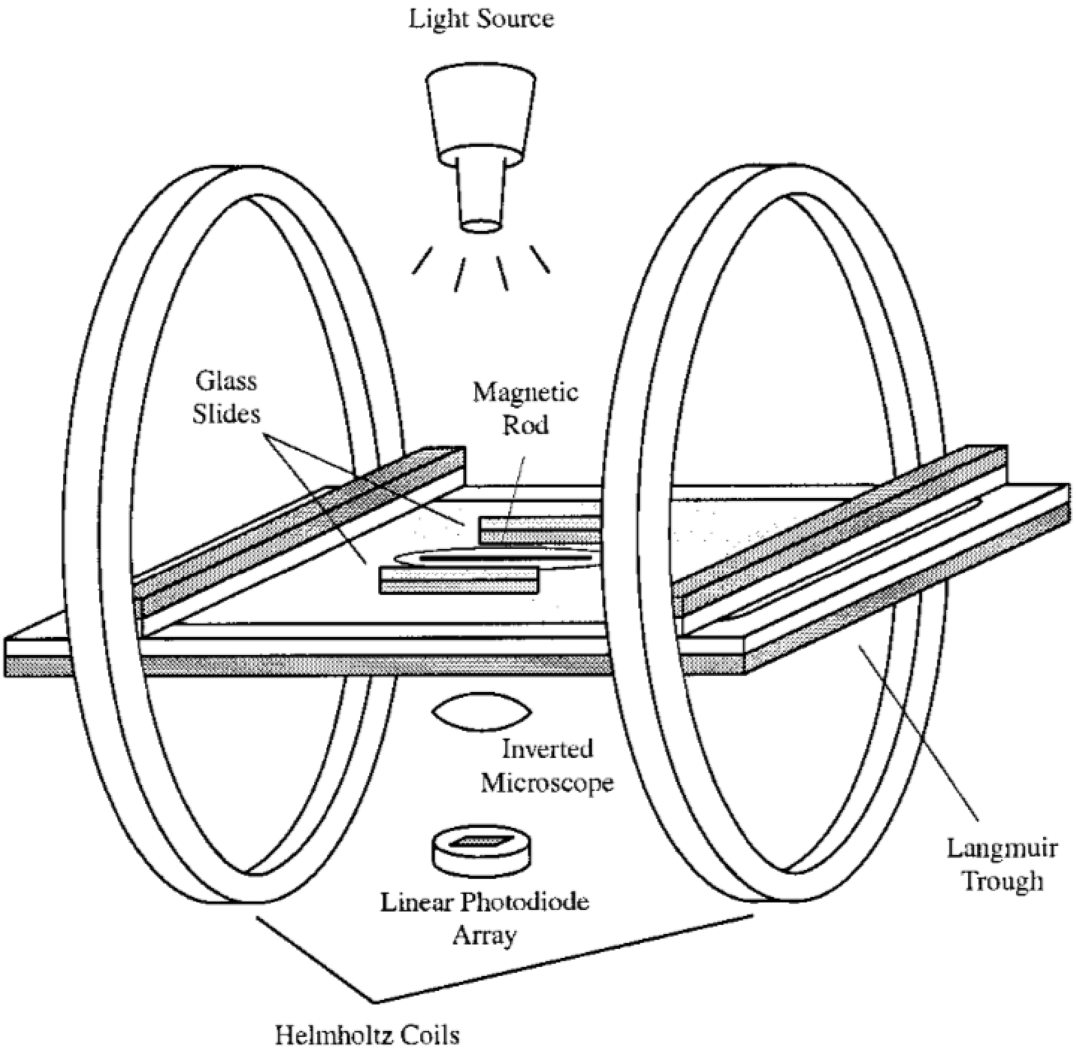
Light Source
Glass Slides
Magnetic Rod
Inverted Microscope
Langmuir Trough
Linear Photodiode Array
Helmholtz Coils

Figure 1.6: An example schematic of an interfacial stress rheometer. A magnetic rod sits between two walls at a water-air interface. The rod is pushed axially by an oscillating magnetic field generated by two Helmholtz Coils. The displacement of the needle is measured from below with a microscope. The rheological properties are calculated from the known imposed force, and the measured displacement using the methods described in the text. Reproduced from [35].

is used:

$$m\ddot{x} = AI - d^{*}\dot{x} - d\dot{x} - kx, \tag{1.4}$$

where m is the needle mass, x is the needle displacement, A is the conversion constant between the imposed force on the needle and the current through the Helmholtz coils,

I is the current through the coils, d^* is the drag on the needle from the interface, d is the drag on the needle from the bulk fluids above and below, and k is a spring constant like factor due to the magnetic field. In measuring the properties of the interface, it is crucial that the bulk fluid drag is negligible compared to the interface drag. The Boussinesq number, Bo, quantifies this ratio as, $Bo = |\mu^*|a/\mu$, where μ^* is the interface viscosity, a is the needle's radius, and μ is the viscosity of the bulk fluid. For accurate measurements, Bo needs to be above 100.

Equation 1.4 is an non-homogenious, second-order, differential equation that can be solved for the ratio of the displacement and imposed force amplitudes as well as the phase lag between them:

$$\frac{x_0}{F_0} = \frac{1}{\sqrt{(k - m\omega^2)^2 + (\omega d^*)^2}} \tag{1.5}$$

and

$$\delta_{interface}(\omega) = tan^{-1}\left(\frac{-\omega d^*}{k - m\omega^2}\right). \tag{1.6}$$

With the addition of colloids to the interface, the colloid's response can be gained by subtracting the interface's response at the same frequency from the observed response of the entire interfacial suspension as:

$$G^*(\omega) = \frac{w}{2L}\frac{F_0}{x_0}e^{-i\delta}\Bigg)_{colloid} = \frac{w}{2L}\frac{F_0}{x_0}e^{-i\delta}\Bigg)_{measured} - \frac{w}{2L}\frac{F_0}{x_0}e^{-i\delta}\Bigg)_{interface}, \tag{1.7}$$

where w is the distance between the needle and the wall and L is the length of the needle. Using equation 1.7 it is possible to describe the response of a colloidal monolayer.

The custom Interfacial Stress Rheometer

In recent years Keim and Arratia [105, 106, 107] developed an interfacial stress rheometer that can simultaneously measure the rheology as discussed above while imaging the precise positions of $\sim 50,000$ particles spanning the entire space between the needle and the wall. Trajectories are generated with extremely high spatial ($\pm 0.5\mu m$) and time accuracy ($40 frm/sec$). The experiments conducted by Nathan Keim and the system developed by Keim and Arratia were used throughout this thesis so a short overview of the colloidal suspension studied is provided here.

The bi-disperse interfacial monolayer studied in this thesis is composed of an equal parts by number mixture of 4.1 and 5.6 μm-diameter sulfate coated latex (polystyrene) particles (Invitrogen; nominal diameters 4 and 6 μm) adsorbed at the interface between deionized water and decane [11, 161, 142]. The mono-disperse interfacial material is composed of 5.6 μm-diameter sulfate latex particles. Area fraction is set by the number of particles dispersed into the experimental cell (a 6 cm-diameter glass dish); positive osmotic surface pressure keeps the area fraction uniform. The number densities of the systems are approximately 16,500 particles/mm^2 (bi-disperse) and 14,300 particles/mm^2 (mono-disperse). Average center-to-center distances between particles are $7.4\mu m$ (bi-disperse) and $7.7\mu m$ (mono-disperse).

When placed at an oil-water interface hydrophobic particles experience Pieranski [172] dipole–dipole repulsion through the phase of lower dielectric constant [172, 23, 95, 71, 210, 123, 11, 157, 10, 142, 161, 163]. This dipole-dipole interaction is caused by individual particles inducing asymmetric counter-ion distributions in either phase. We note that the particles studied here are small enough that they do not cause gravity-driven capillary deformation over long enough ranges to interact with each other over the distances in our experiments [117, 157]. Additionally, mesostructures, a sign of inter-particle attraction, have not been observed in our experiments.

Previous studies have examined the specific strength of the dipole-dipole interaction in a system very similar to ours; i.e., using the same preparation protocol and a system composed of sulfate coated latex particles (Invitrogen) at decane-oil interfaces [162]. The dipole-dipole form is:

$$\frac{U(r)}{k_B T} = a_2 \frac{1}{r^3} \tag{1.8}$$

where U is the potential, k_B is Boltzmann's constant, T is the thermal temperature,

a_2 is the scaling constant, and r is the center-to-center distance between particles. By separate methods using optical tweezers and Monte Carlo simulations, Ref. 162 reported $\langle a_2 \rangle = 5.1 \pm 2.4 \times 10^{-13} m^3$ (mean around a gamma distribution). Ref. 142 reported a three-phase contact angle of $\phi = 90 \pm 20°$. Additionally, pendant drop experiments [183, 209] have previously determined that the surface tension of the decane-water interface is $\gamma_{OW} \sim 50 mN/m$.

The interfacial stress rheometer and other experimental systems [36] allow for the observation of the microstructure during deformation of amorphous colloidal systems. There is also a host of molecular dynamics simulations aimed at examining the microstructure throughout deformation. Several approaches have surfaced from simulations and experiments that explore signatures of yield within the microstructure. The next two sections introduce excess entropy, which characterizes the state of an entire material's microstructure, and shear transformation zone theory, which quantifies local plasticity.

1.2.2 Models and insights linking microstructure to bulk behavior

Meta-stability of amorphous solids

Stability is a topic at the heart of material science. Are chemical reactions constant? Is a system in mechanical equilibrium? Does a process transfer heat? Each of these questions inform how the material world progresses over time and whether or not it does so reversibly [178, 177, 39, 37, 146, 40, 116]. According to the second law of thermodynamics, the most stable state (chemically, mechanically, and thermally) is the one that has the most possible constituent configurations; in other words, the stable state is the one in which nothing changes because it is by far the most probable [146, 37]. A stable state is also the one that has the lowest and most evenly dispersed energy [37].

For solids, the fundamental questions are how mechanically stable the constituents

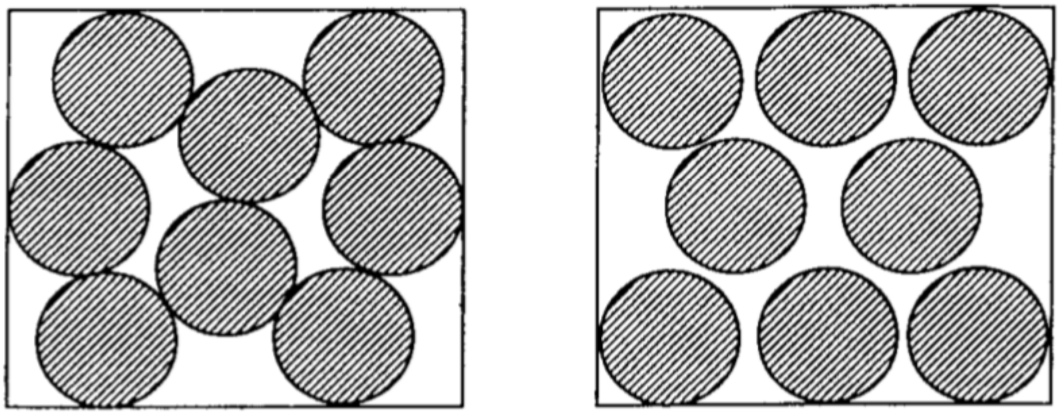

Figure 1.7: An example of the greater free volume available to crystalline grains versus an amorphous packing. An illustration of how crystals have a higher entropy and a higher maximum density. Reproduced from [122].

are and how stability relates to the number of configurations available [122]? Consider figure 1.7. On the right is a crystal in a box. An amorphous configuration is in the box on the left. Both boxes have the same area and yet the crystalline particles have room to diffuse *via* Brownian motion whereas the amorphous particles are constrained by contacts. Because the crystalline particles can move without making contact, the crystal has the maximum number of available configurations. This observation has two consequences: crystals represent the equilibrium state [122, 98] and available volume relates to the entropy in systems where particles only interact by making contact [63]. Interestingly, this implies that, given enough time, thermally driven amorphous systems (left) will evolve towards a crystalline state (right). With the addition of particle interactions other than contact, such as those caused by charged particle surfaces, particles are further constrained by their neighbors. The crystal remains the equilibrium state, but the available configurations are lower than the case without forces [122]. In systems with inter-particle interactions, forces are a measure of entropy instead of volume [218, 219, 20, 21].

In the amorphous state, each particle is constrained by its neighbors (figure 1.7b) [220, 126, 18]. The constraints impede the ability of the system to transform into a

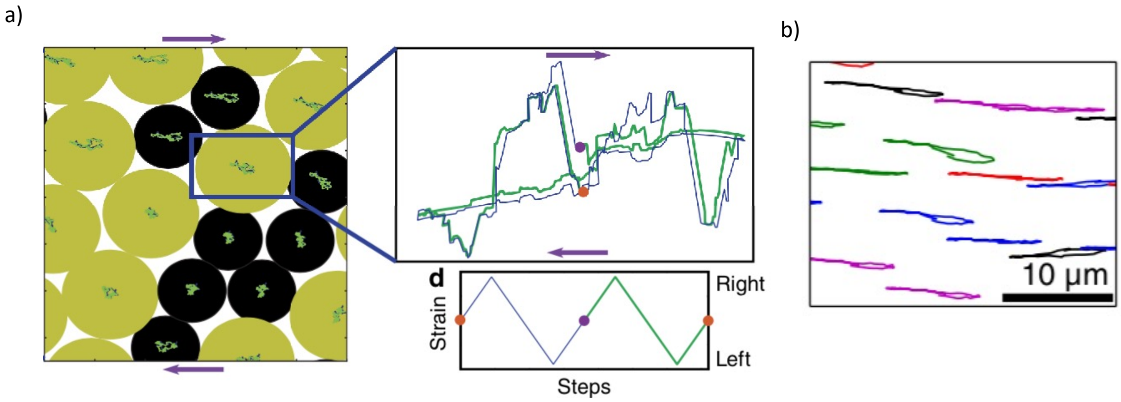

Figure 1.8: a-c) Examples of the chaotic motions that non-Brownian particles within an amorphous packing exhibit when undergoing shear deformation. a) Simulations of a-thermal cyclically sheared amorphous packings. Reproduced from [180] b) Experiments of non-Brownian colloidal particles at an interface undergoing cyclic shear. Reproduced from [106].

crystal. The constraint phenomenon is known as caging [122, 220] and the overall system is called jammed [126]. Because caging is so strong relative to thermal energy, many jammed systems, such as glass, require an astronomical length of time to crystallize. Never-the-less, this crystallization is a candidate for the slow yielding or creeping described above; crystallization corresponds to greater available volume [122], which allows the material to slowly deform because there are weaker supporting particle contacts. On earth, the deformation that comes with slow yield is biased in the direction of our gravitational field, leading to the creeping of hill slopes [56, 68]. Such systems that evolve so slowly are described as being stuck in meta-stable states; not truly stable, but effectively so.

A statistical approach: the analogy between thermal and a-thermal amorphous solids

In any system composed of particles larger than about $1\mu m$, the contribution of thermal motions is negligible for all practical purposes. For instance, the arrangement of candies within a jar is likely amorphous. It is extremely likely the candy will be eaten or melt before they can rearrange into a crystal. On the other hand, a jar

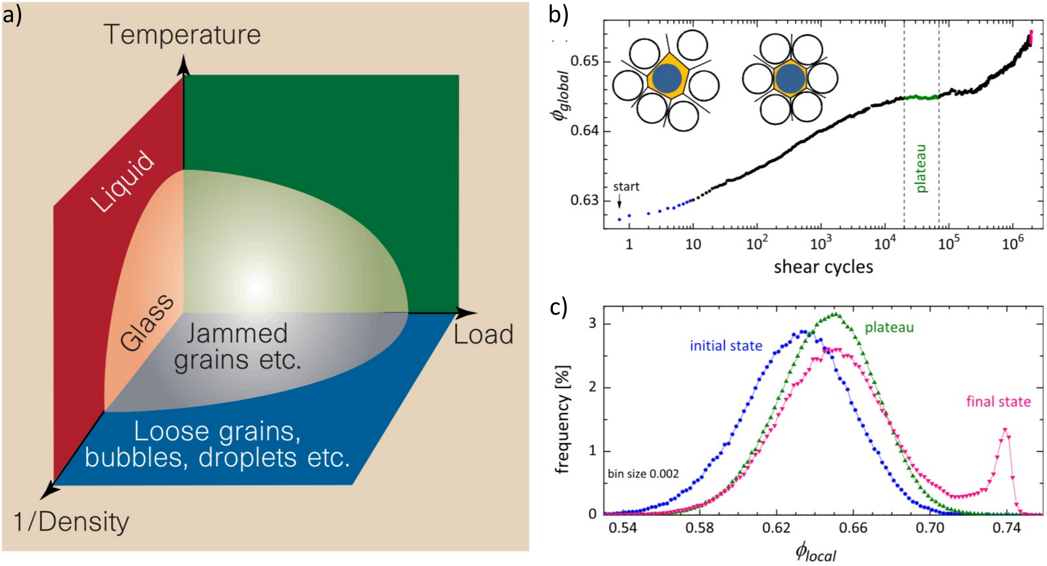

Figure 1.9: a) The load-density-jamming phase-state diagram for amorphous materials. Along the temperature-density plane, glass exists at high density and low temperature. Once temperature is raised or density falls a glass will melt. Crystallization of glasses will occur at various rates. Along the load-density plane a similar phenomenon is observed: a packing will become un-jammed with increasing load or decreasing density. Reproduced from [126]. b) Over many tens of thousands of cyclic shear cycles the density of an amorphous solid composed of non-Brownian hard spheres will plateau to the value of random close packing. However, after hundreds of thousands of further cycles, the density will begin to increase again. c) As the density increases past the random close pack, crystals are observed forming homogeneously within the amorphous solid. Reproduced from [186]

of honey can crystallize before someone gets around to eating it. Thermal motion does not cause the candy to vibrate, so it does not crystallize. The honey molecules do vibrate so crystallization occurs. In sheared, a-thermal systems, particles exhibit erratic motions similar to the vibration that occurs in thermal systems [152, 193, 181, 180, 132, 207, 106, 196]; as load is applied, particles jostle each other, creating chaotic motions (Fig. 1.8). These chaotic motions occur because particles in an amorphous material cannot perfectly follow continuum deformation fields without bumping into their neighbors; conversely crystals can follow continuum deformations. Above a certain load threshold 'melting' begins because particles can shift positions, just as above a temperature threshold a solid turns to liquid (Fig. 1.9a). In recent, painstaking experiments, it has been shown that below the load threshold, an a-thermal amorphous solid will slowly crystallize from homogeneous nucleation sites over hundreds of thousands of shear cycles [186] (Fig. 1.9b&c) during cyclic shear. Amazingly, mechanically driving a jammed system appears analogous to thermally exciting a glass; both speed up the transition from meta-stable states to equilibrium states.

The similarities between the behavior of thermal and sheared systems reveals that a common framework may govern both [126]. Typically, the macroscopic behavior of thermal systems at equilibrium are described by thermodynamics, which relies on energy conservation as its backbone [39, 116]. Equilibrium thermodynamics can be derived using statistical mechanics [146]. As the name implies, statistical mechanics is based not on the deterministic and time reversible laws that govern individual particles, but instead on the distributions of properties of many (at least trillions) of particles [146, 178, 121]. This trick enables statistical mechanics to explain time irreversible macroscopic phenomena, so long as they happen very slowly (quasi-statically) and transition between two equilibrium states [178, 116]. The chaotic, n-body nature[13, 211] of the microscopic world contributes to the time evolution of the macroscopic world [178]. Though the similarities can be striking, it is not immediately clear how to redevelop statistical mechanics for meta-stable amorphous solids; especially those that are a-thermal, which signals an apparent lack of energy [20, 21]. There is, however, the advantage that amorphous systems evolve quasi-statically. Coincidentally, crystals can be described by deterministic, continuum equations precisely because their particle motions are very well correlated; they do not display chaotic motions during deformation, so entire grains represent a predictable 1-body system.

There have been attempts at modelling macroscopic properties of a-thermal amorphous materials based on deterministic approaches [185, 167, 51, 194, 50, 195, 213, 15]; in other words, looking at specific local particle configurations and trying to make predictions about whether a plastic event will occur or not. These methods have very strong success over small time windows [15, 51]; they identify if an event is occurring and the types of kinetics that bring about plasticity. These local structural signatures can be very helpful in identifying which sorts of systems are developing plastic events [185]. But these models could be improved by incorporating statistics so that they can capture time evolution [178].

The first step toward a statistical description is shear transformation zone theory (STZ theory) introduced by Falk and Langer [67] and later developed and expanded [67, 29, 30, 31, 32, 207, 132, 167]. STZ theory tries to link the *probability* of a local plastic event occurring to the volume available to the nearby particles [67]. The key contribution was the introduction of a variable, $D^2_{min.}$, that classifies how well a particle neighborhood manages to follow the prescribed deformation; in other words, $D^2_{min.}$ measures affinity of local deformations [66]. It is calculated as the sum of the differences between best fit affine deformations and the measured non-affine deformations:

$$D^2_{min.} = \frac{1}{N}\sum_i^N(\mathbf{r}'_i - \mathbf{A}\mathbf{r}_i - \mathbf{b})^2, \tag{1.9}$$

where N is the number of particles in the local neighborhood, $\mathbf{r}'$ is the final position vector of particle i, $\mathbf{r}$ is the initial position vector of particle i, $\mathbf{A}$ is the best fit affine transformation tensor between the initial and final positions of all of the particles, and $\mathbf{b}$ is the best fit translation vector of all of the particles. If a particle neighborhood has a high value of $D^2_{min.}$ it is exhibiting chaotic motions and cannot be described by deterministic approaches alone. If $D^2_{min.}$ is low, the neighborhood is deforming in a smooth, deterministic way [66]. Keim and Arratia [105, 106, 107] found that non-affine particle motions appear precisely as the material yields rheologically. Non-affinity appears to correspond with the amount of plastic dissipation [106]. Even though STZ theory is built on the probability of local plasticity occurring, as measured by $D^2_{min.}$, it can be unwieldy, incorporating many variables [29, 30, 31, 32, 207, 132] that are not readily measurable or definable [32] in experiments or even simulations. Finding ways to measure these or similar quantities and perhaps simplifying the modelling could make STZ theory much more versatile.

Another more recent step towards a probabilistic description of a-thermal amorphous solids borrows from glassy physics. In thermal systems, the mobility of particles is linked to the entropy of a system in excess of its equivalent ideal gas. Excess entropy is useful because it only requires knowledge of particle configurations. Excess entropy is a thermodynamically derived quantity that does not consider vibrations caused by thermal motions [179, 148, 187, 223, 16]. In thermal materials, it has been shown in simulations and experiments that excess entropy scales with particle mobility [62, 188, 133, 61, 133]. Because of excess entropy's a-thermal nature and its known link to thermodynamics, the research groups of both Bonnecaze and Tanaka have recently used excess entropy to describe simulations of a-thermal, amorphous solids. It was shown by Ingebrigtsen and Tanaka [96] that particle mobility is also linked to excess entropy in a-thermal systems. Bonnecaze et al. [27, 113] showed that there is a link between excess entropy and mechanics. Given these links, a natural question is whether excess entropy can be incorporated into STZ theory to describe amorphous solids.

Excess entropy incorporates many of the concepts discussed above (probability, caging, energy distribution, inter-particle forces, crystallinity, available volume) *via* its functional definition [16]:

$$s_2 = -\pi\rho \int_0^\infty \big\{g(r)ln[g(r)] - [g(r) - 1]\big\} r dr, \tag{1.10}$$

where ρ, is the density of particles throughout the entire system and g is the radial density of particles as a function of distance from a reference particle, r. Representative examples of $g(r)$, the probability of particles being separated by a certain distance, r, are given for crystals and amorphous solids in figure 1.10. As peaks become narrower, excess entropy increases; there are more ways to arrange all of the particles to make narrower peaks, than wide ones. Often above 90% of excess entropy's final value comes from r between zero and the distance to the trough in $g(r)$ between the first neighbors and second neighbors. Because of this, excess entropy can be considered to characterize the caging from first nearest neighbors. $g(r)$ also reflects another definition of entropy: the spatial dispersion of energy. A low

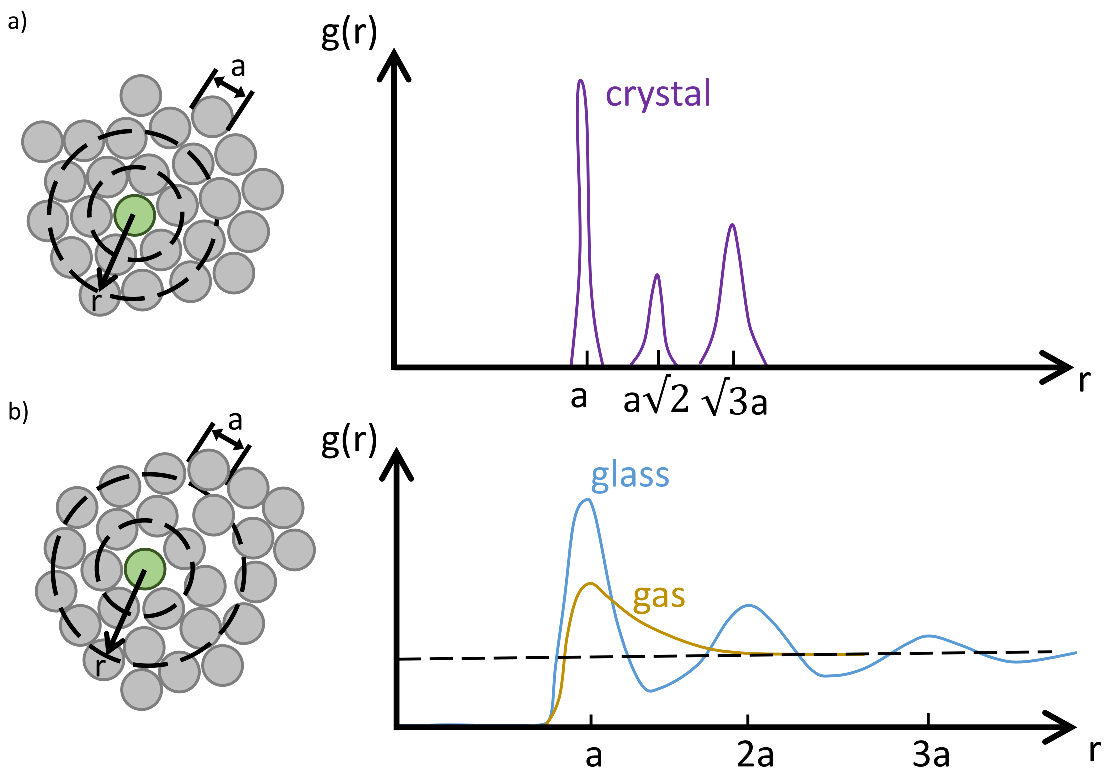

Figure 1.10: Example packings and their corresponding radial distribution functions. a) Within the radial distribution function, a crystal has narrow peaks at positions determined by the pattern. b) An amorphous material has much more position variation around first neighbors and second neighbors. Gasses have very high variance in positions and display no layering of particles. Adapted from [40].

entropy implies the energy is not well distributed throughout a system. Conversely a high entropy implies an even distribution. Wider peaks correspond to some cages having stored drastically different amounts of energy in their neighbor interactions (i.e., low excess entropy, reflecting a system similar to an ideal gas). By comparison, crystals have only a few characteristic distances between particles, so all cages have very similar energy (i.e., a high excess entropy, indicating a system that is different to an ideal gas). Similarly, excess entropy captures volume and force distributions. For all of these reasons, excess entropy appears to perform the same function as thermal entropy, but is applicable to a-thermal solids, from perfect crystals to completely amorphous.

1.3 Thesis Overview

The objective of the proposed thesis is to show how the microscale within a-thermal amorphous solids gives rise to macroscale mechanical properties. Along these lines, I have three interrelated goals that apply to disordered systems undergoing yield. These are:

1) Connect bulk mechanical yield to particle scale kinematics.

2) Reveal the global interplay between particle kinematics and configurations.

3) Use statistical changes in particle configurations to predict and characterize bulk yield.

In pursuit of these goals, I have investigated numerous physically motivated metrics that probe the behavior of individual particles, groups of particles, and all of the particles within the system. I analyze several model, 2D, disordered systems that range from large crystalline grains to almost no discernible crystalline grains. To a large degree my work has contributed to the understanding of the three goals listed above. Each chapter addresses one of the above goals, which build conceptually off each other. Moreover, each chapter is published [76, 77, 75].

In Chapter 2, I investigate dynamical signatures of constituent particles in semi-amorphous 2D colloidal packings of a-thermal particles. I find that at low oscillatory strain amplitudes the trajectories are erratic. With increasing strain amplitudes, particles trace out areas though out a cycle; they move in the shear direction and then return along a different path. These limit cycles indicate energy dissipation. I show that for particles that return to their original positions at the end of a shear cycle, the area enclosed is a key metric that reflects the total energy dissipated. Moreover, the arc-length of each trajectory is limited to the length predicted by the strain field – even during chaotic motions. A dimensionless equation is uncovered that relates the strain amplitude with the average enclosed area divided by the average normalized arc-length. These enclosed areas represent signatures of plastic energy dissipation during yield. This chapter reveals that the statistics of chaotic the dynamics relates to the mechanical response.

Chapter 3 explores experimentally the relationship between particle mobility and excess entropy. I determine that above yield, the escape time of particles leaving their cages scales systematically with the value of excess entropy at later times in the shear cycle. This result indicates two conclusions. First, causality is established. Imposed stress leads to a resulting strain as we already know from rheology. The imposed strain results in a spike in particles shifting past their neighbors. These shifting motions, precipitate specific structures within the microstructure as characterized by excess entropy. Second, the average amount of mobility of the particles at any given time directly relates to the resulting structures. This implies that it may be difficult to use *a-priori* particle positions to predict long-time particle dynamics because it appears to be the case.

Chapter 4 provides a phenomenological model of a link between a material's relative elasticity and plasticity for a given oscillatory deformation. I derive from first principles an energy balance that applies to non-Brownian, amorphous suspensions. This derivation uses a grand canonical ensemble over each cage in a system to describe yield as a transition between pressure and chemical work. With the energy balance in hand, it is possible to recover the amount of elasticity relative to plasticity for any given strain amplitude by using observations of the microstructure. Each variable in this model is measured and the relationships hold experimentally. A statistical link between bulk yield and the microstructure is reported.

Chapter 5 includes a summary of this dissertation and provides outlook for future works and perspective on the results.

Chapter 2

A statistical connection between the dynamics of individual particles and the onset of yield

2.1 Introduction

Much of our natural and built environment is made of amorphous materials, such as foods, foams, and glasses [122, 42]. The properties of disorder may be exploited to create materials with desirable properties, e.g. yield stress or shear thinning fluids. When amorphous solids fail, however, catastrophic fluidization may occur: witness the collapse of solid soil into fast-flowing mudslides [101, 5]. Therefore, predicting and controlling failure within these materials is of fundamental importance. Bulk rheology of amorphous solids is an emergent property arising from micro-scale grain-grain and fluid-grain interactions [82, 220]. There has been major progress in unifying the rheology and yielding of ideal granular materials and suspensions [33, 85]. Yet such descriptions are mostly phenomenological; moreover, small variations in particle size, shape, surface properties, or inter-particle forces may cause dramatic changes in bulk properties. Often, constituent particles may be jammed together, preventing all undriven motion either by confinement or by outside forces such as gravity. These factors complicate the unifying description of such materials by creating structure based effects, which commonly cause history dependent responses [220, 122, 101].

A key insight has been that as energy is injected via shear into a disordered material, bulk deformations are achieved via contributions from local rearrangements [66, 139]. These rearrangements within the microstructure are thought of as particles shifting to lower energy configurations, thereby dissipating some of the injected energy [67]. The energy not dissipated is recovered as elastic energy. The yield transition is quantified as a shift from mainly elastic to dissipative response with increasing strain [122]. For a wide range of disordered materials, a universal strain of ~ 3% has been found to mark the yield transition [50].

A convenient way of repeatedly probing a system's elasticity (storage modulus) and dissipation (loss modulus) is to subject the material to oscillatory stress. This method gives statistically robust measurements over as many cycles as desired. Under oscillatory stress, three types of particle dynamics have been observed. First are those that return to their initial position by the same path they went in (elastic and reversible). Second are those that return via a secondary path (plastic but reversible). Third are particles that do not return at all (plastic and irreversible) [173, 132, 207, 181, 176]. It is thought that reversible particles enter a new minima in the energy landscape, but are returned once strain reverses; i.e. the energy landscape is restored. However, irreversible particles do not return, because of permanent modification to the energy landscape by small perturbations in the positions of neighbors [152, 180]. It has been observed that reversible, plastic trajectories emerge at the same strain amplitude as the bulk material's rheological yield [105, 106]. Therefore, understanding reversible, plastic trajectories may shed new light on the yield transition in amorphous materials.

Strikingly, reversible, plastic trajectories are similar to a classic limit cycle description of dissipation from non-linear analysis [106, 211]. Past research has explored this idea, showing via simulations that the area traced is related to energy dissipated [196, 181]. An intuitive implication is that reversibly plastic trajectories within the same system may share similar properties, reflecting changes to an energy landscape by stress. It may be possible that reversibly plastic particle trajectories are stable from one cycle to the next, corresponding to specific meta-stable states within the energy landscape [104, 181, 180, 169]. More broadly, particle dynamics (reversible vs irreversible, elastic vs plastic) near and above yielding are still not well understood.

In particular, there are still many outstanding questions regarding how particles transition from the elastic to plastic regime. These include: Are irreversible particle trajectories born out of reversible plastic trajectories (limit cycles)? Or are reversibly plastic particles stable as a function of strain, space, or time? And is there a relationship between the properties of these reversible plastic trajectories and the material's macroscopic rheology? Answering these questions will help elucidate microscopic factors that bring about bulk material yield and inform models.

In this manuscript, we experimentally investigate the Lagrangian dynamics of particle trajectories in a two-dimensional dense colloidal suspension that is undergoing cyclic shear. Samples are deformed using a custom built interfacial stress rheometer that permits characterization of the sample microstructure while simultaneously measuring its bulk flow respnse (i.e. rheology). Contrary to intuition, we find that there is no chaotic progression in time (in other words, they do not evolve from elastic to reversibly plastic to irreversibly plastic). Instead, particles develop specific trajectories based on their position within the shear channel, and the strain amplitude. For example, above yield, particles in the center of the channel are much more likely to have irreversible trajectories. Also, both plastically and elastically reversible particle trajectories transition to irreversible trajectories in later cycles (and vice versa); they sometimes change states. However, plastically and elastically reversible trajectories do not transition between each other. These observations are used to deduce the presence of a melting front, whose depth increases with strain amplitude. Based on a quantification of this depth we present an empirically determined strain amplitude scaling that quantifies plastic dissipation.

2.2 Methods

We study the yield transition using an interfacial stress rheometer as shown in Fig. 2.1a. In short, a steel rod (230μm in diameter, 28.1mm in length), referred to as a needle, is placed at a water/decane interface. The interface is pinned on either side of the needle by glass walls (18mm long, 3.175mm spacing), ensuring the interface is planar. A monolayer of particles is also adsorbed at the interface (Fig. 2.1b). To shear the monolayer, the needle is driven sinusoidally by a uniform magnetic field, which is imposed by a pair of Helmholtz coils [202].

Rheological information is calculated by measuring the displacement of the needle using an inverted microscope and comparing to the imposed force. The effect of the interface on the needle is characterized by fitting fluid imparted drag and magnetic field imparted spring forces to the solution of a forced spring-mass-damper second order differential equation across measured needle displacement and proscribed force on the needle. The interface's effect is subtracted directly from the total observed response of a monolayer and interface, giving the storage and loss moduli, notated G' and G'' respectively [35, 182].

To ensure rheological measurements are accurate, drag from the bulk fluid must be negligible compared to the drag from the interface. This ratio is calculated directly by the Boussinesq number, $Bq = |\eta^*|d/\eta_L$. η^* is the observed complex viscosity, d is the needle diameter, and η_L is the liquid viscosity of the oil and the water, which is $\sim 10^3$ Pa s. Here the Boussinesq number is $\sim 10^2$ [35, 182], so that in plane stresses are dominant.

Three systems of mono-layers, composed of non-Brownian particles are presented here. Table. 2.1 provides a summary of their differences. All three systems have crystaline grains with large amorphous swaths at the boundaries. However, the degree of crystalinity differs greatly between the three. For more information on disorder in these systems see [105, 106, 107]. All are composed of mixtures of non-Brownian, sulfate latex spheres of nominal diameters 4.1μm and 5.6μm (Invitrogen). Sulfate charge groups coat the surface, creating an overall dipole-dipole repulsion force be-

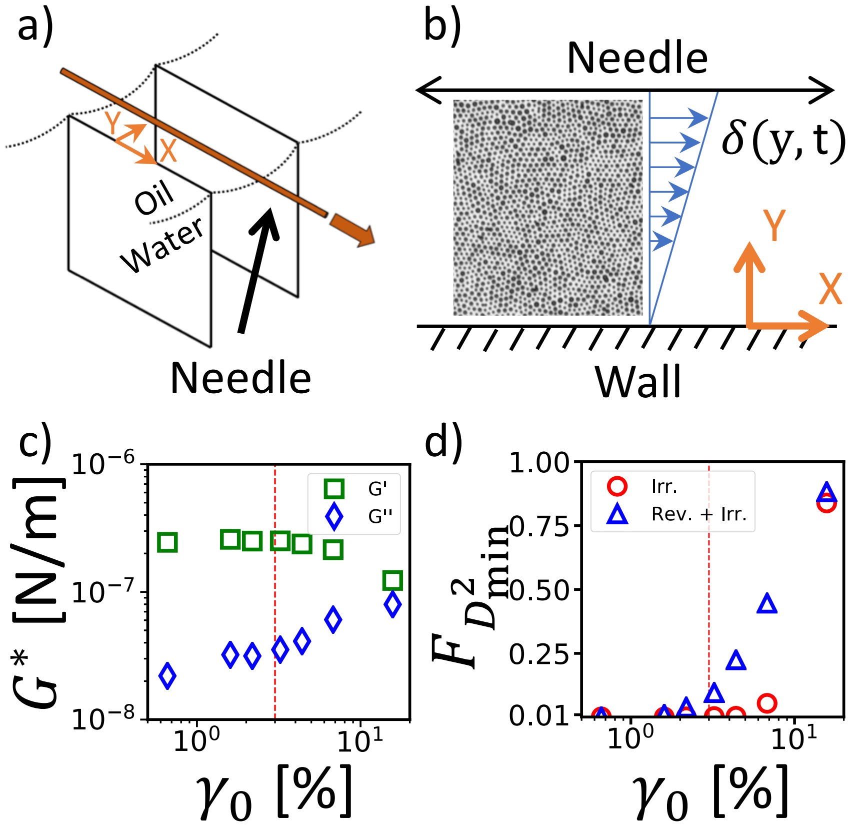

Figure 2.1: Schematic of the system and background of data. a) Diagram of the interfacial stress rheometer including oil/water contact line pinned at the two glass walls and the axially displacing needle. b) A top view schematic with a description of coordinates and the idealized displacement field, $\delta(y,t)$. Also shown is an image of the particle micro-structure representing about 1/24th of a total image. The vertical edge is $250\mu m$ long. Crystallized grain clusters may be observed, surrounded by expansive amorphous boundaries. c) Storage, G', and loss modulus, G", as a function of strain amplitude γ_0, both showing inflection at the classic yield point of ~3% (**- - -**). d) Characterization of the fraction of particles displaying irreversible and reversible non-affine events. The total number of reversible and irreversible events diverge at the yield point.

tween particles [163]. These inter-particle forces are strong enough to create a stable material at the relatively low area fractions studied here, ~ 31 – 43%. We refer to the monolayer as "jammed" in the sense that without shear, the individual particles do not undergo measurable changes in position — let alone rearrangements. In addition to being jammed, this material is also soft, meaning that it can be deformed readily. An example image of monolayer A is shown in (Fig. 2.1b). Packings typically have

Table 2.1: A summary of the properties of the systems presented here, including dispersity, particle size ratios, sizes of particles, area fractions, Φ.

Dispersity	Ratio	Diameters	Φ
Bi-disperse	50-50%	4.1, 5.6μm	~ 31%
Mono-disperse	N/A	5.6μm	~ 35%
Bi-disperse	60-40%	4.1, 5.6μm	~ 43%

small grains of a few particles with amorphous boundaries. Images span the space between a wall and the needle (~ 1000μm) and include ~40,000 particles. During each experiment imaging is carried out at 100-600 frames per cycle for up to 30 cycles. Features are identified and linked together using Trackpy [3]. The resultant trajectories are analyzed in several ways discussed below. The analysis presented in this paper is of the Bi-disperse monolayer with 50-50% distribution, to serve as a demonstration. Final results, however, are shown for all three systems. Information about analysis of the other monoayers are available upon request.

Here, frequency is held constant at $0.1Hz$ during all experiments with monolayer A. Strain amplitude, γ_0, is defined as needle displacement amplitude, δ_0, divided by the distance between the wall and the needle. γ_0 is varied between 0.7% and 17%. This range fully traverses the yield transition, which is known generally to be near 3% strain amplitude for many amorphous or glassy materials [50]. Yielding is often designated based on an inversion of G' and G''. As seen in Fig. 2.1c the inversion occurs near 3% strain amplitude, consistent with previous findings. Further information about this system can be found in [106].

As a touchstone to previous work reported in the literature $D_{2,min}$ calculations are presented. $D_{2,min}$ can be thought of as a quantification of a local deformation's non-linearity; i.e., it is the mean squared deviation of particle positions from a best-fit affine transformation over a time interval. We normalize this value by the square of the typical particle separation, a, and the number of neighbors considered (those within the two nearest neighbor shells, $2.5a$). A non-affine event is characterized as a particle having a $D_{2,min}$ above 0.015, a value used in simulations of amorphous solids. This threshold has been found previously to correspond to a disturbance in particle

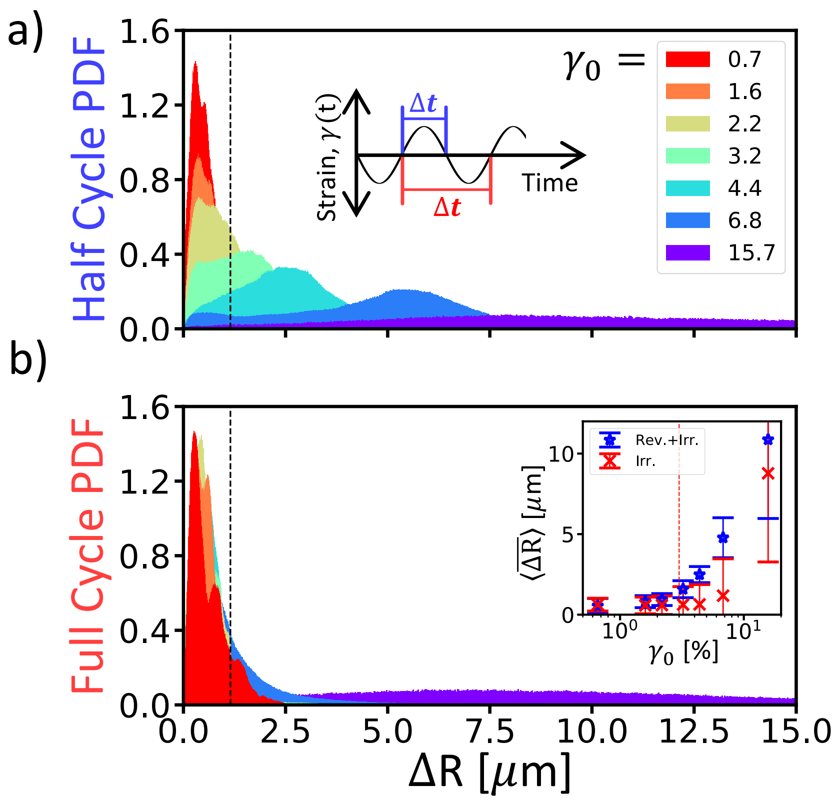

Figure 2.2: Probability density function comparisons of particle displacement after a) half cycles and b) whole cycles over a range of strain amplitude. a) Particles fall within a small displacement below yield, slowly transition to a bi-modal distribution near yield, and finally nearly all particles escape above yield. A threshold (- - -) is included, found previously in simulation studies, $0.1a$ = $1.15\mu m$. Inset: visual representation of when half cycles and whole cycles are taken relative to strain, γ_0. b) A separate transition is present, well above yield. Inset- the average displacement of particles that are to the right relative to strain amplitude over half and whole cycles.

location of about $0.1a$ [66].

In this paper, we measure $D_{2,min}$ over two time intervals: half cycles and whole cycles as shown in the inset of Fig. 2.2a. Whole cycle events are termed 'irreversibly plastic' because they indicate particles that have not returned to the positions they held at the beginning of the cycle. Half cycle events are also thought to detect irreversible plasticity, however they also detect a second type of event: 'reversible plasticity'. These events are characterized by particles that do not return to their original position after a half cycle, but do in fact return after an entire cycle. These particles typically trace limit-cycle trajectories as mentioned above. For further information on reversible and irreversible plasticity in this system and similar systems please see [105, 106]. Here we report the number of $D_{2,min}$ events averaged across steady-state cycles as a fraction of all particles observed, $F_{D_{2,min}}$ (Fig. 2.1d).

To build a physical understanding of the types of non-affine events (reversible or irreversible) that are occurring, we measure several characteristics of each trajectory. One characteristic is the displacement of a particle over a half cycle and a whole cycle (see the inset of Fig. 2.2a for the time intervals used). From this information it is possible to determine weather any given particle has returned to its original position or not, using a threshold of $0.1a$ as found in previous $D_{2,min}$ analysis [66]. To be explicit, any particle that returns to within a tenth of the inter-particle spacing, a, has returned and a particle that does not return to within $0.1a$ has escaped.

In addition, we calculate the area enclosed by trajectories of the particles that did not escape (the area of those that have escaped is defined as zero). This calculation is not as straight forward as it may initially seem; trajectories often intersect tens of times in a single half cycle. However, standard area calculation algorithms detect self intersections as a negative area and will not produce absolute area. Therefore, we have implemented a highly optimized algorithm that detects intersections and redefines sub-polygons that together make up the original area. Each sub-polygon's area is then calculated and summed. In addition to area, we calculate total arc-length.

Clusters are present within the enclosed area and arc-length phase space. To determine the relative numbers of particles transitioning from any given cluster to another, an algorithm must first be used to identify boundaries between clusters. The algorithm used in this paper is known as HDBSCAN (Hierarchical Density-Based Spatial Clustering of Applications with Noise) [38, 144]. This clustering routine is strong at detecting clusters based on variations of density as well as distance within the chosen phase-space, and it is easily implemented in Python.

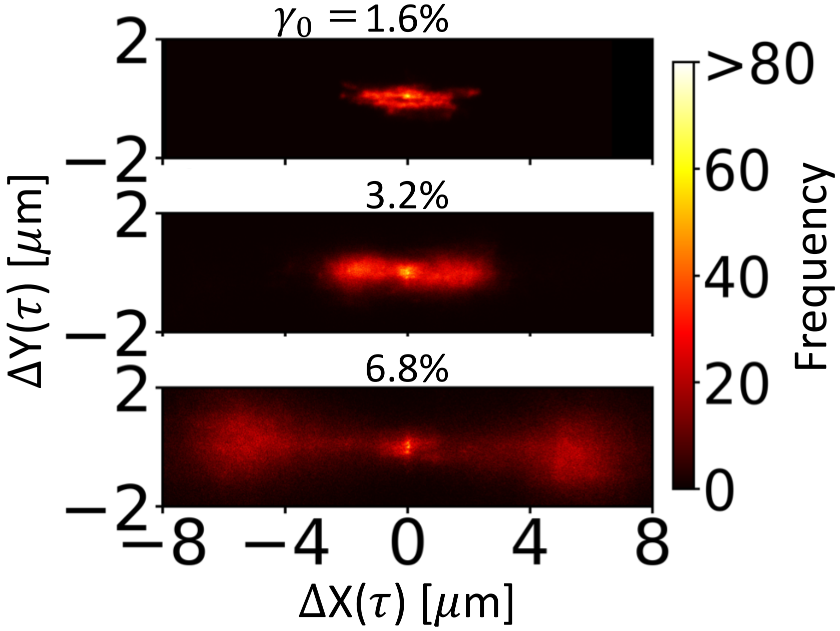

Figure 2.3: Characterization of half cycle displacement vectors by x-y displacement Poincarè sections for three strain amplitudes. An additional attractor develops with increasing strain amplitude. Strain is increased from below yield (top), to near yield (middle), to above yield (bottom). Below yield, most particles return to their original position as expected from Fig. 2.2. Above yield, many particles do not return; their paths back to the origin are cut short, ending at periodic, chaotic points centered on the x-axis. These points grow outward with strain amplitudes above yield (~3%). This can be seen in detail for all strain amplitudes in a video within the Supplemental Information.

2.3 Results

We are interested in comparing the Lagrangian dynamics of each individual particle within the system; how these variables may change with position in the shearing channel, between successive cycles, and with strain amplitude. To gain this insight, we first investigate whether strain amplitude may be interpreted as a bifurcation variable affecting the propensity of particles to escape from their nearest neighbors. Fig. 2.1d, shows that the number of total non-affine events bifurcate at the yield point. To investigate further, Fig. 2.2a gives a normalized histogram of the displacement distance over half a cycle. Crucially, particles from the near yield case (3.2%) show a bi-modal distributions about the noted threshold. Particles to the left have returned

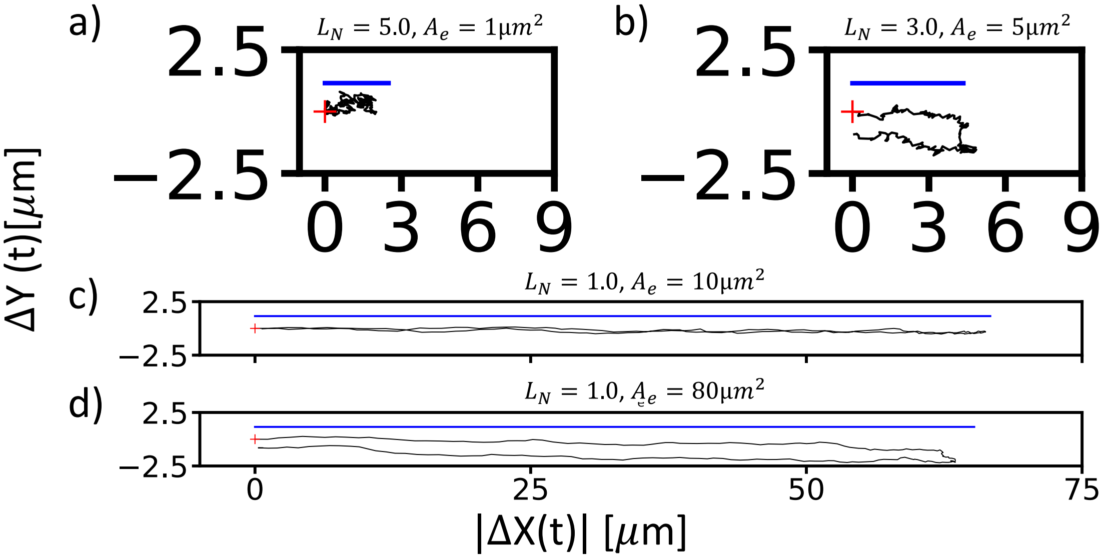

Figure 2.4: Above yield trajectories (γ_0 =6.8%). Trajectories are black with a red plus, (+), at the beginning of the cycle. For reference, local displacement is offset above in blue (–). a-b) Trajectories dominated by mechanical noise. c) A low area example of a trajectory with arc length equal to the expected displacement (L_N = 0). d) A high area example of a trajectory with L_N = 1.0.

to their original positions, whereas those on the right have escaped their original particle positions. As strain amplitude is increased past yield, particles transition from below the threshold to above it. In the case of whole cycles (Fig. 2.2b), particles remain below the threshold, except when the system is well above yield. These trends (inset of Fig. 2.2b) are qualitatively similar to those of $D_{2,min}$ shown in Fig. 2.1d. Notably, half of the particles are seen to escape over half cycles at the yield point. Also, nearly all of the particles are seen to escape over whole cycles at the strain amplitude of equal elasticity and plasticity (~ 17%) seen in figure Fig. 2.1c.

A natural way to glean more information is to consider the components of the displacement vectors in each coordinate direction. To do this we plot Poincarè sections of spatial displacement (every half cycle) in Fig. 2.3. Plots of the remaining strain amplitudes are included in the supplemental information. Here we again find confirmation that there is a deviation of attractors above and below yield. It is seen that the attractor at the origin diminishes with strain amplitude, but is still present. The attractor representing escapes is visualized as a cloud of points and grows outward

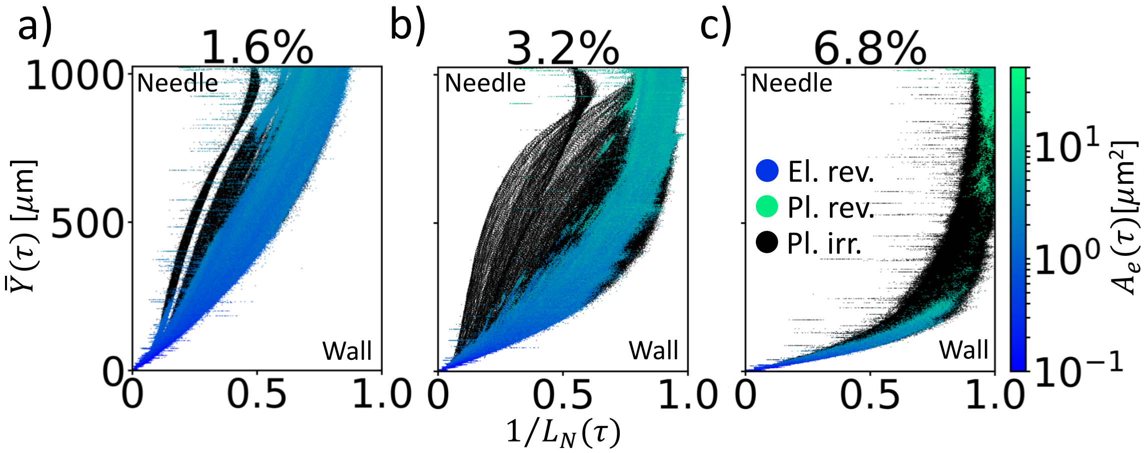

Figure 2.5: Inverse normalized arc-lengths ($1/L_N$) and enclosed area (color bar) compared with the mean particle position between the needle and the wall. Irreversible particles are shown in black. a) Below yield the system is dominated by reversibly elastic, and irreversibly plastic particle trajectories. All trajectories have $1/L_N < 1.0$, indicating that trajectories are long relative to the displacement field. This means they are dominated by mechanical noise. b) Near yield, plastically reversible particles emerge near the needle. Overall the $1/L_N$ shifts nearer to one (especially the plastically reversible particles) indicating a transition to low mechanical noise relative to affine displacements. c) Particles in the middle of the channel are exclusively plastically irreversible. Plastically reversible particles reach $1/L_N \sim 1.0$ indicating that these trajectories are completely dominated by background displacement, while simultaneously enclosing high area. It is worth noting that not a single particle is observed to have a $1/L_N >> 1.0$.

with the increase of strain amplitude.

We have observed no evidence of structure within either attractor, therefore we believe these to be fully chaotic. Interestingly, the attractor that emerges at yield has two periodic points (see the supplemental material for supporting information about periodicity). Remarkably, the periodic points are directly centered on the $\Delta y = 0$ axis. The whole cycle analysis shows two periodic points growing outward along the horizontal axis as well, with the caveat that they do not move outward as far as those shown in the half cycle cases (which is expected from Fig. 2.2b).

These results paint a picture of typical trajectories and their changes with strain amplitude. Particles predominantly move in the direction of needle displacement as expected. Moreover, particles that do not return are of a specific type: they are on track to return, but their trajectories get cut short by the end of the cycle. I.e. by the end of each half cycle of strain they have not returned *yet*. Crucially, this implies that distance travelled by a particle is linked with the type of trajectory it creates (Fig. 2.4).

These findings inspire the inspection of a different phase space that can be thought of as a version of efficiency of dissipation. We recall that enclosed area is thought to correspond to energy dissipation. Therefore, it is natural to think of arc-length of an enclosed area as a way of measuring the efficiency of that energy dissipation. In other words, we measure how far a particle needs to travel to dissipate a certain amount of energy to its surroundings. However, particles will exhibit very different arc-lengths depending on how close they are to the wall; if a particle is very close to the wall it will hardly move at all. This leads us to normalize each trajectory's arc-length by the displacement that would be expected given its average y position, assuming a linear strain profile from the needle to the wall as shown in Fig. 2.1b. From geometry of similar triangles, this length is $2\gamma_0\delta(x,t)$. We define normalized arc-length as $L_N = \frac{L_{arc}}{2\delta_0\langle Y\rangle}$.

The efficiency spectrum introduced above is shown (indirectly) in Fig. 2.5. This set of plots show the mean particle position between the instrument needle and wall, $\overline{Y}(\tau)$, as a function of $1/L_N$, where τ is cycle number. We choose the inverse of L_N for reasons apparent below. We show data for three strain amplitudes ranging from below yield (Fig. 5a, 1.6%) to well above yield (Fig. 5c, 6.8%). For the case below yield (Fig. 2.5a), particles trace out a wide range of $1/L_N$ relative to the expected displacement (based on needle displacement). However, each particle has an $1/L_N$ that is below one. This indicates that the arc lengths are long compared to the expected linear displacement field. These relatively long particle displacements are a result of erratic (i.e. non-smooth) particle paths. These erratic motions are due to small perturbations to the material's underlying energy landscape caused by small displacements of neighboring particles. This effect is commonly known as mechanical noise [173]. An example of such a trajectory is shown in Fig. 4(b). Interestingly,

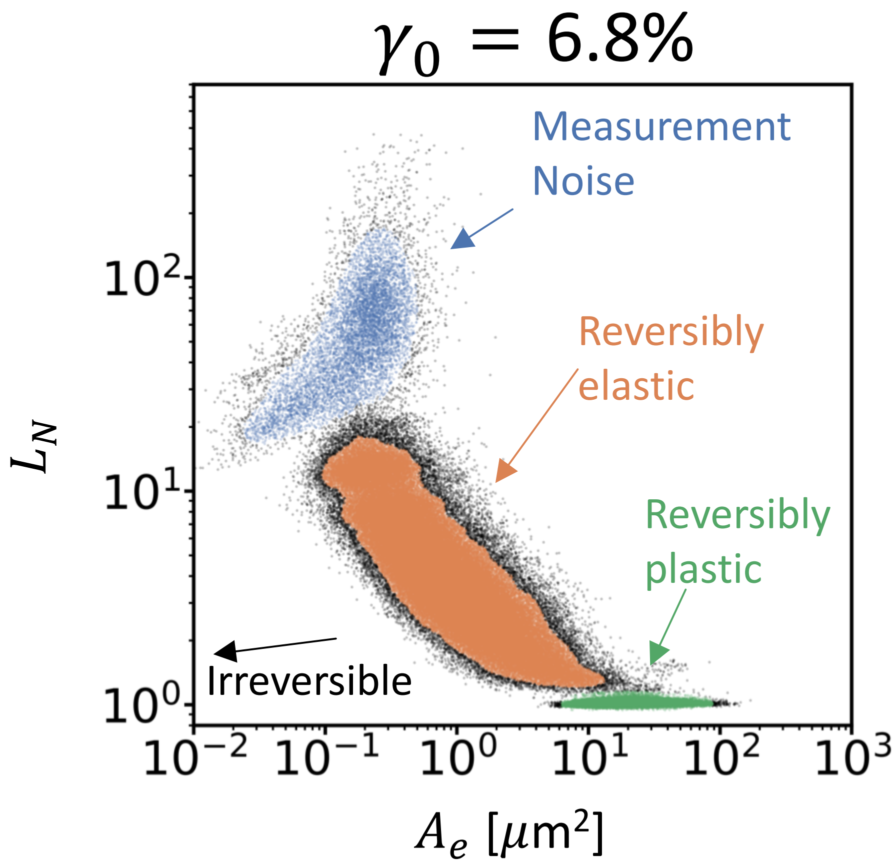

Figure 2.6: A direct view of the efficiency space described. Normalized arc-length, L_N, is plotted against Enclosed area, A_e. Above yield clusters emerge that correspond to the reversibly plastic, in addition to the reversibly elastic cluster. Colored clouds of points demonstrate the HDBSCAN clustering algorithm employed for our data. Here, the strain amplitude is 6.8%

the lowest values of $1/L_N$ are near the wall, implying that the effect of mechanical noise is much higher there than near the needle where displacements are largest. The enclosed area of trajectories is small relative to higher strain amplitude cases, which means that particles are predominantly elastically reversible in this case.

Near yielding (Fig. 2.5b), we observe the appearance of trajectories that are reversible and plastic (green points), predominantly near the needle. $1/L_N$ shifts closer to one near the needle (and even the center of the channel), reflecting a decrease in the importance of mechanical noise relative to the low-strain case. This effect corresponds to the emergence of much higher enclosed areas, constituting plastic reversibility. Finally, well above yield (Fig. 2.5c), $1/L_N$ reaches one at the needle meaning that mechanical noise is nearly negligible (for the case of particle motion) and trajectories are mostly smooth (see Fig. 4c,d). Additionally, these reversibly plastic trajectories reach enclosed areas that are almost an order of magnitude larger than in lower strain amplitudes. Crucially, the particles in the center of the channel become nearly completely irreversibly plastic.

These results seem to imply that yielding is characterized by particles that dissipate energy with a minimized arc-length. In contrast, particles below yield dissipate very little energy while exhibiting large arc-lengths (high mechanical noise; see trajectories in Fig. 2.4a-b). Randomized particle motions due to mechanical noise dominate the particle system below yield. As strain is increased, this motion becomes smaller relative to the overall strain-driven displacement. Once above yield, the effect of mechanical noise is negligible relative to the local displacement, resulting in arc-lengths that are smaller relative to the local affine displacement field. Crucially, arc-lengths smaller than the linear displacement are not observed (Fig. 2.4c). Once this limit is reached, enclosed areas grow and the system begins to dissipate energy (Fig. 2.4d).

A direct view of the efficiency space described above is shown in Fig. 2.6, where L_N is plotted against A_e. Here separate clusters are immediately apparent. Above yield, a large A_e cluster emerges, which corresponds to the reversibly plastic state described above. Because irreversible particles do not enclose an area, they are off of the logarithmic horizontal axis.

The presence of attractors and states brings up the question of how particles may be transitioning from one half cycle to the next. We perform a cluster analysis to answer this question. The efficiency spectrum of enclosed area and normalized arc-length provides a convenient way to determine clusters of elastically reversible, plastically reversible, and irreversibly plastic trajectories. Once these clusters are determined, questions of how many particles transition between states from one cycle to the next can be answered quantitatively.

The colored clouds of points shown in Fig. 2.6 reflect the detection of clusters by

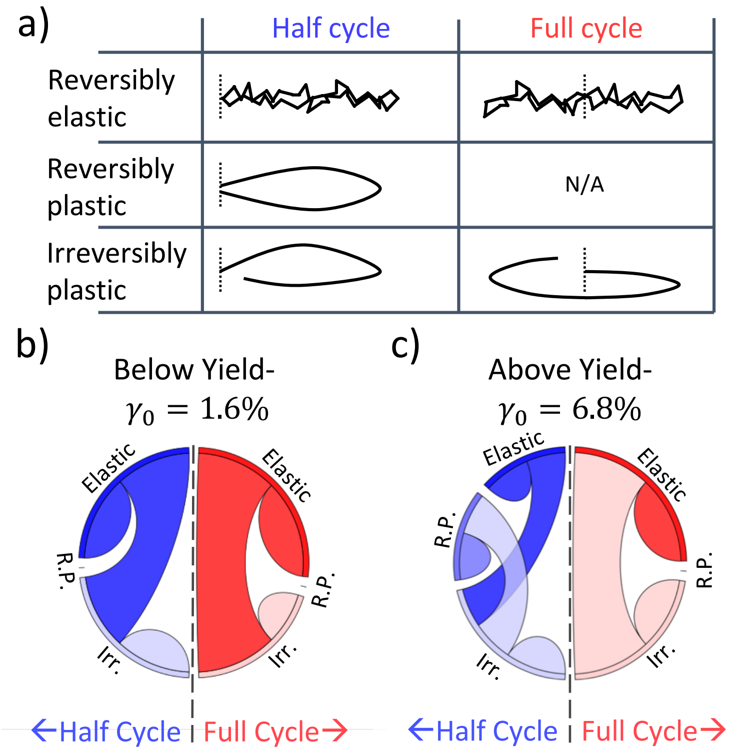
a)
Half cycle
Full cycle
Reversibly elastic
Reversibly plastic
N/A
Irreversibly plastic
b)
Below Yield-
$\gamma_0 = 1.6\%$
Elastic
R.P.
Irr.
c)
Above Yield-
$\gamma_0 = 6.8\%$
←Half Cycle
Full Cycle→

Figure 2.7: a) Cartoon representation of different particle trajectories corresponding to those shown in Fig. 2.4. b&c) Chord diagram representations of particle's inter-cycle transitions between apparent clusters within Fig. 2.5a&c. Widths of cords at either end represent the log of the numbers of particles transitioning from that state. Color of each cord corresponds to the state that has more particles transitioning. b) Below yield for both the half cycles and whole cycles there is no presence of the reversible plastic cluster. c) Above yield, half cycles exhibit a reversibly plastic cluster, whereas the whole cycles do not. The reversibly and irreversibly plastic states do not exchange particles.

the HDBSCAN algorithm. One observation is that the algorithm does not designate quite all of the particles around the borders of the designated clusters; it leaves out 0.30% of the total points. This is due to large differences in the density of points within the designated clusters and the outer fringes; there are narrow, 'loose and fuzzy' edges. A second note is that there is a cluster labeled as 'measurement noise'. These points correspond to particles within a few particle diameters of the wall. Trajectories are highly noisy for these particles because there is optical disturbance from the wall. This cluster comprises 0.32% of the overall points. These points are discarded.

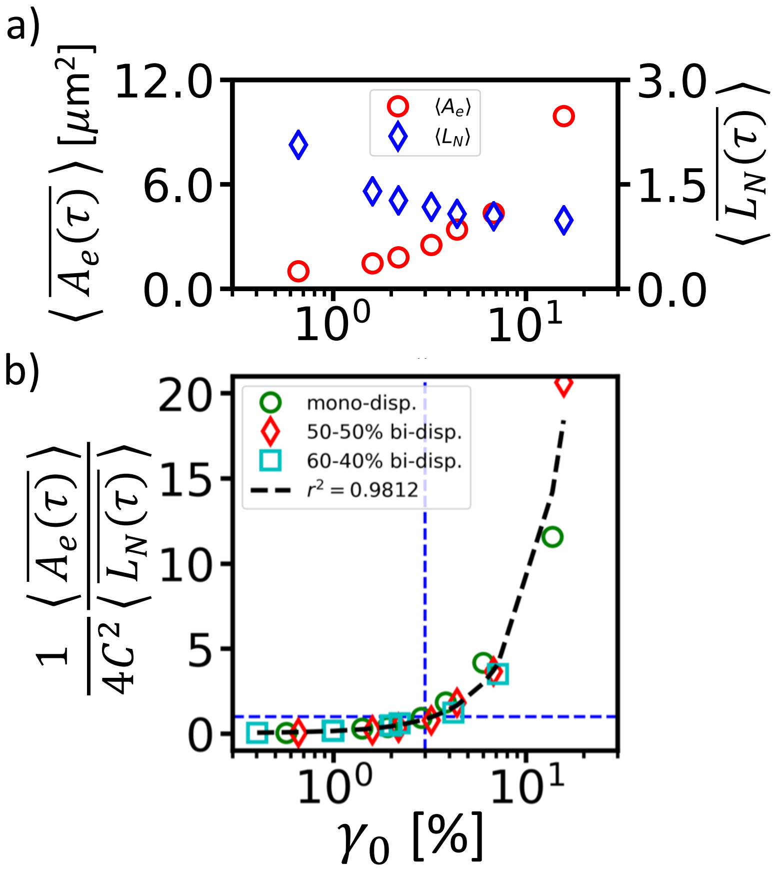

Figure 2.8: Trends in average enclosed area and normalized arc-length as a function of strain amplitude. a) With increasing strain amplitude, average enclosed area, $\langle A_e \rangle$ grows rapidly. With strain amplitude, average normalized arc-length, $\langle L_N \rangle$, drops monotonically toward an asymptote at unity. b) Taking the square root of the ratio, $\langle A_e \rangle / \langle L_N \rangle$ we find a linear collapse between three colloidal systems of various amounts of disorder. Moreover, this collapse passes through unity at the yield point ($\gamma_0 \sim 0.3$).

To display our results quantitatively, we have elected to use two chord diagrams (Fig. 2.7b,c). These plots give a quick but quantitative assessment of the numbers of transitions from one state to the next. Thickness of chords indicate the logarithm (base 10) of the number of particles transitioning out of one state into another; e.g. a chord that is wide on one end and narrow on the other indicates more particles leaving the wide state than from the narrow state. This functions almost like an arrow, where the widths indicate the logarithm of the number transitioning.

As a summary of each state found, we have included a table of cartoon depictions of the observed particle paths (Fig. 2.7a) We note here that even though reversibly plastic trajectories are not observed over whole cycles, the trends indicate that they may occur at higher strain amplitudes than are presented here. The first observation to draw from Figure 2.7 is that particles readily transition between the elastic and plastically reversible states both over half and whole cycles. A second observation is that both elastically reversible and plastically reversible particle trajectories do not transition between each other, implying that they are separate populations. This is a break from intuition, which would have that particles transition from elastically reversible to reversibly plastic and then to plastically irreversible.

Two findings have been made: reversibly plastic and elastic states exist independently of each other in time, and the particles fall into these states based on where they are within a melting front between the needle and the wall. The depth of this melting front, as characterized by the normalized arc-length, increases with strain amplitude. Crucially, we have seen that the enclosed area increases rapidly above the yield point and that the normalized arc-length decreases monotonically towards unity. In Fig. 2.8a we present both of these quantities averaged in time and space, relative to strain amplitude. Remarkably, taking the ratio of these two quantities reveals a parabolic relationship with strain amplitude, as shown in Fig. 2.8b. This functionality suggests a relationship of the type

$$\frac{\gamma_0}{\gamma_{cr}} = \frac{1}{2C}\left(\frac{\langle\overline{A_e(\tau)}\rangle}{\langle\overline{L_N(\tau)}\rangle}\right)^{0.5} \tag{2.1}$$

where $\gamma_{cr} = 3.0\%$ is the critical strain amplitude indicating yield. The two is included to account for the fact that there is material being sheared on either side of the needle. Eq. 2.1 is a dimensionless scaling, quantifying plastic loss as a function of strain amplitude. That is, this equation uses Lagrangian particle dynamics to describe the yield transition.

Enclosed area of limit cycles is related to dissipated energy, which has been measured previously to increase rapidly beyond the yield point [105, 106]. Therefore these results lead us to conclude that the ratio, $\langle\overline{A_e(\tau)}\rangle/\langle\overline{L_N(\tau)}\rangle$ (having units of μm^2) is a direct Lagrangian measure of dissipation within the entire system. (L_N appearing here in the denominator is the reason we above plot against $1/L_N$ in Fig. 2.5)

To explain the origin of the coefficient C we must consider the subtlety of plasticity. As particles rearrange, they must squeeze past each other. This relaxation process results in local forces acting between particles. These forces on the bulk scale give rise to fluctuating normal forces on the needle and walls. This is known as Reynolds dilatancy [128]. The walls are fixed in space, whereas the needle is constrained only by contact with the particles on either side of it. These normal force fluctuations cause the needle to displace at low frequencies as material on both sides of the needle relax. However, this length-scale must adhere to a value that depends on the particle interaction strength and the sizes of particles themselves. In these experiments, we observe this value to be $C = 1.04 \pm 0.15 \mu m [95\%]$.

2.4 Discussion and Conclusions

In this paper we investigated the Lagrangian dynamics of constitutive particles within a 2D soft jammed material spanning strain amplitudes from below yield to above. Our first finding is that the average displacement distance of particles from the beginning of a cycle to the end increases monotonically with strain amplitude in a qualitatively similar way to the number of non-affine events (both reversible and irreversible)(Fig. 2.1d and Fig. 2.2b inset). Moreover, these displacements are predominantly in the direction of shear, which is linked to particles falling short of returning to their original positions (Fig. 2.3). This in turn implies particle motions have slowed, dissipating energy; thus there is importance to measuring area and arc-length as proxies for energy dissipation and a material's ability to dissipate energy (efficiency) respectively.

As has been noted previously, [173] particles below yield are found to display erratic motions about a mean path (reversibly elastic). The mean path is the expected local displacement due to a linear strain field. These erratic motions are caused by mechanical noise from perturbations of the energy landscape (Fig. 2.4a&b and Fig. 2.5). However, above yield particles near the shearing surface are found to instead have smooth trajectories with limit cycle trajectories (reversibly plastic)(Fig. 2.4c&d and Fig. 2.5). Moreover, any particle that does not maintain these limit cycles, will not return to its initial position (irreversibly plastic). These non-returning particles are found everywhere throughout the channel below and near yield. However, well above yield, they are the only variety of trajectory found in the center of the channel.

More broadly, these may be signs of what is happening within the energy landscape; as particles transition from rough to smooth trajectories at the yield point, the energy landscape is transitioning from a fixed state with small perturbations, to being actively changed, but in ways that reverse as strain inverts. Irreversible particle trajectories represent local, permanent changes to the landscape and become dominant well beyond yield. The magnitudes of these changes has been shown in our system (Fig. 2.2b inset) and in simulations [104] to suddenly transition in strain amplitude, similar to a first order state transition. Strain is a temperature-like variable. Other indications that the yield transition is generally of the first order have been observed recently in simulations and theory [159] and experiments [55, 91].

We find that a quantification of this yield surface is the ratio of the average enclosed area (increasing with strain amplitude) and the average normalized arc length, L_N, (falling with strain amplitude). Area serves as a quantification of the energy dissipated by a limit cycle [211, 196, 181]. We posit that the inverse of L_N is a measure of how efficiently a particle is dissipating energy relative to a given strain amplitude. Using both of these concepts, we present a non-dimensional quantification of plastic dissipation based entirely on the Lagrangian dynamics of the constituent particles (Eq. 2.1 and Fig. 2.8).

More generally, this quantification works because it captures variations in particle response between the stationary and shear surfaces. While enclosed area of trajectories is not an applicable concept outside of oscillatory systems, $1/L_N$ is applicable and should be measured in other systems. In this paper, we describe a spatial transition in $1/L_N$ that is associated with the yield transition, and the location of this transition penetrates farther from the shearing interface the more strain is increased. This is reminiscent of a melting front, and consistent with dynamics observed in dry and immersed granular systems [115, 103, 93, 92]. In particular, steadily-sheared granular systems exhibit: a decreasing shear rate away from the shearing interface; a fluidized layer at the shearing interface where particles move ballistically; and a transition associated with a critically-low shear rate to caged dynamics characteristic of glassy materials [68, 92]. The thickness of the fluidized layer has been found to be proportional to the applied shear rate [93], and the melting front has been identified as a yield surface marking the transition to (athermal) granular creep. Seeking similarities in the melting-front dynamics of these systems and our experiments is an exciting next step, which will help to reveal whether the creep-flow transition in granular systems is a similar state transition to what we observe here.

We have presented echoes within a colloidal system under oscillatory stress of phenomena observed in granular systems under steady shear. This introduces evidence that may help answer a tantalizing question: how is the particulate behavior of amorphous systems of greatly variable length scales, various interaction forces and complicated shapes related to each other? And how is that related to the bulk response? Some observations have been made previously: yield strain within amorphous materials as a whole is ~ 3% [50]; in granular systems, dimensionless strain rates are related directly to the volume fraction [33, 101]. The results presented here indicate that particle displacement relative to the expected strain may be a useful tool in understanding the response of amorphous materials more generally. This parameter is accessible and should be investigated further in a myriad of systems.

2.5 Appendix

Within the main body of the text, two attractors were shown in Fig. 2.3 and discussed. The point at the center of all Poincarè sections is an attractor corresponding to particle returning to their original positions. Two additional points develop with increasing strain amplitude, constituting a bifurcation. In the main body it was stated that these points are periodic within the same attractor. In Fig. 2.9a we supply evidence. By numbering sequentially, T, each half cycle of every particle's trajectory we display where each particle is during even and odd numbered half cycles. In the Poincarè section in Fig. 2.9a we show that a binned average of the remainder of T corresponds to each point. Particles on the right overwhelmingly are of odd half

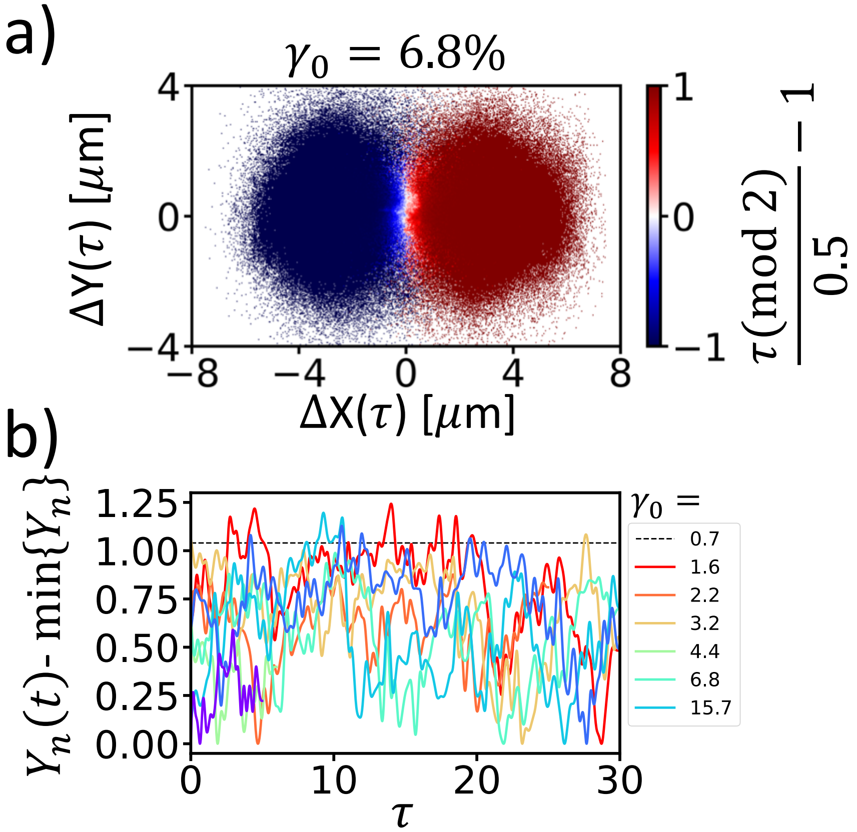

Figure 2.9: a) Horizontal and vertical axis are a Poincarè section well above yield. Color represents a binned average of the remainder of half cycle count divided by two, shifted so that even numbers of half cycles are blue and odd half cycles are red. The left half of the attractor is composed of even half cycles and the right is made up of odd half cycles. Therefore particles must be oscillating between both points. b) The range in the the displacement of the needle in the direction normal to shear plotted against cycle, τ, for all strain amplitudes. The average difference between the highest and lowest displacement is about one here. $C = 1.04 \pm 0.15 \mu m[95\%]$ is shown as a dashed gray line (-).

cycles, whereas particles on the left are overwhelmingly even half cycles. This means that particles are switching from the right to the left points periodically throughout a cycle. Therefore, the attractor is made up of two periodic points.

Within the main body of the text, it is mentioned that the characteristic displacement length, C, of the shearing tool perpendicular to shear is ~ $1.0 \mu m$. In Fig. 2.9b we plot the y-position of the needle minus the minimum position versus time (in units of cycles). The highest peak for any given strain amplitude corresponds to an estimate of C. The average of these peak heights across all three samples is $C = 1.04 \pm 0.15 \mu m$ over a 95% confidence interval.

Chapter 3

The system wide link between particle arrangements and their dynamical responses

3.1 Introduction

For many amorphous solids, i.e., solids without long-range order, a threshold stress exists beyond which the material starts to deform plastically (yield) and flow like a liquid. These yield stress materials, which range from foams and colloids to cement and metallic glasses, have constituents and dynamics that vary widely across length and time scales [14, 26, 154]. Nevertheless, they are unified by two features: the cross-over transition from solid- to liquid-like behavior and a nonlinear viscosity response to external stress (shear thinning) [200]. Ultimately, to understand these nonlinear mechanical processes, we need a detailed picture about how shear couples to microscopic structure and relaxation. If successful, this understanding could lead to improved processing of amorphous metals via stress-induced control of microstructure [65, 212].

To this end, useful models have been developed to characterize the structural origin of plasticity in amorphous solids. Shear transformation zone models, for example, posit the existence of mechanically weak regions in amorphous solids analogous to crystalline defects, and then they focus (largely) on the kinetics associated with localized plastic events [66]. The softer regions are believed to facilitate or accelerate rearrangements nearby. This general phenomenology of dynamic heterogeneity is observed in experiments [193] and computer simulations [66], and is supported by first-principle Mode-Coupling and Random First-Order Transition theories [83, 114, 130]. Nevertheless, identification of mechanically weak regions from *static* sample structure, e.g., before plastic events occur, remains a challenge.

In a different vein, thermodynamic predictors based on excess entropy (S^{ex}) have shown promise for explaining nonlinear mechanical phenomena in complex fluids [187, 62, 119, 1, 61, 96]. Excess entropy concepts developed from studies of liquids rather than solids and enable comparison of macroscopic system-averaged structural and dynamical quantities. S^{ex} is a structural order parameter defined as the difference between system thermodynamic entropy and that of an equivalent ideal gas [16]. For typical liquids, S^{ex} derives mainly from pair correlations of its constituents [62] and is readily evaluated by experiment [1, 133]. Excess entropy accurately predicts transport coefficients of simple and complex fluids in equilibrium using their static structure [191, 94, 190, 147, 118, 1, 120, 175, 133, 224, 156, 135, 125]. Recently, in computer simulations, S^{ex} has been applied to supercooled liquids under steady-state shear; the shear-dependent relaxation time of the supercooled liquids was found to scale with S^{ex} [96], thereby revealing a simple structural connection to shear-thinning induced relaxation. This intriguing discovery has not been tested experimentally. Moreover, the concept of excess entropy scaling has not been applied to understand plastic flow in amorphous solids, nor in materials driven into more general non-stationary states.

In this contribution, we investigate the connection between shear rate, relaxation time and excess entropy of plastically deformed matter in non-stationary states. We use a custom-made interfacial stress rheometer [202, 182, 105, 106] to apply oscillatory shear at different strain amplitudes to an oil-water interface (Fig. 3.1a, see *Materials and Methods* for details). A series of disordered, two-dimensional colloidal solids are

Table 3.1: Summary of colloidal monolayers. σ: particle diameter, ϕ: packing fraction, d: mean interparticle separation, $\Gamma_{\max}$: strain amplitude

Sample	σ (μm)	ϕ	d (μm)	$\Gamma_{\max}$
A (bi-disperse)	4.1,5.6	43%	7.4	5-16%
B (monodisperse)	5.6	32%	7.7	8-16%
C (bi-disperse)	1.0,1.2	32%	9.8	5-8%

prepared at the oil-water interface (Fig. 3.1b). Their translational and orientational correlation functions do not exhibit long-range order (see the Supporting Information (SI)). The disordered samples are driven by the applied oscillatory shear, and concurrently, the trajectories of individual particles in the samples are captured by video optical microscopy and standard tracking software.

3.2 Results and Discussion

From particle position data during oscillatory shear, we compute strain rate, the relaxation rate/time associated with plastic flow, and the sample excess entropy. The relaxation time exhibits a power-law scaling with shear rate, a characteristic of shear-thinning behavior. Furthermore, phase-shifts between the oscillatory signals revealed a constant lag time between plastic shear rate and plastically induced relaxation rate, and a different lag time (proportional to the instantaneous relaxation time) between relaxation rate and excess entropy. These delay-intervals (phase-shifts) uncover novel connections between shear rate, plastic flow induced relaxation, and structure of the samples in non-stationary states. Surprisingly, we find that relaxation time/rate and excess entropy data measured at different strain amplitudes collapse onto a single master exponential scaling curve which depends only on sample type. In total, the work introduces an analysis framework based on excess entropy scaling to understand plastic flow in both stationary and non-stationary states, and the findings suggest that information about the relaxation history of an amorphous material can be deduced from its current static structure.

Briefly, the solid-like monolayers consist of colloidal spheres with different diame-

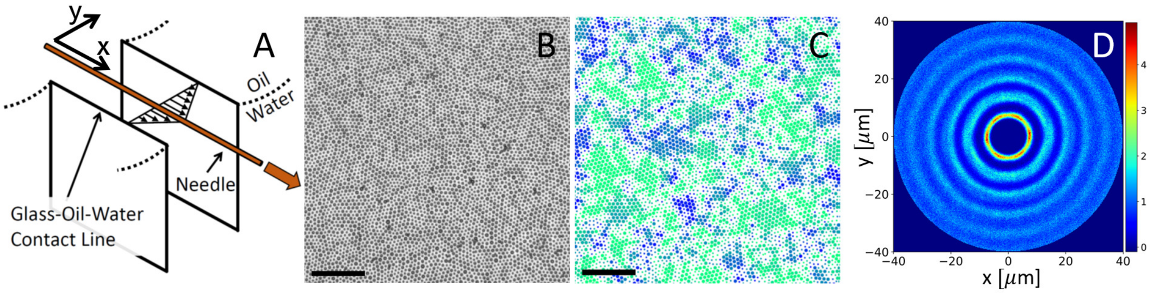

Figure 3.1: (a) Schematic of the interfacial stress rheometer. A sinusoidal magnetic force is imparted to the interface-bound magnetic needle, which in turn introduces oscillatory shear stress at the oil-water interface. The parallel and perpendicular directions with respect to the needle motion are defined as the x- and y-axis, respectively. (b) Micrograph of bi-disperse colloidal particles at the oil-water interface from sample A. (c) Sixfold bond orientation order, ψ_6, measured from particles in (b). Colors help to indicate the lattice director (orientation) as a guide for the eye to help discern ordered and disordered domains. Dots with large size indicates $|\psi_6| > 0.9$, and small dot size indicates $|\psi_6| < 0.9$. The scale bars in (b) and (c) are 100μm. (d) A pair correlation function, $g(x, y)$, measured from particle positions in (b) exhibits strong anisotropy due to ordered domains.

ters (σ), surface charge densities, and packing fractions (ϕ) (see Table. 3.1 and *Materials and Methods*). In combination, these factors determine interparticle separation (d), sample structure (see Fig. 3.1c,d and SI), shear moduli, and plasticity

[105, 106]. Rheology measurements of the samples exhibit elastic behavior at small strain amplitudes and yielding behavior when the strain exceeds about 3% (see SI). Herein, we focus exclusively on strain amplitudes above yield point (e.g., larger than 5%, see Table. 3.1).

We first use the particle trajectory data to measure and compare shear rates and shear-induced relaxation times. The shear strain, $\Gamma(t)$, at time t quantifies the sample's *affine* deformation, which follows the oscillations of the needle motion. We compute $\Gamma(t)$ by taking average of the measured y-dependent *local* strain, $\gamma(y, t)$ (see *Materials and Methods*). Figure 3.2a shows that $\dot{\Gamma}(t)$ follows the driving sinusoidal function set by the external force, and that it exhibits measurable fluctuations about the sinusoidal function too. Note, fluctuations of $\Gamma(t)$ about the driving stress have been seen in plastically deformed bidisperse polycrystals in computer simulations [87, 204]; these fluctuations were attributed to intermittent yielding along grain boundaries and become weaker when the sample has smaller crystalline domains.

We use *nonaffine* particle motions to evaluate sample relaxation behavior [231, 96]. At time t, the self-part of the intermediate scattering function is,

$$F_s(t,\tau) = \frac{1}{N}\langle\sum_{j=1}^{N}\exp[\frac{2\pi i}{d}|\Delta\vec{r}\,'_j(\tau)|]\rangle. \tag{3.1}$$

Here N is the number of particles and $\Delta\vec{r}\,'_j$ the nonaffine displacement of the j-th particle, that is, the residual after the affine displacement has been subtracted from the total particle displacement, $\Delta\vec{r}_j$. (See *Materials and Methods* and SI for how to compute $\Delta\vec{r}\,'_j$ from $\Delta\vec{r}_j$.) The brackets, $\langle\cdots\rangle$, represent a time average over the period $[t-\delta t/2, t+\delta t/2]$ ($\delta t = 2.5$s is one quarter of the shear cycle). The duration of the measurement is thus δt. Ideally, $F_s(\tau)$ should decay to below $1/e$ at $\tau = \delta t$ to extract the relaxation time. However, we will soon show this is not necessary.

Figure 3.2b shows examples of $F_s(t,\tau)$ at two times where the $\dot{\Gamma}$ values are different; these $F_s(t,\tau)$'s decay at different rates, indicating shear-dependent relaxation behavior. $F_s(t,\tau)$ is well fit by the function,

$$F_s(t,\tau) = A\exp[-(\tau/\tau_\alpha)^\beta], \tag{3.2}$$

where τ_α is the α-relaxation time measured in the time-interval centered on t, and $A \simeq 1$ is a constant prefactor (see SI). Since we can fit $F_s(\tau)$ data before it decays to $1/e$ to obtain τ_α, we can estimate τ_α from measurements with duration (δt) shorter than τ_α (see SI for details). Interestingly, we find $\beta > 1$ (compressed exponential) throughout the shear cycle in all samples. This finding confirms the expectation that particle configurations, when driven by external forces, relax/reorganize faster than would occur if driven by exponential diffusive motions alone. A few studies have also reported $\beta > 1$ phenomena [46, 141, 137, 143, 6, 80]; in these cases, ballistic motions of constituents were found to accompany the accumulation and release of internal stress [215]. In our experiments the nonaffine mean-square-displacements (MSD's),

$\langle \Delta r'^2(\tau) \rangle$, exhibit super-diffusive behavior, that is, $\langle \Delta r'^2(\tau) \rangle \sim \tau^p$ with $p > 1$ (see SI); by analogy to prior work, we believe the measured compressed exponential decay of $F_s(t, \tau)$ is caused by super-diffusive particle motions. Note, we also investigated other alternative explanations for the compressed exponential decay of $F_s(\tau)$ (see SI).

Using the $\dot{\Gamma}(t)$ and $\tau_\alpha(t)$ data, we next investigate how shear influences relaxation in the *non-stationary* regime. Figure 3.2c compares $|\dot{\Gamma}(t)|$ and $\tau_\alpha^{-1}(t)$ measured from sample A ($\Gamma_{\max} = 16\%$) as a function of t; here, the absolute shear rate is used because we expect the shear direction to have little influence on relaxation rate. This comparison clearly demonstrates that the relaxation rate lags the shear rate by a time interval, $\Delta t \simeq 0.8$s (see *Materials and Methods* and SI). This lag time hints at a causal relation between shear and shear-induced relaxation processes. Moreover, the amplitude of $\tau_\alpha^{-1}(t)$ follows $|\dot{\Gamma}(t)|$.

For a more quantitative comparison, we examine our data in the context of the non-Newtonian relationship between shear rate and relaxation time that has been found in steady-state [206, 19]:

$$\tau_\alpha \sim (1 + \dot{\Gamma}/\dot{\Gamma}_0)^\mu. \tag{3.3}$$

Here, $\dot{\Gamma}_0$ is the shear rate associated with onset of non-Newtonian viscous response behavior, and $\mu < 0$ is a power law exponent characterizing shear-thinning behavior.

In oscillatory measurements, Eq. 3.3 has been established between the *mean* (or *maximal*) viscosity and shear rate during multiple shear cycles [45]. To our knowledge, this relation has not been used to describe the connection between the *instantaneous* viscosity (or relaxation time) and shear rate in non-stationary samples. Despite the phase-shift between shear rate and shear-induced relaxation rate, we might expect our data to follow Eq. 3.3 with $\dot{\Gamma}$ being replaced by its weighted time average, $\langle |\dot{\Gamma}| \rangle_{\delta t}$, over the time-interval $[t - \delta t/2, t + \delta t/2]$ (that is, the same window wherein $\tau_\alpha(t)$ is evaluated, see *Materials and Methods* and SI about calculation of $\langle |\dot{\Gamma}| \rangle_{\delta t}$). To test this hypothesis, we plot $\tau_\alpha(t + \Delta t)$ versus $\langle |\dot{\Gamma}(t)| \rangle_{\delta t}$ measured from sample A in Fig. 3.2d. Remarkably, the data from the sample A sheared at three different strain amplitudes collapse onto

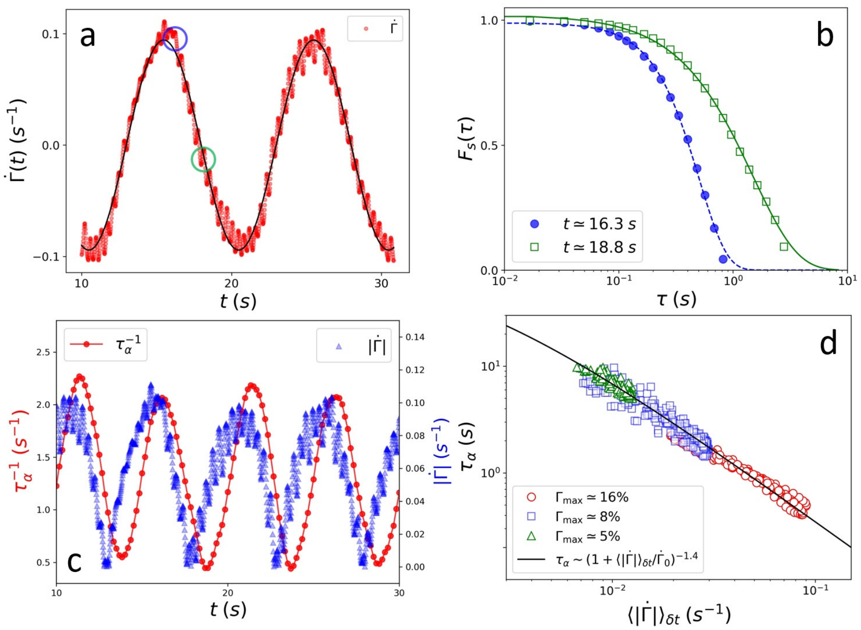

Figure 3.2: Dynamics in sample A (a) Instantaneous shear rate, $\dot{\Gamma}(t)$, versus time, t. The solid line is the sinusoidal fit, $\dot{\Gamma}(t) = 0.096\sin(\omega t)$. (b) The self-part of the intermediate scattering function, $F_s(\tau)$, measured at the two times indicated by same-color circles (green, blue) in (a). The dashed and solid lines are fits using Eq. 3.2, with $\tau_\alpha = 0.5$ and 2.3 sec and $\beta = 1.3$ and 1.5 at $t = 16.3$ and 18.8 sec, respectively. (c) Relaxation rate, $\tau_\alpha^{-1}(t)$, versus time, t (red circles). The magnitude of shear rate, $|\dot{\Gamma}(t)|$, is also plotted (blue triangles) for phase-shift comparison. (d), The measured relaxation time, $\tau_\alpha(t + \Delta t)$, versus time-averaged shear rate, $\langle|\dot{\Gamma}(t)|\rangle_{\delta t}$, from three experiments with different $\Gamma_{\max}$ values. The solid line is the best fit using $\tau_\alpha \sim (1 + \langle|\dot{\Gamma}|\rangle_{\delta t}/0.0017)^{-1.4}$.

a single master curve; the best fit using Eq. 3.3 gives $\dot{\Gamma}_0 = (1.7 \pm 0.5) \times 10^{-3}\ s^{-1}$ and $\mu = -1.4 \pm 0.3$. Interestingly, the fitted $\dot{\Gamma}_0$ in our sample is of the same order of magnitude as the onset shear rates of non-linear viscous response in molecular glasses [206]. The fitted μ is similar to those measured in dense suspensions of soft colloidal particles [122]. This finding suggests an interesting new way to characterize shear-thinning behavior in a non-stationary (e.g., oscillatory) measurement. Note, also, while in principle the lag time, Δt, between shear-rate and relaxation time may be a complex function of shear rate, in our samples it suffices to use a constant lag time.

Next, we compute excess entropy from particle position data and explore whether excess entropy scaling laws can be applied in systems experiencing *non-stationary* (oscillatory) shear. If the scaling relation still holds, then by implication, sample static structure can provide information about relaxation induced by plastic deformation. Previously, viscosity, diffusion coefficients, and relaxation times have been found to obey a simple excess entropy scaling law, $\tau_\alpha \sim f(S^{ex})$, for a wide variety of materials [191, 94, 190, 147, 118, 120, 175, 224, 156, 135, 125] spanning different particle type, size, density, interaction, temperature, material phase, and even shear rate [118, 96]. Importantly, S^{ex} is well approximated by the two-body contribution, S_2, which is readily determined from scattering or imaging experiments [1, 133, 224].

To this end, we compute the time-dependent sample pair correlation function, $g(r)$, using particle positions at time t. Note, we employ particle coordinates in a single video frame at time t for determination of $g(r)$; these particles are the same as used above in computing $\dot{\Gamma}(t)$ and $\tau_\alpha(t)$. Examples of $g(r)$ at two times, $t = 16.7$ and 19.2 s, are shown in Fig. 3.3a. These $g(r)$'s exhibit quasi-long-range order extending out to 10 shells of neighbors; the extended correlations are indicative of presence of many small crystalline domains (see Fig. 3.1c and SI). By comparison, $g(r)$ from sheared glass-forming liquids typically exhibits only 3 well-defined peaks (e.g., see Refs. [231, 96]). The correlation lengths obtained from the spatial correlations of translational and orientational order also confirmed that the samples are more ordered than traditional glasses but less ordered than crystals/polycrystals (see SI).

The peaks of $g(r)$ evolve subtly throughout imposed shear cycles (Fig. 3.3a insets); these changes are indicative of shear-induced restructuring. The comparatively high peaks in $g(r)$ at $t = 19.2$ s compared to $t = 16.7$ s suggests a more ordered structure in the former case. The differences in peak height at different times are rather small and are in accord with measurements in sheared molecular glasses [231, 119, 96]. From the time-dependent $g(r)$ data, we compute S_2 versus t,

$$S_2 = -\pi\rho \int_0^\infty \{g(r)\ln[g(r)] - [g(r) - 1]\} r dr. \tag{3.4}$$

Here, ρ is sample particle number density. Equation 3.4 converges quickly after r reaches $5d$ (see SI); thus we choose the cut-off length, $r_{\text{cut}} = 10d$, as the integration

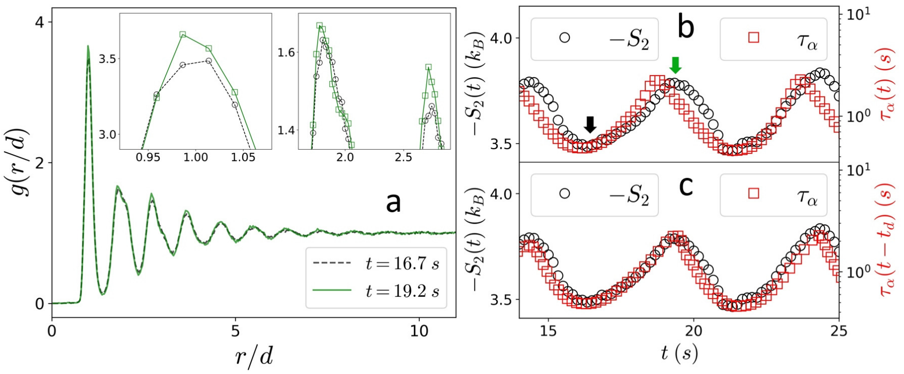

Figure 3.3: (a) Measured $g(r)$ from data taken at t = 16.7 and 19.2 s. The insets show the enlarged plots of the first (left inset), and the second and third peaks (right inset) of $g(r)$, respectively. (b) $S_2(t)$ versus t. $\tau_\alpha(t)$ is also plotted for comparison. The black and green arrows indicate t = 16.7 and 19.2 s, respectively. (c) $\tau_\alpha(t - t_d)$ is plotted versus time delay, $t_d(t) \simeq 0.3\tau_\alpha(t)$.

limit for computing S_2. We confirmed that with the same cut-off length Eq. 3.4 converges for the other two samples as well (see SI).A larger $-S_2$ value at t = 19.2 s confirms a more ordered structure, consistent with $g(r)$ data in Fig. 3.3a. Note that larger $-S_2$ are also accompanied by larger bond orientation order [216], suggesting the orientational order is coupled to translational order by shear (see SI).

Figure 3.3b presents $S_2(t)$ and $\tau_\alpha(t)$ as a function of t during the shear cycles. Notice that longer relaxation times, τ_α, are accompanied by larger $-S_2$ or, equivalently, more ordered sample structures. Taken together with the $\dot{\Gamma}(t)$ findings (Fig. 3.2c), we conclude that faster shear rates lead to shorter shear-induced relaxation times and more disordered resultant particle arrangements.

Further inspection of Fig. 3.3b reveals that the peaks of $-S_2(t)$ clearly lag behind those in $\tau_\alpha(t)$; by comparison, the lags between valleys are less apparent. A possible explanation is that $S_2(t)$ lags behind $\tau_\alpha(t)$ at all phase positions; this hypothesis is further supported by the hysteresis loops generated by the two functions (see SI). Based on this intriguing observation, we hypothesize that: i) the relaxation time measured at t is related to the sample structure (S_2) at a later time, $t + t_d$, and ii) the time delay, $t_d(t)$, is a function of $\tau_\alpha(t)$. We assume $t_d(t) \simeq h\tau_\alpha(t)$, where h is a constant throughout the shear cycles. To test this hypothesis we re-plot $\tau_\alpha(t - t_d)$

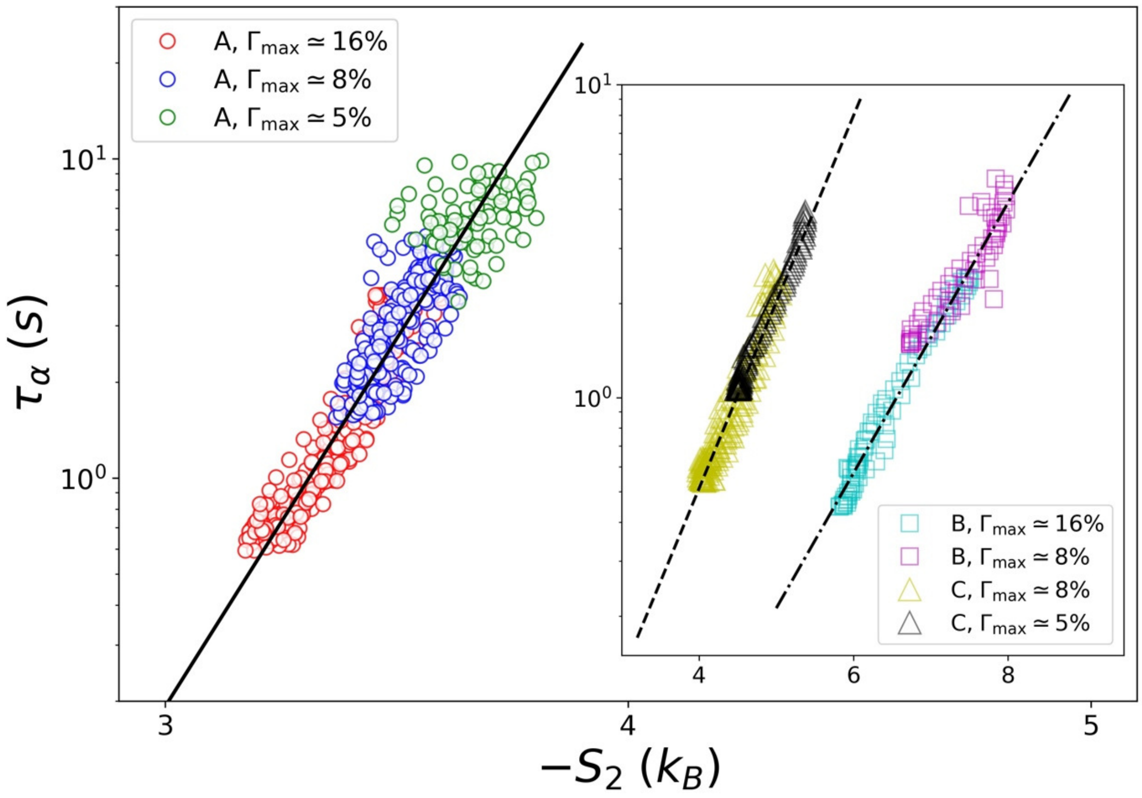

Figure 3.4: Delayed relaxation time, $\tau_\alpha(t-t_d)$, as a function of the excess entropy, $-S_2(t)$, measured from sample A with 3 different $\Gamma_{\max}$. Inset shows same data measured from sample B and C. The three data sets are fit using Eq. 3.5 with $c = 3.9 \pm 0.2$(solid line), $1.0 \pm 0.1(dash-dotline)$, and $1.4 \pm 0.1(dashedline)$ for sample A, B, and C, respectively.

in Fig. 3.3c. The relation $t_d(t) \simeq 0.3\tau_\alpha(t)$ best aligns the peaks and the valleys of $\tau_\alpha(t-t_d)$ and $-S_2(t)$ (see *Materials and Methods* and SI). Note, the choice of a linear function of τ_α to approximate t_d is empirical; t_d could have a more complex dependence on τ_α, $\dot{\Gamma}$, and their time-derivatives. This empirical finding that $t_d \sim \tau_\alpha$ suggests a picture wherein new structures driven by shear-induced relaxation evolve to their final form after a waiting time that is itself dependent on the relaxation process/timescale. Moreover, the introduction of this form for t_d enables comparison of τ_α versus S_2 across different times and conditions.

To this end, we investigate the scaling connection between τ_α and S_2 obtained at the different shear rates. Figure 3.4 shows $\tau_\alpha(t-t_d)$ as a function of $S_2(t)$ for all three samples listed in Table. 3.1 . For sample A, data from three strain amplitudes, $\Gamma_{\max} = 16,\ 8,$ and 5%, collapse onto a single master curve. Therefore, we confirm $\tau_\alpha(t - t_d)$ is a simple monotonic function of $S_2(t)$, in non-stationary oscillatory conditions. Moreover, the collapsed data from sample A are well fit by Rosenfeld's equilibrium excess entropy scaling law,

$$\tau_\alpha(t - t_d) \sim e^{-cS_2(t)/k_B}, \tag{3.5}$$

where $c = 3.9 \pm 0.2$ is a constant prefactor [187].

Previous studies of the excess entropy scaling connect sample dynamics to static structure; in other words, a measurement of static structure and the scaling law can be used to predict sample dynamics. Our finding, although similar in form, has a somewhat different implication: the static structure is a consequence, rather than the cause, of the relaxation process. Slower particle rearrangement processes (τ_α) produce more ordered particle arrangements (S_2) that require longer waiting times (t_d) to observe. Furthermore, since the time delay, t_d, is explicitly encoded in Eq. 3.5, we can use information about the "current" sample static structure to learn about plastic flow and relaxation processes that occurred in the sample at earlier times. The structures "remember" sample dynamical history [111]. In the future, application of this concept could provide insight about manufacturing and processing of amorphous materials wherein micro-structures are altered by thermomechanical processing [65, 212]. Note also, the "asynchronous" dynamics-structure connection observed in our oscillatory experiments is fully compatible with steady-state experiments. When $\dot{\Gamma}$ approaches a constant value, both $\tau_\alpha(t)$ and $t_d(t)$ lose their dependence on t, and the new scaling framework evolves into a previous relationship found for glass-formers in uniform shear flows [96]. Thus, we expect to see this transition from a non-steady-state to a quasi-steady-state by gradually increasing the oscillatory period in future studies.

To further examine the influence of material structure and other properties on the excess entropy scaling, we plot $\tau_\alpha(t - t_d)$ versus $S_2(t)$ for samples B and C (Fig. 3.4 inset). Sample B is a monodisperse colloidal suspension (see Table. 3.1) and thus has larger crystalline domains (see SI) compared to those in sample A. In this case, the combination of initial sample packing condition and shear-induced restructuring gives rise to much larger $|S_2|$ values, well above $4.5k_B$, a value that corresponds to the liquid-to-crystal transition observed in two-dimensional colloidal samples [226]. By comparison, sample C is a bidisperse mixture of much smaller particles (see Table. 3.1) and thus has more thermal particle motion; its $|S_2|$ values are between those of sample A and B. The short-time $F_s(\tau)$ for sample C is very close but never equal to unity, unlike those measured in sample A and B (see SI). We believe this difference is caused by thermal motion at short times in sample C. Despite these differences in material properties, in all three samples, both τ_α and $|S_2|$ decrease with increasing shear rate (as in sample A). All experimental data thus demonstrate that excess entropy scaling with relaxation time exists independent of shear rate. The best fits to Eq. 3.5 yield $c = 1.0 \pm 0.1$ and 1.4 ± 0.1, for samples B and C, respectively. In previous experiments with colloidal samples, the range of the dynamics is typically one decade by utilizing multiple packing fractions. Our experiment achieves a similar dynamic range by changing shear rate alone. The excess entropy scaling form has been found to depend on factors including interfacial boundary conditions and the functional shape of the sample's pair potentials [133, 96, 135]. For our amorphous samples with small crystalline domains separated by regions of disorder, to fully understand the difference in the prefactor c will require further investigation.

Finally, we also examine use of S_2^θ computed from directional $g(r,\theta)$; here, θ is the direction relative to shear. Unfortunately, the noise in $g(r,\theta)$ at long distances prevents Eq. 3.4 from converging within the finite cut-off distance (see SI). In steady-state measurements, this sampling noise can be suppressed by time averaging. In non-steady state samples, however, time-averaging necessarily involves integration over a broader range of shear rates which complicates evaluation of sample static structure. In the future, this issue could be ameliorated by using a much larger sample size. Our observation that τ_α scales with S_2 indicates a major difference in the microscopic relaxation mechanism between amorphous solids with small crystalline domains separated by regions of disorder and the more disordered glassy samples.

In the latter, τ_α has been found to scale better with the extensional excess entropy, S_2^θ, which is derived from $g(r, \theta = \pi/4)$ [119, 96]. The deformation along the extensional direction ($\theta = \pi/4$) has been argued to create more accessible configurations (that is, smaller $|S_2|$ values) that facilitate faster relaxation rates [96]. In sheared amorphous samples with small crystalline domains separated by regions of disorder, by contrast, particle rearrangements likely occur through cooperative sliding motions along grain boundaries, whose orientations depend on sample's initial condition and become randomized when sample size is much larger than grain size. Therefore, we expect particle rearrangements to be less sensitive to shear in our polycrystal-like solids [87, 204, 215].

3.3 Conclusion

In summary, we have developed a framework to understand plastic flow induced dynamics in deformed amorphous colloids with different degrees of polycrystallinity. The framework extends the concept of excess entropy scaling from equilibrium to nonequilibrium non-stationary states. Ours is the first experiment to demonstrate excess entropy scaling in *nonequilibrium* materials. Experimental data comprising a wide range of shear rates, relaxation times, particle pair correlations, and excess entropy reveal that transient shear-induced relaxation times scale as a simple exponential function of excess entropy. Collectively, these results demonstrate, in non-stationary states, that increasing (reducing) strain rates lead to faster (slower) relaxation, which in turn results in more disordered (ordered) micro-structures. The work also reveals a power-law connection between bulk shear rate and bulk viscous relaxation time that characterizes sample shear-thinning behavior; using the observation of excess entropy scaling, we thus deduce that shear-thinning is controlled by microscopic structure. Notably we find that new parameters, specifically lag times between shear rates, relaxation times and excess entropy, are crucial for proper application of the excess entropy concept in non-stationary conditions. In the future, it should be interesting to compare microscopic relaxation channels and shear-induced structural anisotropy in polycrystals versus more traditional glasses. Also, in addition to uniform and oscillatory shear, it would be desirable to test excess entropy scaling in more general strain protocols in both 2D and 3D systems.

3.4 Methods

3.4.1 Interfacial stress rheometer

The experiments use a custom-made interfacial stress rheometer [105, 182]. Briefly, a pair of vertical glass walls pin a water/decane interface as shown in Fig. 3.1a. A metal needle is located between and is parallel to the glass walls; it is held by capillary forces at the interface. Water height is adjusted so that the interface is flat between the two walls and needle. A pair of Helmholtz coils imposes a sinusoidal magnetic force on the needle that translates it axially. The out-of-plane Lorentz forces (approximately 10^{-16} N) are negligibly small compared with interfacial trapping forces (approximately 10^{-2} N). The moving needle and the two fixed boundaries thus create a flat two-dimensional (2D) shearing channel. A microscope (Infinity, K2) and high-resolution camera (IO Industries, Flare 4M180) are employed to measure the motions of the needle and interface-bound colloidal particles [105, 202].

3.4.2 Sample preparation

The colloidal suspensions are composed of sulfate latex particles (Invitrogen) with different diameters. The particles are injected onto the interface using a pipette, and regions of approximately 80x200 particles are studied. Due to the small particle sizes ($< 10\mu$m), capillary interactions are small and unimportant [172, 117]. A long-range dipole-dipole repulsion between particles [163] causes the spheres to assemble into a disordered, jammed, 2D structure with large amorphous areas filling the regions between randomly oriented microcrystal domains (see Fig. 3.1b-c and

SI). Characteristics of the three investigated particle systems such as particle type, packing fraction, mean interparticle separation, d (derived from sample pair correlation functions), and strain amplitude are summarized in Table. 3.1. The camera records the needle displacement and all particle motions; trajectories are extracted from the images using standard particle tracking software [2]. The experiments thus measure the particle positions, strain-rate, relaxation time, and excess entropy versus time during the shear cycle. We shear the samples at a fixed low frequency of 0.1 Hz to reduce/remove hydrodynamic effects. Additionally, we have calculated the Boussinesq number, $B_q = |\eta^*|/D\eta$, wherein η^* is the complex interfacial viscosity, D the needle diameter, and η the mean viscosity of the oil and water [35, 222]. B_q quantifies the ratio between the in-plane and out-of-plane stresses induced by the needle. We find that $B_q = 147.5$ and 101.5 for sample A and B, respectively, corroborating the expectation that hydrodynamic flows in the water and oil phases are negligible. The relaxation processes are due to plastic events that occur when the samples are stressed beyond yield.

3.4.3 Affine and nonaffine particle motions

To compute the y-dependent mean particle displacement, $\Delta x(y)$, along the shear (x) direction, we first compute $[y_j(t), \Delta x_j(t)]$ from all particles at time t; $\Delta x(y)$ is then obtained from the fit of $[y_j(t), \Delta x_j(t)]$ (see SI). The *local* strain is thus $\gamma(y,t) = \partial \Delta x(y,t)/\partial y$. To account for the slightly nonlinear flow profile (see Fig. S1 in SI), $\Delta x(y,t)$ and $\gamma(y,t)$ are fit by a polynomial of y up to the third and second order, respectively. To characterize the overall affine deformation, we define $\Gamma(t)$ as the spatial average (over y) of $\gamma(y,t)$. The nonaffine particle displacement, $\Delta \vec{r}'_j \equiv \{\Delta x'_j, \Delta y'_j\}$ between times t and $t+\tau$ is obtained by subtracting the affine contribution from the total horizontal displacement, $\Delta x'_j(\tau) = x_j(t+\tau) - x_j(t) - \Delta x(y_j, \tau)$. Since the net flow in y direction is zero, $\Delta y'_j(\tau) = y_j(t+\tau) - y_j(t)$.

3.4.4 Calculation of $\langle|\dot{\Gamma}|\rangle_{\delta t}$

To determine $\langle|\dot{\Gamma}|\rangle_{\delta t}$, we define a triangle kernel function centered at t, $\Lambda(t,s) \equiv \max(\delta t/2 - |s-t|, 0)$, and we compute the convolution of Γ and Λ: $\langle|\dot{\Gamma}|\rangle_{\delta t} = (|\dot{\Gamma}| * \Lambda)(t) \equiv \int_{-\infty}^{\infty} |\dot{\Gamma}(t-t')|\Lambda(t')dt'$. (Note, Λ is normalized before the convolution.) This parameter-free approach places maximal weight on the shear rate value at t, and zero weight on those shear rates outside of $[t-\delta t/2, t+\delta t/2]$. We also tested convolution with a Gaussian kernel function, and the results were very similar (see SI).

3.4.5 Evaluation of Δt and t_d

To determine Δt, we compute the (unnormalized) correlation function, $C_1(\Delta t) \equiv \langle(\langle|\dot{\Gamma}(t)|\rangle_{\delta t} - \langle\langle|\dot{\Gamma}(t)|\rangle_{\delta t}\rangle)(\tau_\alpha^{-1}(t+\Delta t) - \langle\tau_\alpha^{-1}(t+\Delta t)\rangle)\rangle$; here, Δt is the trial lag time and $\langle\cdots\rangle$ represents time average. The value of Δt wherein $C_1(\Delta t)$ reaches its maximal value is set to be the true lag time between $\langle|\dot{\Gamma}(t)|\rangle_{\delta t}$ and $\tau_\alpha^{-1}(t)$ (see SI). To determine t_d, we similarly compute the (unnormalized) correlation function, $C_2(h) \equiv \langle|S_2(t)|\tau_\alpha(t-h\tau_\alpha)\rangle$ as a function of h. Similar to the procedure above, $C_2(h)$ is maximized when $h\tau_\alpha$ (or equivalently, t_d) is closest to the true time lag between $|S_2(t)|$ and $\tau_\alpha(t)$ (see SI).

Chapter 4

The relation between system composition and its stress response throughout yield

4.1 Introduction

Disordered solids are ubiquitous. They are found, for example, in our foods as pastes and gels [153], and amidst our homes in the form of concrete [97] and mud [101, 155]. Frustratingly, these materials can experience sudden mechanical failure, such as the collapse of soil during rapid mudslides. Indeed, when sufficiently stressed, all disordered materials exhibit a swift decrease in ability to support load. In the vicinity of this "yield" transition, the solid material shifts from a state wherein energy is stored via internal elastic forces, to a state in which energy is dissipated via irreversible plastic rearrangements [122, 85, 42, 36, 171]. Microscopic spatiotemporal features are associated with this yield transition and affect macroscopic material responses such as ductile versus brittle behavior. In contrast to the case for crystalline materials, it remains a challenge to predict and control yield in disordered solids based on their constituents and interactions [85, 47]. To build such microstructural models, we need to identify key microscopic metrics [185] relevant to plasticity in disordered materials.

Recently, excess entropy has been explored for this purpose [77, 96, 27].

In equilibrium systems, the Rosenfeld scaling [62, 188, 61, 135] has shown that interparticle structure, measured by excess entropy, is connected to viscosity and particle mobility; Isomorph Theory provides a framework for this connection [61, 60, 79, 199]. There have also been great strides in using entropy-based methods to describe the glass transition within a thermodynamic context. One such example is Random First-Order Transition theory [229, 140, 59] (RFOT), which accounts for the system's entropy in excess of a crystalline state. In equilibrium, it is known that contributions to the sample excess entropy are largest from local structures with low configurational entropy and thus decreased particle mobility [124, 86]. Recently in far-from-equilibrium systems, excess entropy scaling has been shown to facilitate a relationship between microscopic structure and dynamics in simulations [96, 27] and in experiments [77], but no relationship to nonlinear rheology is provided. Thus, excess entropy offers an untapped signature for plasticity and a potential tool for modeling the mechanical response of disordered solids.

The study of rheology and particle dynamics in disordered systems has a venerable history [8]. As a result of this research, theories have proliferated [185] in recent decades. Two of the most successful are Mode Coupling Theory, wherein the interplay of dynamical modes causes the emergence of rearrangements [205, 72], and Shear Transformation Zone theory, which posits that local configurations determine where rearrangements occur [8, 67, 66, 207]. More recently, structural signatures for rearrangement have been revealed by machine learning approaches [50, 51, 15, 134], by study of low-frequency excitations [43, 232, 44, 201, 113, 230], and via local yield stress [167, 166] and near-neighbor cage dynamics [138]. Despite their usefulness, difficulties remain in applying these theories to experiments because of the need for fitting parameters [32, 205] and the use of empirical relations[138] that are difficult to measure. Moreover, while these theories account for history-dependence, an explicit phenomenological link between microstructure and history-dependent rheology has yet to be uncovered.

Generally, disordered materials contain memories, i.e., microscopic signatures related to how the material has been processed [109, 111, 149, 165, 69, 197, 150, 108]. Memory of a previous shearing direction, for example, can be encoded into a material's response. Once a material is sheared sufficiently in a given direction, continued shear requires more force than in the opposite direction because of a restoring force. In contrast, the Bauschinger effect is a memory at zero strain of previous plastic deformation; the yield stress is higher if sheared in the same direction as the original plastic deformation [73, 66, 111, 166]. Both types of directional memory are related to orientation of shear transformation zones [32, 67] and have been described by shear transformation zone theory [66]. In jammed systems, recent experiments and simulations have studied directional memories at low strain amplitudes, both below and near the yield transition; far above yield, memories are erased [110, 105, 217]. These observations, in turn, raise important new questions: How is microstructure related to directional memories? Is plastic flow synonymous with erasure? How do these phenomena manifest during yield, e.g., in storage and loss moduli?

In this contribution, we utilize excess entropy to quantify material memory and construct a microstructural model for disordered-material response and energy dissipation. Experiments and simulations show that three non-dimensional parameters govern the connections between microstructure and bulk rheology: packing density, a normalized (non-dimensional) form of the imposed stress, and an excess entropy (microstructure-related) ratio that quantifies the material's ability to retain information about its initial state. Our results confirm that memory is stored elastically and lost plastically, and show how yield and the ductile/brittle response emerge from knowledge about particle configurations at the microscopic scale.

4.2 Results

The experiments investigate disordered solids. The solids are colloidal monolayers of athermal, spherical particles (~ 40,000) adsorbed at an oil-water interface (Fig. 4.1a).

The charged particle surfaces generate a dipole-dipole repulsion between particles. This repulsion is strong enough to jam the entire material, arresting particle motions. To probe the effects of disorder, we study both mono-disperse and bi-disperse spherical particle systems with diameters of 5.6 μm and 4.1 μm-5.6 μm, respectively. In the bi-disperse system, crystalline domains tend to be much smaller (See Supplementary Materials). We impose many cycles of sinusoidal stress on these samples using a custom-made interfacial stress rheometer [105]that permits measurement of the bulk response of the colloidal monolayer while simultaneously recording trajectories of individual particles (see Methods). Cyclic stress is quasi-static, insofar as the time scale for a completion of a rearrangement (~0.5s) is much shorter than the shortest driving period (5s) or largest inverse strain rate (20s).

We investigate particle rearrangements by identifying non-affine deformations within each particle's neighborhood [66, 105]. The degree of non-affinity is quantified by the mean-squared displacement after subtracting the best fit affine transformation, D^2_{min} (see references [66, 105] for more information). Within cyclically sheared disordered materials, two types of non-affine events occur (Fig. 4.1a): those wherein particles return to their original position at the end of a strain cycle but along different paths, and those wherein particles escape their nearest neighbors and do not return [106, 132, 152, 181, 76]. It is possible to concurrently measure the degree of returning and escaping non-affine behavior for each particle [105]. For visualization, we estimate which type of non-affine event is dominant by defining $D^2_{min,C} \equiv \pm\sqrt{(D^2_{min,R})^2 + (D^2_{min,E})^2}$, where the subscripts refer to returning (R) and escaping (E) events. The sign for each particle is assigned according to which is greater. Negative corresponds to $D^2_{min,R}$, whereas positive corresponds to $D^2_{min,E}$. Both types of events dissipate energy [132, 152, 106, 181, 180, 76]. Returning non-affine events are known to emerge near the yield point when elasticity begins to diminish and plasticity starts to increase [105, 36]; escaping events arise well beyond yield [105] (Fig. 4.1b). The fraction of particles undergoing non-affine events is f_d. By following the rearrangements, we develop understanding about trajectory dynam-

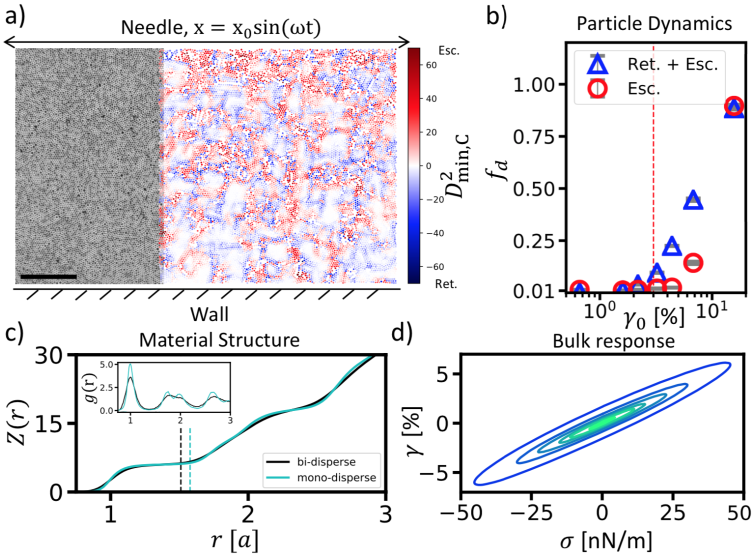

Figure 4.1: **Overview of structure, dynamics, and response.** We characterize the disordered solid bulk response to cyclic stress from evolving configurations of individual constituent particles. (a) Image of ~40,000 particles. Part of the raw image is shown (left). The scale bar is $200\mu m$. Detected particle positions are also shown (right). For illustration, color indicates $D^2_{min,C}$, which quantifies the degree to which a particle has followed a non-affine returning trajectory (blue), or a non-affine escaping trajectory (red). The particles in this image are experiencing yield (γ_0 ~ 15.7%). (b) Quantification of the fractions of particles escaping and returning averaged over all stress cycles versus total strain amplitude. Error bars are standard deviation. Returning events rapidly increase near the yield point (γ_0 ~ 3.0%). (c) The number of particles, $Z(r)$ within a radius, r of a reference particle. The radius is expressed in units of a, the average distance between neighboring particles. Vertical dashed lines indicate the limit of the first shell of neighboring particles. Inset: radial distribution function, $g(r)$. (d) The measured strain of the material versus the imposed stress throughout a cycle. Both stress and strain are averaged stroboscopically over 25 cycles. The different ellipses correspond to separate runs at different imposed stress amplitudes. Here, the area enclosed is a result of the lag between stress and strain, which in turn quantifies the energy dissipated from the material.

ics within the microstructure, and we take steps towards our ultimate goal to relate microstructure to rheology.

To quantify structure, we characterize the inter-particle forces and particle configurations using the radial distribution function, $g(r)$. Since the material is jammed, the motion of each particle is arrested by its neighbors [220, 126, 18, 127, 52, 88]. This caging, and escape thereof, provides another lens for the non-affine motions mentioned above; when enough particles pass each other via small changes in the structure of their surrounding cage, the material yields [66]. For quantitative analysis, we compute a microstructural measure of internal force, F^*, which is the sum of the magnitudes of inter-particle forces acting on the average particle. Specifically: $F^* = 2\pi\rho\int_0^{r_N}(-\frac{\partial u}{\partial r})g(r)rdr$; here ρ is the number density of particles, r_N is an upper cutoff distance below which nearest neighbor particles are found, u is the pair potential function between any two particles, $\frac{\partial u}{\partial r}$ is the force acting between any two particles, and $g(r)$ is the sample radial distribution function as a function of separation r (Fig. 4.1c; Methods). To determine r_N, we use the coordination number as a function of radial distance, $Z(r)$ (Fig. 4.1c). $Z(r)$ is derived from $g(r)$ and has been studied [220] and recently used [138] to characterize particle interactions and their effect on bulk materials. In our systems, neighbor shells are well defined by broad peaks in $g(r)$ separated by troughs (Fig. 4.1c-inset). The extent of the nearest neighbor shell is defined as the radius at which $Z(r)$ begins to increase rapidly for a second time (Fig. 4.1c-main).

We quantify disorder using excess entropy [188], the difference between the system's entropy and that of its ideal gas analogue (identical pressure, temperature, etc.). The two-body approximation of excess entropy, s_2, is calculated from $g(r)$ using a formula given in the methods section (Eq. 4.4). We calculate s_2 at discrete time points to characterize its variation within each shear cycle (more below). Since our systems are jammed, we interpret the below-yield system s_2 as 'frozen in' excess entropy [140, 229] .

We seek to relate these microstructural parameters to bulk rheological properties. Recall that as the yield transition is approached from below, the strain will begin to lag behind the oscillatory imposed stress by a phase angle, δ. If $\delta = 0[rad]$, then the material is fully elastic. If $\delta = \pi/2[rad]$, then the material is fully viscous. In between, the material exhibits both elasticity and plasticity; the phase angle lag quantifies dissipation (Fig. 4.1d) and encodes the ratio of the loss (plasticity) and storage (elasticity) moduli, $G''/G' = tan(\delta)$. We will show how G''/G' is related to the microstructural and dynamical quantities described above (s_2, F^*, f_d).

Next, we examine structural disorder, and its variation as a function of ap-

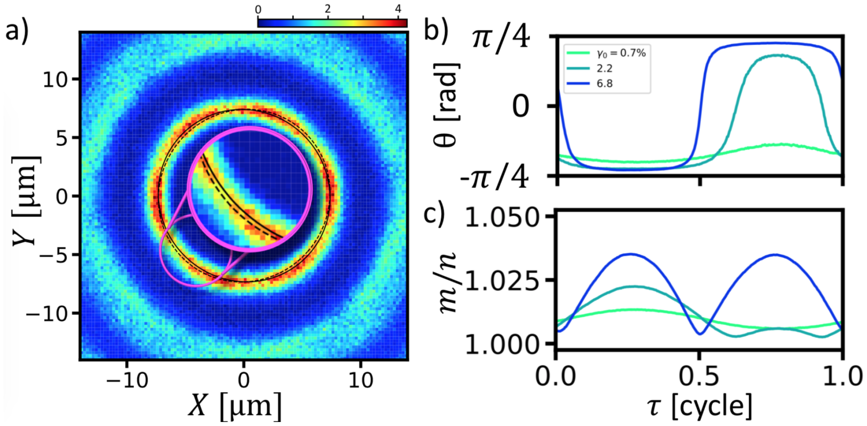

Figure 4.2: **Memory within microstructure.** Microstructural anisotropy reveals signatures of memory. Below yield, anisotropic orientation remains unchanged regardless of shear direction. Orientation quantifies stored memory. Above yield, anisotropic orientation reverses freely to match the direction of shear, indicating a loss of memory. (a) Radial distribution function, g(x,y,t) at a time corresponding to one quarter of the way through a shearing cycle. We fit an ellipse to the first neighbor ring. This ellipse stretches and reorients over time indicating changes in structural anisotropy of the sample. Two elliptic fits are shown at two times, t=1.25 (—) and 1.75 [cycles] (- - -). (b) Orientation of the sample microstructure over time as a function of strain amplitude. With increasing strain amplitude, the microstructure reorients to match the stretching axis. It first reorients completely at the yield point (3.2%). (c) Elongation quantified by the ratio of ellipse major and minor axis lengths (m/n) over time. Below yield, elongation oscillates directly with the strain; above yield, elongation oscillates with twice the frequency of strain perturbation. In b & c data are averaged strobscopically over 25 cycles.

plied shear. The angle-dependent radial distribution function, $g(x, y)$, quantifies microstructural order [122, 54] (Fig. 4.2a). Crucially, a nearest-neighbor ring is observable in disordered systems composed of interacting particles [221, 164]. In our experiments this ring deforms throughout shear (Fig. 4.2a and supplementary video), in agreement with previous observations [164, 45, 201, 57, 138, 54]. Throughout shear, the central ring is ellipsoidal. We can readily track the orientation and elongation of the ellipse throughout the shear cycle (Fig. 4.2b&c); ellipse orientation and elongation provide a measure of the sample anisotropy. Far above yield, as the material is sheared in one direction and then the other, the microstructural anisotropy switches between two principal strain axes (oriented at $\pi/4[rad]$ and $-\pi/4[rad]$, counter-clockwise from horizontal in Fig. 4.2a); in this situation, microstructural anisotropy is responsive to the direction of imposed shear (Fig. 4.2b). Below yield, however, the microstructural

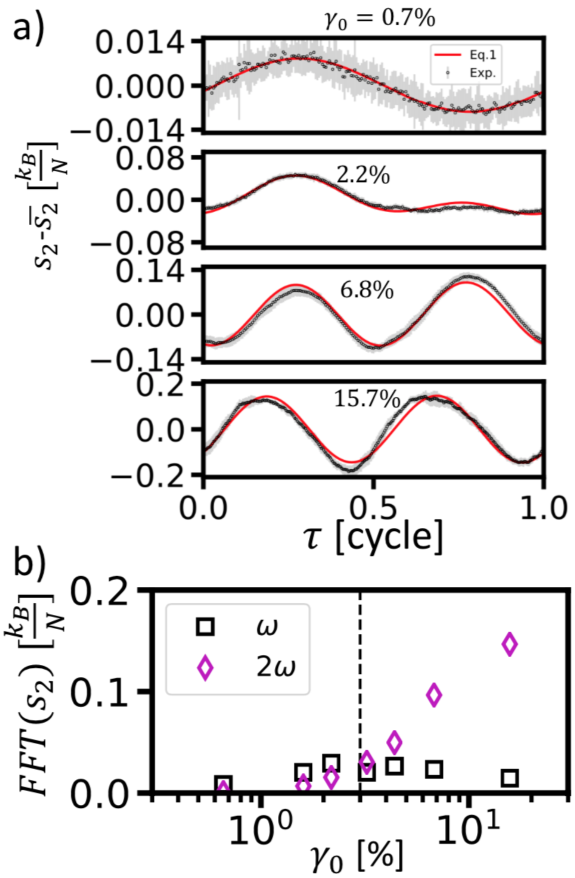

Figure 4.3: **Entropy and material memories.** Variation of entropy provides means for predicting system response to a given strain amplitude. (a) Excess entropy, with the mean value subtracted, follows a sinusoidal response. Below yield, its oscillation frequency is the shear cycle frequency. At yield, the excess entropy signal has components at both the driving frequency and twice the driving frequency: the material is beginning to forget its initial state. Above yield, the entropy response oscillates almost exclusively at twice the shear cycle frequency. Black dots indicate experimental data. Red lines are fits to equation 4.1 with T as the only fitting parameter. The experimental data are averaged stroboscopically over 25 cycles. (b) Amplitudes associated with the first and second harmonics are present within the s_2 signals. Note, that the second and first harmonic amplitudes cross each other at the yield point, γ_0 = 3%, designated by the vertical dashed line (- - -).

anisotropy remains in its original orientation; shearing is not sufficient to overcome initial 'frozen in' material structure. This phenomenon is apparent from changes in ring elongation (Fig. 4.2c) during the shear cycle. Note that above yield the microstructure elongates twice every shear cycle, at frequency 2ω, but below yield, the microstructure elongates only once per cycle at ω.

Microstructural anisotropy reveals a memory of the last direction the material was sheared above yield (Fig. 4.2). To remove internal stresses, each of our experiments is pre-sheared well above yield (γ_0 ~ 50%); nevertheless, this protocol imprints an anisotropy into the sample set by the last shear direction. Previously it was shown that this type of material memory is imprinted into $g(x, y)$ [164, 110, 168]. Here, we find that this memory imprint is associated with the principal directions of shear (Fig. 4.2). Once a memory is stored, the memory is retained as long as the material is sheared elastically. Precisely when the material yields, all memory is lost, and the microstructure freely switches between both orientations. Taken together, these results indicate that materials store and express memories in the elastic regime but lose them in the plastic regime. Furthermore, recently we showed that orientational memory is stored most strongly within crystalline domains wherein particle rearrangements are most intensely suppressed [217].

We now use excess entropy to characterize and relate observations about imprinted memory to the system microstructure. Above yield, we find that structural response is independent of the direction of shear (Fig. 4.3a, $\gamma_0 = 6.8\%$); when the material is sheared in either direction, the excess entropy increases and decreases as the shear is reversed. Ostensibly, the material cannot sustain a memory above yield, because it is continually forced out of meta-stable states within the energy landscape. Near yield, however, the direction of shear has an effect on structural response (Fig. 4.3a, $\gamma_0 = 2.2\%$). Notice, s_2 does not increase as the material is sheared over the second half of a sinusoidal shear cycle. Finally, below yield, the direction of shear is important; shear in one direction produces an increase in excess entropy, and shear in the other direction produces a decrease (Fig. 4.3a, $\gamma_0 = 0.7\%$).

As seen in figure 4.3b, the s_2 signals are sinusoidal. The first harmonic (ω) decays and the second harmonic (2ω) grows with increasing strain amplitude. The first harmonic is dominant below yield, and the second is dominant above yield. Therefore, the amplitude of the first harmonic of s_2 provides quantification of a stored memory, and the amplitude of the second harmonic characterizes the degree to which memory of the initial state is lost. Notice, these first and second harmonic amplitudes cross each other near the yield point.

To build a relationship between excess entropy and bulk rheology, we next investigate the connection of s_2 to the other dynamical metrics. For this comparison, we compute the ratio of the second to first harmonic amplitude, which we denote as H_{s_2}. We can relate H_{s_2} to several quantities in our system (Fig. 4.4). For example, H_{s_2} scales with the product of F_0/F^* and f_d (Fig. 4.4a), where F_0 is the amplitude of the prescribed shear force. This relationship between dimensionless parameters suggests

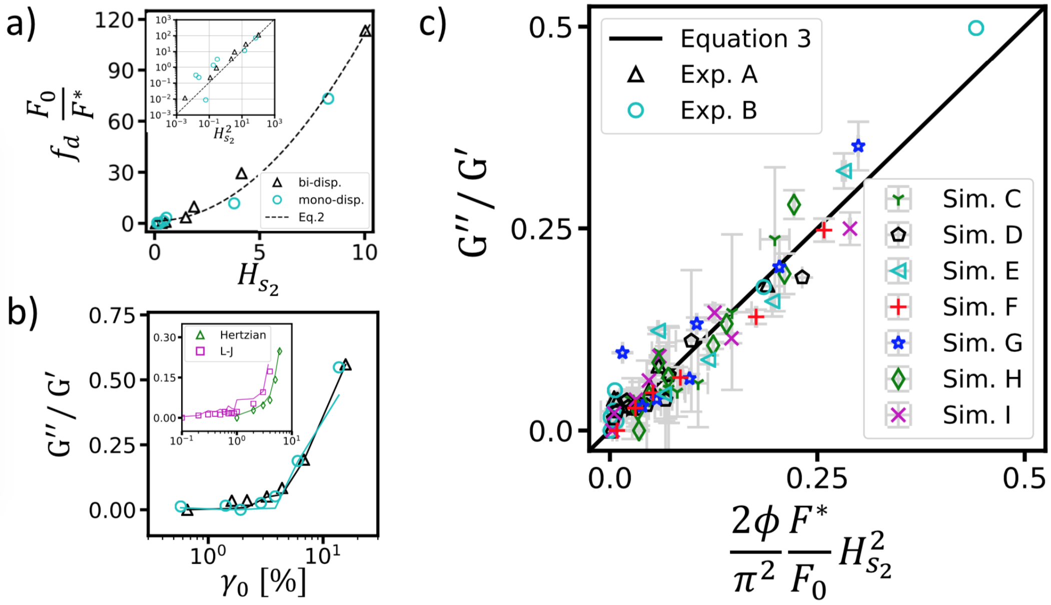

Figure 4.4: **Imposed force, microstructural excess entropy, and rheology**. a) The imposed force amplitude, F_0, normalized by the elastic force capacity, F^*, is plotted versus the excess entropy harmonic ratio, H_{s_2} (in both mono-disperse and bi-disperse experiments). A fit of the data suggests a parabolic relationship (p-value:3.14x10^{-13}, and r^2:0.989), corroborating equation 4.2. Inset: log-log. b) The increase in the ratio of loss and storage moduli, (G''/G') versus strain amplitude in both the mono-disperse and bi-disperse experiments (same legend for mono-disperse and bi-disperse experiments as panel a). Yield is signaled by the rapid increase in parameter values at about 0.03 strain amplitude. Inset: data from simulations employing Hertzian and Lennard-Jones interaction potentials. In both cases, markers are measured values and lines are predictions of equation 4.3. c) Left and right hand sides of equation 4.3. Notably, all parameters are measured. The solid diagonal line (—, slope of 1.0) represents equation 4.3. The slope of the best fit to the data is 0.981, p-value:4.43x10^{-26}, and r^2:0.944.

that when the imposed force on the system grows larger than F^*, the microstructure begins to permanently change, losing stored memory. Rapid variation of f_d also signifies the transition. These findings build on recent work that links excess entropy and non-affine particle dynamics [77, 96]. Note that the scaling in the present case is quadratic because f_d varies nearly linearly with the imposed force, F_0 (see Supplemental Materials). Finally, we find that the product of $H_{s_2}^2$ and F^*/F_0 scales linearly with G''/G' (Fig. 4.4c). The scaling factor for this linear relationship is $2\phi/\pi^2$; here $\phi = \pi N a^2/A$ quantifies the particle spatial density, a is the average nearest neighbor distance derived from the first peak of $g(r)$ (Fig. 4.1c: inset), and A is the total area of the observed sample or simulation.

The yield phenomenology shown in Fig. 4.4c depends on four dimensionless parameters: F_0/F^*, H_{s_2}, G''/G', and the packing density ϕ. The ratio F_0/F^* characterizes the shear stress exerted on the material relative to the internal stress that the material contains; when $F_0/F^* \geq 1$ plasticity is non-negligible. The microstructural quantity H_{s_2} provides a metric for whether a material's response is dominated (or not) by memory as it experiences oscillatory strain; this microstructural property can be interpreted as the degree of plastic response. Finally, a familiar ratio quantifies the bulk rheological response of the material: (G''/G'). All experimental (and simulation) data are collapsed using these dimensionless parameters, and a direct relationship between rheology, dynamics, and microstructure is experimentally established in the disordered solid.

Numerical simulations complement the experiments. The simulations enable us to vary features of the disordered system that are difficult to control experimentally. In particular, we can test ideas regarding variation of inter-particle potential. Moreover, unlike the experimental system, which involves a fluid-fluid interface that gives rise to viscous drag on the particles, the simulations offer the possibility to study the validity of our new concepts in disordered materials without viscous drag. Thus, we have conducted shear simulations without viscous drag and with two different inter-particle interaction potentials: Lennard-Jones, a model for atomic glass, and Hertzian, a model for granular systems (see Methods).

The simulations and experiments exhibit remarkably similar behaviors. Across both the experiments and simulations, a direct and common functional relationship between excess entropy and rheology is revealed (Fig. 4.4c). This relationship does not depend on the details of particle interactions, nor the amount of disorder. Further, since simulations do not involve a background fluid, the importance of hydrodynamic effects is ruled out. The findings above measure how strongly a material can retain a memory when it is sheared. We can probe the limits of our findings by progressively making it harder for the simulations to form memories. One way to explore this issue is to introduce varying amounts of Brownian motion into the Lennard-Jones simulations. At low temperatures, particles are fully arrested by interactions with their neighbors; all mobility is due to shear, and memory is formed reliably. However, if temperature is so high that the particles rearrange due to Brownian motion, in addition to shear stress, then memory is not formed reliably. Thus, high temperatures that increase thermal mobility produce larger error bars in Fig. 4.4c. Similarly, in our Hertzian simulation, if the packing fractions are low enough so that particles are not constrained by their neighbors, then memory is not formed reliably, and quantitative relationships are observed to become noisier. The wide applicability of these ideas suggests the existence of a deeper theoretical formulation. Thus, in the remainder of this paper we outline how our results may be derived phenomenologically (for the full derivation see the Supplemental Materials).

Inspired by the equilibrium successes of RFOT and related thermodynamic theories [229, 140, 59], we perform a simple energy balance to elucidate the relationship between s_2 and the material properties (G', G'') . We start with the harmonic behavior in s_2. In this situation, internal energy change is balanced via reversible heat transfer, $T\Delta S_2$, work, $F^*\Delta X/2$, and dissipation, $f_d F \Delta X$ (note the change in internal energy is zero):

$$T\Delta S_2(t) = F^*\Delta X(t)/2 + f_d F(t)\Delta X(t). \tag{4.1}$$

Here $\Delta X(t)$ is the displacement of the system boundary with respect to the equilibrium position $X(0) = 0$, $F(t)$ is the imposed shear force, and T is a parameter (generally different from the thermal temperature) that converts differences in entropy to differences in energy [20, 158, 27, 112]. Note, equation 4.1 represents the average response of a cage (i.e., a particle and its nearest neighbors) to the applied shear deformation. This equation would not apply in a system dominated by thermal motion, because we do not account for changes in entropy due to thermal fluctuations. The term $F^*\Delta X/2$ is the work done by the surroundings on the cage (on average); this term is connected to the potential energy between particles. With a single fitting parameter, T, the changes in harmonic behavior in excess entropy are reproduced from below to above yield (Fig. 4.3a).

The harmonic transition, associated with the excess entropy found in experiments and simulations, is captured by the first and second terms on the right-hand-side of equation 4.1. $H_{s_2}^2$ is the ratio of those two terms:

$$H_{s_2}^2 = f_d \frac{F_0}{F^*}. \tag{4.2}$$

This relation describes the harmonics data remarkably well (Fig. 4.4a). We next build on equation 4.2 by incorporating a finding of shear transformation zone theory, namely that elastic energy builds up in the microstructure until it is plastically released via non-affine rearrangement events [67, 66]. Quantitatively, this concept is represented as: $G'' \propto N f_d G'$, where N is the number of total particles observed; when substituted into Eq. 4.2 we obtain:

$$\frac{G''}{G'} = \frac{2\phi}{\pi^2} \frac{F^*}{F_0} H_{s_2}^2. \tag{4.3}$$

Note, that each parameter in this expression is measured and is generally accessible in many systems. Across strain amplitudes, remarkable agreement is found between G''/G' measured in experiments and simulations, and the predictions by Eq. 4.3 (see Fig. 4.4b&c).

4.3 Conclusion

Our results demonstrate that the yield transition of jammed systems has a configurational origin rooted in the persistence of material memory. We investigated the responses of several jammed systems undergoing cyclic shear deformation, incorporating aspects of STZ theory, excess entropy, and harmonic analysis into a single framework. The analysis reveals two new dimensionless parameters and three relations, derived phenomenologically, which connect particle configurations to bulk rheology. Importantly, the microstructural information needed, i.e., the radial distribution function, is available in myriad of scattering/microscopy experiments spanning length scales and particle types [122, 227]; thus, this analysis is accessible to experimentalists. In the future, it should be interesting to search for similar relations for other loading conditions, such as compression or steady shear, and to explore a wider array of particulate systems in which the particles are not simple spheres. More specifically, it may also be possible to relate local excess entropy to plastic events by exploring a local version of Eq. 4.1 and $F^*\Delta X/2$. Finally, it may be possible to generalize the work presented here to higher strain amplitudes by considering how energy is dissipated once, f_d reaches unity.

We have developed a framework to understand bulk properties of jammed materials under shear based on microstructural information. The findings hold potential to predict behavior of a broad range of dynamically arrested disordered materials including foams, gels, packings of nano- and micro-scale particles, and atomic/molecular glassy matter. Our findings, perhaps, also shed light on some deeper questions: in particular, the nature of entropy and the potential to use entropy ideas in far-from-equilibrium media. While entropy formulations for non-thermal systems have found utility in modeling disparate phenomena [203, 170, 99], its physical interpretation often remains mysterious. Disordered particulate packings appear to be particularly useful for clarifying this phenomenology, since their material structure can be interrogated with relatively simple methods.

4.4 Methods

4.4.1 Experiments

Using a custom built interfacial stress rheometer (ISR, SI Fig. 4.5), we simultaneously measure storage and loss moduli and track particle positions in 2D dense suspensions of athermal, repulsive particles. The ISR measures rheology by imposing force on a magnetic needle adsorbed at an interface between oil and water[202]. A stationary wall is opposite the needle, so that shear is imposed over a distance visible by a microscope. The displacement of the rod is measured precisely with the microscope.

ID	Type	Force type	Dispersity	Diameters	ϕ	$\Phi[\%]$
A	Experiments	Dipole-dipole	Bi-disperse	4.1, 5.6μm	14.02	~31
B	Experiments	Dipole-dipole	Mono-disperse	5.6μm	13.99	~35
C	Simulations	Lennard-Jones	Bi-disperse	N/A	5.03	N/A
D	Simulations	Lennard-Jones	Bi-disperse	N/A	5.00	N/A
E	Simulations	Hertzian	Bi-disperse	0.84, 1.16	9.62	100
F	Simulations	Hertzian	Bi-disperse	0.84, 1.16	9.68	110
G	Simulations	Hertzian	Bi-disperse	0.84, 1.16	10.12	120
H	Simulations	Hertzian	Bi-disperse	0.84, 1.16	10.73	160
I	Simulations w/ P.S.	Hertzian	Bi-disperse	0.84, 1.16	11.22	160

Table 4.1: A summary of the properties of the systems presented, including variety of inter-particle force, particle dispersity, particle sizes, spatial density of particles, ϕ, and simple area fractions of particles, Φ. We note, particles are point particles in simulations, C; hence, diameters are not defined in system C.

With displacement (strain) and imposed force (stress), the storage and loss moduli are calculated [35, 182]. Additionally, the microscope is used to image the particles (~ 40,000, from wall to needle) adsorbed at the interface. The particles include charges on their surfaces, so they exert dipole-dipole repulsive forces on each other [11, 142, 163]. At the particle densities in these experiments, these forces result in particle jamming, which we define as full kinematic restraint on each particle by its neighbors. In all data reported here the systems are in a sinusoidal, steady state. In the experiments, steady state occurs after five shear cycles. Twenty-five steady state cycles are used for calculations. For more information about these experiments and the calculations of D^2_{min} see Refs.[105, 106, 107].

An accessible quantity in our experiments is the two-body approximation of excess entropy, the difference between the system's entropy and the entropy of an ideal gas in an equivalent state ($s_2 \sim s_{sys.} - s_{I.G.}$). Conveniently, this quantity is calculated from the radial distribution function, which is available in a wide range of experiments [122]. The previously derived [16] formula for excess entropy is:

$$s_2 = -\pi\rho \int_0^\infty \big\{ g(r) ln[g(r)] - [g(r) - 1] \big\} r dr \tag{4.4}$$

where ρ is the particle number density. We implement equation 4.4 for each image in our experiments individually to collectively construct an entropy time signal, $s_2(t)$. For specifics of our excess entropy calculations, see Ref. [77].

The network force, F^* introduced in the paper is calculated based on inter-particle forces within the average neighborhood of particles. To make this measurement we estimate the average number of nearest neighbors around a particle as:

$$Z(R_c) = 2\pi\rho \int_0^{R_c} g(r) r dr \tag{4.5}$$

where R_c values are shown as the horizontal axis in Fig. 4.1c. We estimate experimental inter-particle forces based on potentials measured in experiments and molecular dynamics simulations reported in Ref. [163]. An account of our estimate is included in the Supplemental Materials.

4.4.2 Simulations

The data points for samples C were obtained using LAMMPS[174]. At each strain amplitude, 10 two-dimensional ensembles of 10,000 bi-disperse Lennard-Jones particles [228, 167] were subjected to sinusoidal shear under periodic boundary conditions at constant confining volume. The period of shearing was 100× that of the LJ time-scale of the particles. Prior to shearing, the samples were dynamically equilibrated at 1% of the glass-transition temperature[167]. During strain-controlled shearing LAMMPS' Nosé-Hoover thermostat was used to maintain the samples at approximately 1% of the glass-transition temperature. After 40 cycles of shearing, the shear stress was output for another 40 cycles for later use in the calculations of the dynamic moduli. We find that similar calculations at 9% of the glass-transition temperature begin to introduce noise to our final relation.

For simulation samples D and E, we use HOOMD-blue [78, 4] to impose cyclic strain on 10 particle configurations for each of six strain amplitudes $(1, 2, 3, 4, 5, 6\%)$ at constant confining volume. Ensembles are composed of jammed states of 50:50 bidisperse mixtures of 10,000 Hertzian particles. Ensembles are initialized from a randomly uniform probability distribution at a packing fraction below jamming, and subsequently quenched under FIRE minimization [24] whilst increasing the packing fraction until the desired pressure is reached. We then run a triangle wave shear protocol, imposing a small strain step of $10^{-4}\%$ and minimizing under FIRE after each step, until a total of 40 cycles have been completed. We calculate dynamic moduli based on the dominant frequencies of the resulting triangle waves.

4.5 Appendix

4.5.1 Discussion of systems

Here we make a few comments on the breadth of properties covered by our systems (as summarized in table 1. First, we note that the systems studied span a large range of disorder, ranging from crystalline regions of several hundred particles (Fig. 4.6a) to merely a few (Fig. 4.6d). Second we note that, Lennard-Jones potentials are attractive at long distances. So our results hold for systems where some of the particles experience attraction, as long as the system is jammed. Finally, our systems span a wide range of length scales. Lennard-Jones systems are atomic scale. Dipole-dipole systems are colloidal scale. Hertzian systems are granular scale. One further difference among our systems is that our experiments include an intermediary fluid and an interface, whereas our simulations do not. This serves to explore the role of specific energy dissipation (viscous drag in the experiments) versus unspecific dissipation (the simulations).

4.5.2 Scaling of imposed force and non-affine events

In the main text we identify that the entropic ratio H_{s_2} varies as a quadratic in figure 4.4a. Our model, (main body equation 4.2), makes no prediction about the form of the scaling unless we know how force amplitude, F_0, and the fraction of particles undergoing dissipative events, f_d, scale with each other. These values scale

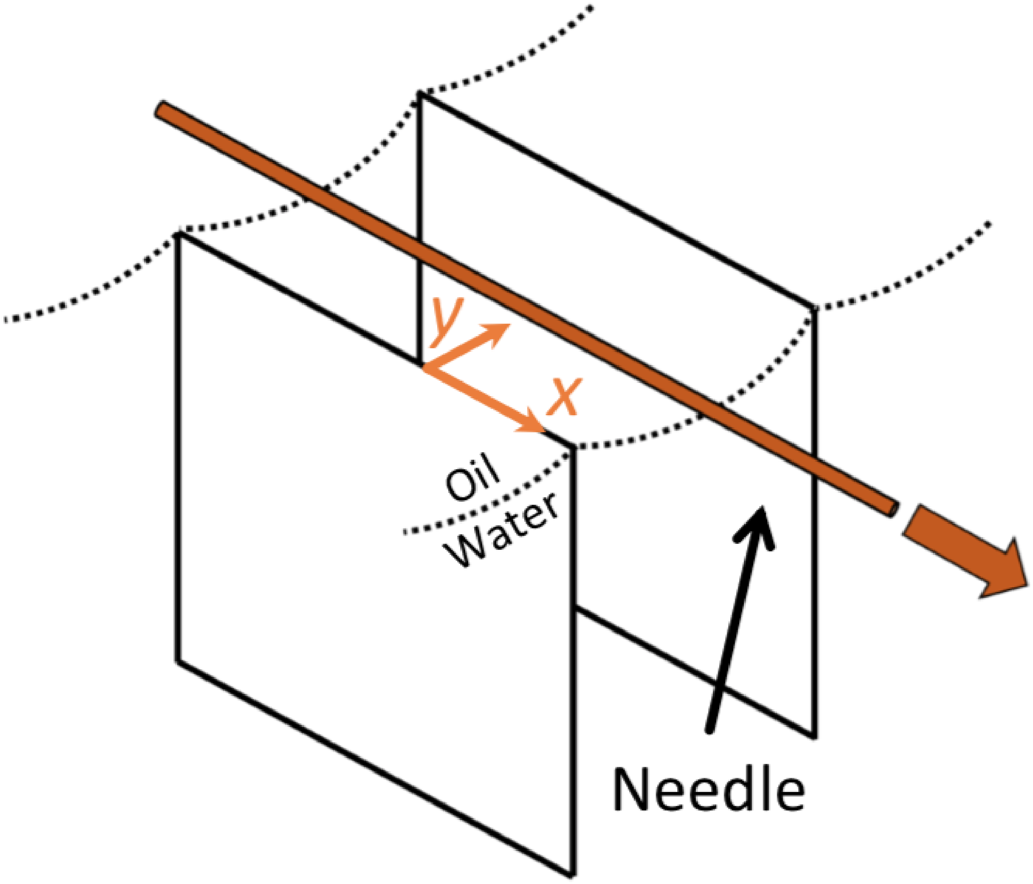

Figure 4.5: **Interfacial Stress Rheometer** Sketch of interfacial stress rheometer (ISR). Dense colloidal monolayer sits on water-oil interface that is bounded by two upright parallel glass walls. A thin magnetic needle cyclically shears the monolayer using Helmholtz coils. Accurate rheometry is obtained by tracking needle position as a function of forcing; particle tracking is used to characterize material microstructure.

linearly with each other in our experiments (Fig. 4.7), which results in a quadratic scaling. This is an approximation, as at very high strain amplitudes it is expected that the fraction of non-affine events will plateau at unity. But within the linear rheological regime studied here, this limit is not reached.

4.5.3 Experimental potentials

In this section we describe our method of estimating the mean inter-particle potential of our experimental systems A and B. Sulfate latex spheres of $D_l = 5.6\mu m$ and $D_s =$

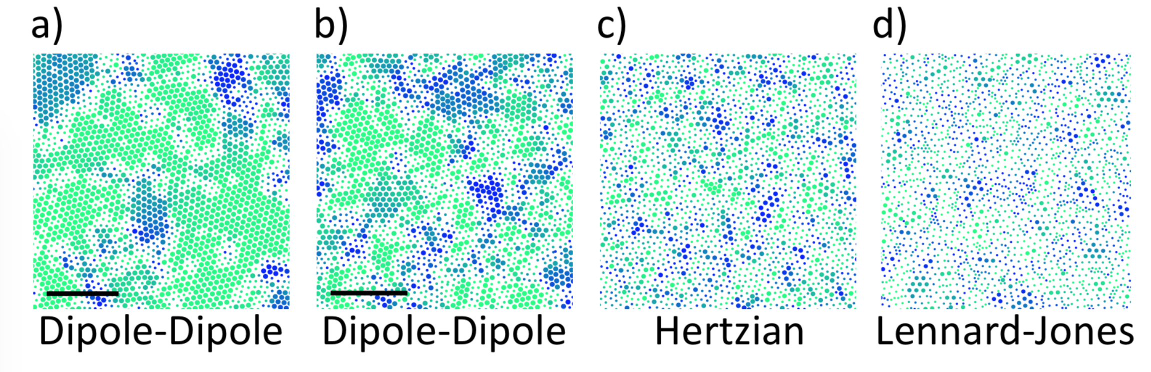

Figure 4.6: **Disorder increasing left to right** Crystalline regions visualized via sixfold bond orientation order, Ψ_6, measured from particle positions. Size of crystals decreases from left to right, indicating an increase in disorder. Colors help to indicate the lattice director (orientation) as a guide for the eye to help discern ordered and disordered domains. Dots with large size indicate $|\Psi_6| > 0.9$, and small dot size indicates $|\Psi_6| < 0.9$. (Scale bars: $100\mu m$). a) Mono-disperse, dipole-dipole, experimental system B. b) Bi-disperse, dipole-dipole, experimental system A. c) Bi-disperse, Hertzian, simulation system D. d) Bi-disperse, Lennard-Jones, simulation C.

$4.1\mu m$ are adsorbed at an interface of decane and water. The sulfate latex groups cover the surfaces of the particles, providing a charge. The charges and the presence of the interface cause the particles to experience dipole-dipole repulsion with each other. The dipole-dipole form is:

$$\frac{u(r)}{k_B T} = a_2 \frac{1}{r^3} \tag{4.6}$$

where u is the potential, k_B is Boltzmann's constant, T is the thermal temperature, a_2 is the scaling constant, and r is the center to center distance of the particles. In our bi-disperse system, the average separation between small particles is $r_{ss} = 7.53\mu m$. Separation between large particles is $r_{ll} = 8.74\mu m$.

This system is often used to study interfacial colloids; Park et al. [163] published a study that precisely measures the form of the interparticle potential quantitatively using Monte Carlo methods and optical tweezers. We used particles from the same manufacturer (Invitrogen Corporation, Carlsbad, CA) as Park et al. and followed the same particle cleaning procedure. They report that for particles of size $D_P = 3.1\mu m$, the mean value of $\langle a_{2,P} \rangle = 5.1 \pm 2.4 \times 10^{-13} m^3$, where P subscripts indicate Park et

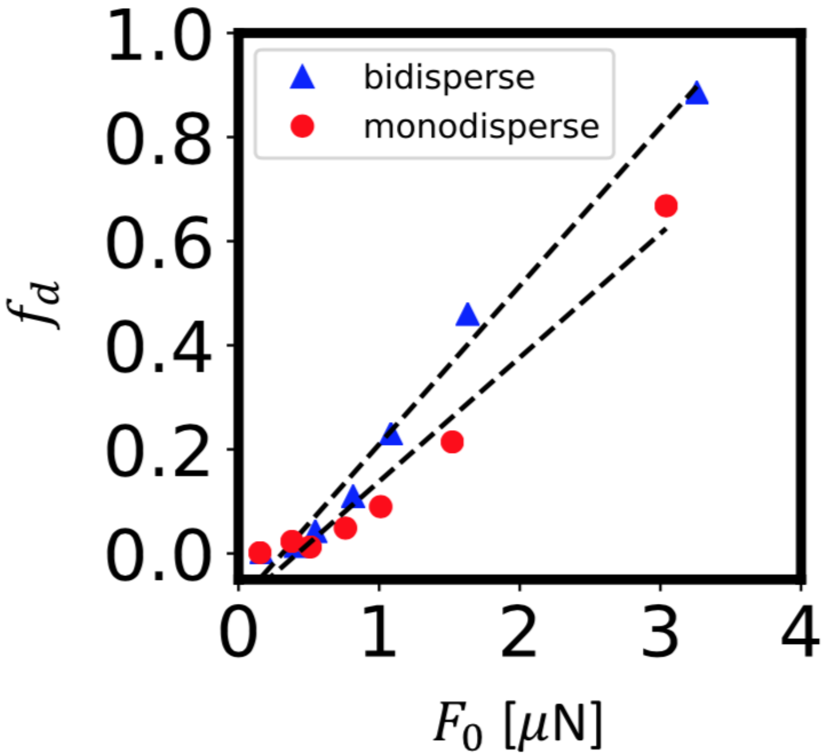

Figure 4.7: **Imposed force scales with dissipative events.** Within the linear rheology regime studied, the fraction of particles undergoing non-affine, disspative events scales linearly with the imposed force on the system. The dashed lines (- - -) are added to guide the eye.

al.'s values.

Within our bi-disperse system, the osmotic pressure is the same between large-large and small-small particles. Here the osmotic pressure is $-\frac{d^2u(r)}{dr^2}$. This allows us to write:

$$\frac{\langle a_{2,s} \rangle}{r_{ss}^5} = \frac{\langle a_{2,l} \rangle}{r_{ll}^5} = \frac{\langle a_{2,p} \rangle}{r_{pp}^5} \tag{4.7}$$

These equations are not linearly independent, so we extrapolate from our diameter-separation information ($[D_s, r_{ss}]$ and $[D_l, r_{ll}]$) to determine r_{pp} using D_P. We find $r_{pp} = 6.72\mu m$, $\langle a_{2,s} \rangle = 9.0 \times 10^{-13} m^3$, and $\langle a_{2,l} \rangle = 1.8 \times 10^{-12} m^3$.

For the main body of the text we use the average weighted by particle numbers of $\langle a_{2,s} \rangle$ and $\langle a_{2,l} \rangle$ for the entire suspension as $\langle a_2 \rangle$. Forces are calculated as $F_{el.}(r) = -\frac{du}{dr} = \frac{3\langle a_2 \rangle k_B T}{r^4}$.

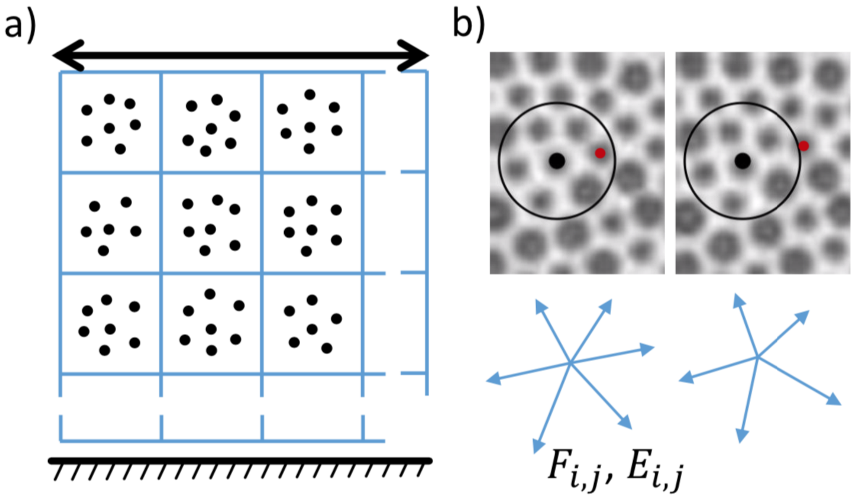

Figure 4.8: **Novel system and ensemble definitions.** A schematic of the central concepts used in the derivation: particle cages as microstates, chemical potential, and cage pressure. a) Each set of particles and their nearest neighbors, known as cages, are observable microstates of a system consistent with statistical mechanics of small systems [90]. In this way, ensembles are composed of copies of nearest neighbor cages, each subjected to the same shear state. b) A demonstration of the concept of chemical potential within this cage-microstate definition. The energy stored in a cage *via* particle interactions changes as a particle is squeezed in or out of a cage. See the accompanying Supplementary Video. c) The total energy, e_i, within cage i can be measured systematically as the total energy stored by the central particle, i, with its neighbor particles, j. Similarly the cage pressure can be calculated as the total force stored between a central particle, i, and its neighbors, j.

4.5.4 Phenomenological derivation

In the first subsection we expand this equation to include the particulars of oscillatory shear. The second section lays out the details for quantifying bulk mechanical properties, such as yield.

Statistical mechanics derivation

Equation 4.1 appears similar to the fundamental thermodynamic relation (graphically in figure 4.3a):

$$T\Delta S_2(t) = F^*\Delta X(t)/2 + f_d F(t)\Delta X(t) \tag{4.8}$$

where t is time, T is a scaling parameter (generally different from the thermal temperature) that converts differences in entropy to differences in energy, S_2 is the excess entropy, F^* is the sum of the magnitudes of inter-particle forces acting on the average particle, X is the system boundary position, f_D is the fraction of particles in the system that are actively dissipating energy, and F is the imposed force at the system boundary. Here Δ indicates a difference between the starting state and the state at time t.

We consider a microstate to be a single particle and its nearest neighbors, called a cage. Ensembles are taken across all of the cages within a material (Fig. 4.8a). For large systems with thousands of particles, this may solve the problem of accessibility mentioned earlier; an a-thermal system may explore all possible microstates slowly in time, but in space there are many realizations. Notice also that in this definition of microstates, energy and particles are free to transfer in and out of the system.

Using nearest neighbor cages as microstates also potentially solves the energy dissipation challenge. In many a-thermal materials, dissipation is achieved by particles shifting in irregular, or irreversible ways; while undergoing high deformations, some particles rearrange entirely (Fig. 4.8b). Rearrangements result in a change in the number of particles, dn, within the cage and a change in energy within the system. Chemical potential, μ, the ratio of energy change to the change in the number of particles, is a concept that naively fits with this phenomena. Hence, it appears that by defining microstates as cages of nearest neighbor particles, some of the challenges of applying statistical mechanics to a-thermal systems are alleviated.

Equivalents of the other macroscopic thermodynamic variables are also required to describe a-thermal materials using energy conservation. We define cage energy to be the total energy stored between the central particle and its neighbors: $e_i = \Sigma_j e_{i,j}$ for cage i, and particle j. Entropy is also defined as the entropy of a cage; for a-thermal materials excess entropy, s_2 has recently been shown to be a useful entropic measure of a cage's response to deformation [201, 27, 112, 77]. The conjugate pair, pressure and volume are also required. Empirically, based on the work above, the analogue to pressure is the total force acting on the central particle within a cage, $F_i = \Sigma_j F_{i,j}$. The equivalent of volume is the strain state of the cage, x. With these variables in hand it is now possible to describe a cage and move forward with ensembles specific to the situation; i.e. nxe, nxT, μxT ect.

The choice of ensemble depends on the type of deformation that the system undergoes; compression and shear will each require a different ensemble. Equation 4.8 applies to shear of colloidal systems. In a separate paper which is in preparation, we explore the same phenomena within a compressed granular material. In this paper we will focus on the sheared system, but a similar methodology can be shown to work for the compression system as well.

In determining the correct ensemble we must identify the member of each conjugate pair that is free to fluctuate; conversely, we must also determine which is held constant. In systems that have particle rearrangement, the particles are free to shift in and out of a cage, so n varies and μ is constant. In sheared systems, each cage is a part of the greater system, so strain is the same for each cage. However, strain changes from one instant to the next, so x varies in time. Pressure does not change in sheared systems, so F_i varies between cages, but the average is constant in time. A way to see this on the microscale is by considering that during shear there is no volumetric dilation [81], which means particles do not get closer or further from each other during shear. Hence the total force inside a cage, F_i, which is related to particle separations, cannot change with shear. Entropy varies with shear because it is a function of not only the mean separation of particles, but also their distributions. So entropy varies and temperature is constant. Therefore, a sheared system's state *at any given instant in time* can be described by the grand canonical ensemble, μxT.

Each successive instant in time corresponds to a new shear state. Because there are many simultaneously observed cages, an ensemble average is accessible in each instant. With this framework in place, it is possible to employ statistical mechanics [146] (conservation, combinatorics, and the method of undetermined multipliers) to determine the partition function:

$$\Xi(\mu, x, T) = \sum_n \sum_i e^{-e_{n,i}(x)/k_B T} e^{\mu n/k_B T} \tag{4.9}$$

and the probability of finding a cage with specified particle number n and energy level e:

$$P_i(n; \mu, x, T) = \frac{e^{-e_i(n,x)/k_B T} e^{\mu n/k_B T}}{\Xi(\mu, x, T)} \tag{4.10}$$

where k_B is Boltzmann's constant.

Next recall that the average energy across all cages will be the sum over probability of a state multiplied the energy level of that state:

$$\bar{e} = \sum_{n,i} P_i(n) e_{n,i} \tag{4.11}$$

Taking a differential of $\bar{e}$ reveals a statement of the first law of thermodynamics, applicable to the ensemble of cages:

$$d\bar{e} = \sum_{n,i} e_{n,i} dP_i(n) + \sum_{n,i} P_i(n) de_{n,i} \tag{4.12}$$

where the first term represents heat transfer and the second term represents work. It has been shown [146] that $\sum_{n,i} e_{n,i} dP_i(n) = Tds$ and $\sum_{n,i} P_i(n) de_{n,i} = -\bar{F}dx + \mu d\bar{n}$, which results in:

$$d\bar{e} = Tds - \bar{F}dx + \mu d\bar{n} \tag{4.13}$$

which is a version of the first law applicable to individual particle cages.

Similar to the statistical mechanics of small systems [90], it is next possible to regain system wide information by summing over the N observed cages:

$$\sum d\bar{e} = \langle d\bar{e} \rangle N = dE \tag{4.14}$$

$$\sum T d\bar{s} = T \langle d\bar{s} \rangle N = TdS \tag{4.15}$$

$$\sum \bar{F}dx = \langle \bar{F} \rangle dxN = F^{*}dX/2 \tag{4.16}$$

$$\sum_{j} \sum \mu_j d\bar{n} = \sum_{j} \mu_j \sum d\bar{n} = AdN_e \tag{4.17}$$

where we note that equation 4.16 holds as long as $\bar{F}$ and dx are de-correlated. In the shear case, dx varies linearly and $\bar{F}$ fluctuate randomly as expected from a pressure like term, so this is a valid assumption. Additionally, equation 4.17 accounts for chemical potentials, μ_j, being different depending on the particle species involved (poly-dispersity, charge distribution, ect.) We utilize the chemical affinity, A, and the total number of particles that escape, dN_e to further simplify, which is common in chemical physics [116].

Summing over equation 4.13 and combining with equations 4.14 through 4.17 results in a system wide statement of the first law:

$$dE = TdS - F^{*}dX/2 + AdN_e \tag{4.18}$$

Comparing equation 4.18 to equation 4.8 it is seen that in the sheared a-thermal system, $dE = 0$, so E is constant. This is true for the same reason that F^{*} is constant: on average across the system, particles do not get closer or further apart during shear because there is no volumetric dilation [81]. Hence no additional energy is stored by the inter-particle potentials. It is also seen that $A = -FX/N$; this observation fits with the understanding that the chemical potential (or affinity) is the Gibbs free energy per particle of the material [116]. The Gibbs free energy in this case is the maximum reversible work that *could* possibly be done by a system, which in this case is the driving force, F, multiplied by the system displacement, X. With that we conclude the derivation of equation 4.8, shown in figure 4.2.

We would like to point out the special case of the particles that trace limit cycles, but still return to their original positions, without escaping. In the statistical mechanics context outline here, we interpret these as particles that do not quite escape; however, they dissipate energy irreversibly due to the limit cycle behavior. We can include those in the AdN_e term by considering they are functionally similar: they too have an energy, in this case dissipated, per particle and a number of particles that are active. This allows us to replace AdN_e with AdN_D where dN_D is the change in number of particles emanating energy from the system, either by particles escaping or by dissipation.

Specifics of oscillatory shear

The idea of applying the thermodynamic definition of temperature to describe sheared athermal systems has been explored in previous research [158, 198, 27]. Specifically we use[27]: $T = \frac{\partial E}{\partial S_2}$, where E is the energy of an average cage. Briefly, as discussed in the main text, equation 4.1 quantifies energy flows through the system (i.e., the average cage); $T\Delta S$ is reversible heat transfer, $F^*\Delta X/2$ is work done on the system (on the average cage), and $f_d F \Delta x$ is dissipated energy due to non-affine deformation. The net change in the internal energy of the cage is zero for shear deformations. Our experiments and simulations indicate that:

$$T\Delta S = F^*\Delta X/2 + f_d F \Delta X. \tag{4.19}$$

Here T is a temperature-like fit constant. S is the entropy of the average cage. F^* is a property of the material that quantifies the average force experienced by a typical particle due to its neighbors. It is calculated as: $F^* = \rho \int\int (-\partial u/\partial r) g(x,y) dx dy$, where ρ is the number density of particles, u is the inter-particle potential, and $g(x,y)$ is the radial distribution function. Here f_d is the fraction of particles undergoing dissipative events, which we detect via non-affine rearrangements. Non-affine events are detected via D^2_{min}. See Refs [105, 106, 107] for details on this calculation. Specifically, $f_d = N_d/N$, where N_d is the number of particles experiencing non-affine events and N is the number of total particles observed. The prescribed shear force and resultant displacement of the shearing surface are F and X respectively. We define the Δ operation as the difference between entropy at time t and the average entropy over an entire cycle of shear: $\Delta S = S(t) - \overline{S(t)}$. Similarly for X.

We next summarize the specifics of our systems: most notably oscillatory shear and excess entropy. To apply equation 4.19 to the oscillatory shear cases considered in this paper, substitute in the time signals for shear surface displacement ($X(t) = X_0 sin(\omega t + \delta)$) and force ($F(t) = F_0 sin(\omega t)$) on the right-hand-side. On the left-hand-side, multiply by Nk_B/Nk_B:

$$Nk_B T\Delta(\frac{S}{Nk_B}) = \frac{F^* X_0}{2} sin(\omega t + \delta) + \frac{N_d}{N} F_0 sin(\omega t) X_0 sin(\omega t + \delta) \tag{4.20}$$

where ω is the frequency of the imposed force and δ is the resulting time lag between the imposed force and the resulting displacement. δ is an important physical parameter in rheology; it helps us to distinguish between solids, fluids, and everything in between. A fully elastic material has a $\delta = 0[rad]$; stress and strain are in phase as is seen from Hooke's law. A fully viscous material has a $\delta = \pi/2[rad]$; stress and strain are fully out of phase as is seen from Newton's law of viscosity [122].

In our experiments, changes in pressure are negligible. Hence, changes in absolute entropy are approximately the same as those for excess entropy ($ds_2 \sim ds - ds_{I.G.} \sim ds_{total}$); the ideal gas entropy is not expected to change. Notice, entropy has changed to lower case 's' to represent quantities that are normalized by N and in units of k_B, which is convention. Additionally, we implement the product-to-sum trigonometric identity ($sin(u)sin(v) = (1/2)[cos(u - v) - cos(u + v)]$). Reorganizing gives:

$$\Delta s_2 = \frac{F^* X_0}{2Nk_B T} sin(\omega t + \delta) + \frac{N_d F_0 X_0}{2N^2 k_B T}\{cos(\delta) - cos(2\omega t + \delta)\}. \tag{4.21}$$

Equation 4.21 describes the evolution of a cage within our jammed system as it undergoes oscillatory shear. Notice that equation 4.21 is unitless. It is now apparent that the second term on the right-hand side (with N_d) has the second harmonic of the forcing frequency 2ω; this relation reproduces the frequency shift of the entropy signals in our simulations and experiments (main body Fig. 4.3a). The appearance of the second harmonic in the entropy signal captures the transition to plasticity.

Connection to rheology

We investigate the yield transition further by taking the ratio of the first and second harmonics within frequency domain of s_2, ($H_{s_2}^2 \equiv \frac{FFT_{s_2}(2\omega)}{FFT_{s_2}(\omega)}$), which follows from equation 4.1 as:

$$H_{s_2}^2 = \frac{N_d}{N}\frac{F_0}{F^*}. \tag{4.22}$$

Equation 4.22 is visualized in figure 4.4a of the main text. This scaling is quadratic because N_d and F_0 scale linearly with each other (Fig. 4.7). The square of H_{s_2} in equation 4.22, is included so that linear relationships are retained throughout.

From here we revisit an idea posited by Falk and Langer (Ref.[66]): relaxation events are due to a local buildups of elastic energy that suddenly release (i.e. $G'' \propto N_d G'$). Recently quantified for above yield cases in Ref.[106] and here expanded to below yield, $G'' = \frac{2a^2}{\pi A} N_d G'$, where a is the first peak distance of g(r) and A is the area of observation. Substituting this equation into equation 4.22 for N_d gives:

$$\frac{G''}{G'} = \frac{2Na^2}{\pi A}\frac{F^*}{F_0}H_{s_2}^2 = \frac{2\phi}{\pi^2}\frac{F^*}{F_0}H_{s_2}^2 \tag{4.23}$$

which allows us to relate the bulk material response directly to measurable microstructural properties without the use of fitting parameters. Equation 4.23 is visualized in Fig. 4.4b&c. ϕ quantifies particle density as $\phi = \pi N a^2/A$, which implicitly takes a as an effective particle diameter. This relation reveals that the yielding transition of jammed materials is specified by four dimensionless groups based on imposed force, particle density, a memory based dimensionless entropy, and the bulk response.

Additional thermodynamic relationships

With equation 4.1 derived using a statistical mechanics framework, it is possible to test other statistical definitions as well. Within the entropy representation, the definitions of intensive variables can be investigated as long as other parameters are held constant according to the definitions. Two of the definitions are: temperature, $1/T = \partial S/\partial E)_{X,N_D}$ and chemical affinity, $A/T = \partial S_2/\partial N_D)_{X,E}$, where the subscripts must be held constant. Recall that here A is the chemical affinity. Because E is constant within a sheared system, the definition of T is inaccessible. Similarly, the definition of A is inaccessible because X varies in time for all experiments. However, the third definition, cage pressure, F^*, is measurable in sheared experiments:

$$\frac{F^*}{T} = \left.\frac{\partial S_2}{\partial X}\right)_{N_D,E} \tag{4.24}$$

The data appears to follow equation 4.24, which provides further support of the statistical model (Fig. 4.9a).

The Maxwell relation for the double derivative of energy, E, with respect to entropy, S_2, and number of rearranging particles, N_D, can also be investigated:

$$\left.\frac{\partial A}{\partial S_2}\right)_{X,N_D} = \left.\frac{\partial T}{\partial N_D}\right)_{X,S_2} \tag{4.25}$$

The data appears to follow equation 4.25, which provides further support of the

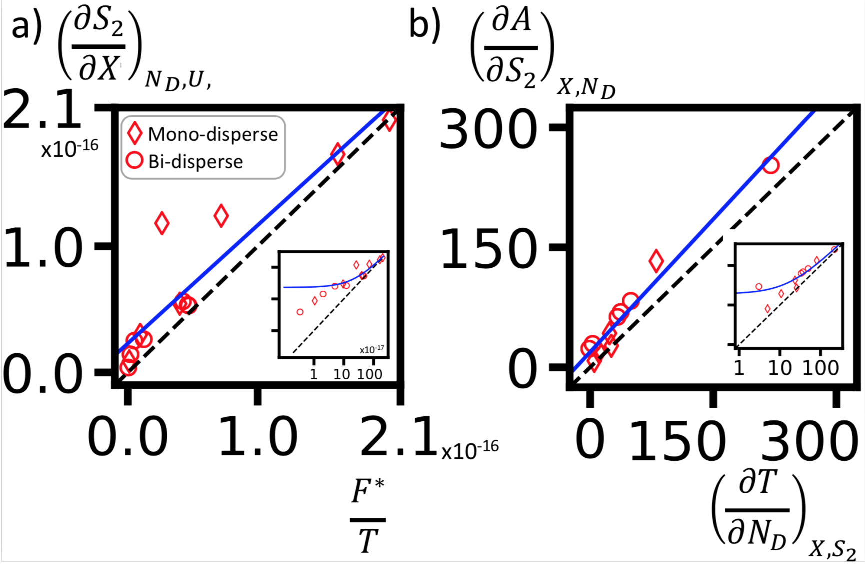

Figure 4.9: **Additional thermodynamic relations.** Demonstration of available thermodynamic definitions and Maxwell relations. a) Definition of cage pressure, F^*. b) The Maxwell relation for the double derivative of energy, E, with respect to entropy, S_2, and number of rearranging particles, N_D. Dashed lines (- - -) are equation 4.24. Solid lines (—) are fits for demonstration.

statistical model (Fig. 4.9b).

The above relations (Eqn. 4.24-4.25) follow from the statistical mechanics framework given in sec. 4.5.4. Here we also present the beginnings of an empiric equation of state between temperature, T, and mobility as measured by f_d. We find

$$T \propto f_d \tag{4.26}$$

over several orders of magnitude T and f_d are proportional (Fig. 4.10). This implies a kinetic relationship between temperature, T, and the propensity for particles to leave their cages, measured by f_d, which provides further support of applying thermodynamics and statistical mechanics to disordered materials.

The thermo-statistical basis of memory

The final thermo-statistical connection provided by this thesis is between memory, equilibrium, and shear. Landauer's principle quantifies the minimum amount of en-

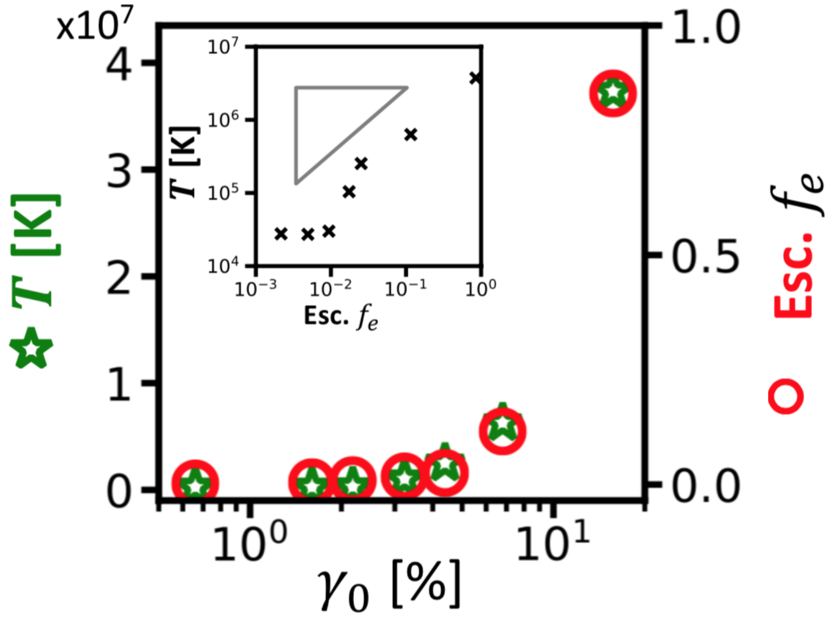

Figure 4.10: **Hints of kinetics.** Demonstration of an empiric, equation of state-like proportionality, which captures the kinetic relationship between temperature, T, and the fraction of particles that leave a cage, f_d.

ergy required to erase a single bit of information based on the temperature of the heat bath that the system resides within. Starting from Boltzmann's entropy formula:

$$S_{memory} = k_B ln(W), \tag{4.27}$$

where W is the number of possible states. A bit represents two possible states, so $W = 2$. In addition, taking $S_{memory} = E_{erasure}/T$ gives the Landauer equation:

$$E_{erasure} = k_b T ln(2). \tag{4.28}$$

In the context of sheared amorphous materials, each cage lies within a bath of many surrounding cages. Above we described how a caged material stores a single bit of information within the orientation of its microstructure ($W = 2$ in orientation memory as well). We also explored how cages exists within a bath of its neighbor cages and the system resides at a single configurational temperature, T. Using equation 4.28 it is possible to calculate the minimum energy required to erase the orientation memory relative to the energy within the system. given that the memory

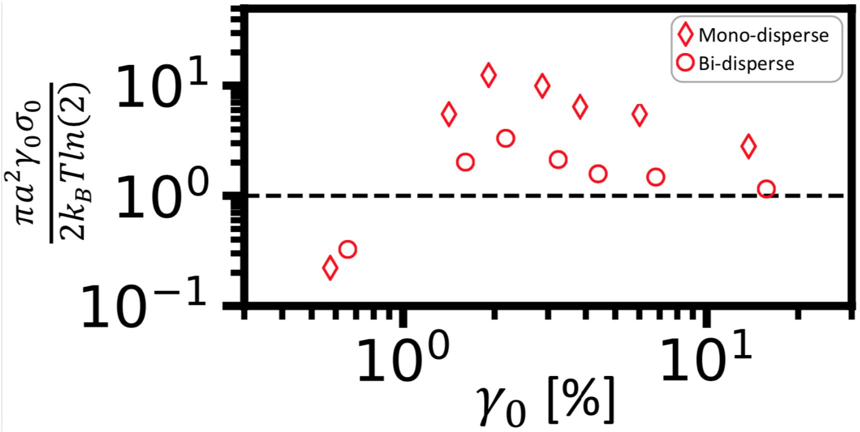

Figure 4.11: **Memory erasure measured by thermodynamical information.** Using Landauer's principle is is possible to calculate the minimum energy required to erase a stored memory. In this plot we compare the minimum energy of erasure to the cage strain energy, $E_{strain}/S_{erasure}$, relative to the strain amplitude that the system undergoes. A peak above one near the yield point quantifies memory erasure and mirrors how close to equilibrium the system is in the cage ensemble approach.

is expressed throughout the entire system via average cage, we measure the energy injected across the entire system. Rheologically, the energy injected is the strain energy: $E_{strain} = 0.5\pi a^2 \gamma_0 \tau_0$. Here a is the nearest neighbor distance of $g(r)$, γ_0 is the strain amplitude, and τ_0 is the shear stress amplitude.

Figure 4.11 shows the trends of the energy injected relative to the energy required to erase a memory as a function of strain amplitude. For both experimental systems, the energy injected at the lowest strain amplitude is below the minimum required for erasure. Around yield ($\gamma_0 = 1.5 - 3.5\%$) the energy ratio spikes above one, which is exactly when they are being erased. This is also the regime in which limit cycle trajectories emerge, indicating non-reversible energy dissipation. Finally the energy ratio falls back towards one above $\gamma_0 > 2.0$, indicating that memories are still being forgotten, but very efficiently. This is the regime in which limit cycles disappear and particle begin to escape their cages according to the chemical term in equation 4.18. This reinforces the picture that the system transitions from an elastic equilibrium, dominated by cage pressure, F^*, to a plastic equilibrium, dominated by chemical changes, f_d. Between these two equilibrium regimes is an out of equilibrium transition. Memory, measured by $E_{strain}/E_{erasure}$, reflects this transition and the degree of equilibrium.

Chapter 5

Summary & Perspectives

5.1 Summary

Understanding how amorphous solids yield is of fundamental importance in tuning the mechanical response of a myriad of materials that are already in use and in creating new ones. From concrete in our foundations to the silicate glass in our windows, amorphous solids have a huge significance. However, yield of amorphous solids is often accompanied by rapid failure, so they currently cannot be used in high-risk applications, such as support structures. Understanding ways to tune yield based on the microstructure would allow engineers to use amorphous solids in more applications. Perhaps even more importantly, the production of amorphous solids requires much less energy than their crystalline metallic counterparts, such as steel. Moreover, their production does not intrinsically require carbon as an input as steel does [208]. Therefore, a greener future may be possible if amorphous solids can replace some crystalline steel.

In this thesis I have investigated the microstructural mechanisms that accompany yield of amorphous solids. Three fundamental questions were probed: how are the dynamics of particles linked to the bulk mechanical response, how are the dynamics of particles linked to the particle configurations, and how is the bulk mechanical response tied to the particle configurations? These questions are examined using data collected by a custom interfacial stress rheometer that allows for both the simultaneous imaging and measurement of particle positions.

In Chapter 2, I investigate dynamical signatures of constituent particles in semi-amorphous 2D colloidal packings of a-thermal particles. I find that at low oscillatory strain amplitudes the trajectories are erratic. With increasing strain amplitudes, particles trace out areas though out a cycle; they move in the shear direction and then return along a different path. These limit cycles indicate energy dissipation. I show that for particles that return to their original positions at the end of a shear cycle, the area enclosed is a key metric that reflects the total energy dissipated. Moreover, the arc-length of each trajectory is limited to the length predicted by the strain field – even during chaotic motions. A dimensionless equation is uncovered that relates the strain amplitude with the average enclosed area divided by the average normalized arc-length. These enclosed areas represent signatures of plastic energy dissipation during yield. This chapter reveals that the statistics of chaotic the dynamics relates to the mechanical response.

Chapter 3 explores experimentally the relationship between particle mobility and excess entropy. I determine that above yield, the escape time of particles leaving their cages scales systematically with the value of excess entropy at later times in the shear cycle. This result indicates two conclusions. First, causality is established. Imposed stress leads to a resulting strain as we already know from rheology. The imposed strain results in a spike in particles shifting past their neighbors. These shifting motions, precipitate specific structures within the microstructure as characterized by excess entropy. Second, the average amount of mobility of the particles at any given time directly relates to the resulting structures. This implies that it may be difficult to use *a-priori* particle positions to predict long-time particle dynamics because it appears to be the case.

Chapter 4 provides a phenomenological model of a link between a material's relative elasticity and plasticity for a given oscillatory deformation. I derive from first principles an energy balance that applies to non-Brownian, amorphous suspensions.

This derivation uses a grand canonical ensemble over each cage in a system to describe yield as a transition between pressure and chemical work. With the energy balance in hand, it is possible to recover the amount of elasticity relative to plasticity for any given strain amplitude by using observations of the microstructure. Each variable in this model is measured and the relationships hold experimentally. A statistical link between bulk yield and the microstructure is reported.

These results highlight the value of the analogy between thermal and loaded a-thermal solids and that concepts borrowed from thermodynamics may be applicable. In particular, the chaotic motions and entropy of particle configurations are inextricably linked the bulk rheological response of amorphous solids.

5.2 Future recommendations

Here, I introduce project ideas that could continue the investigation of yield of amorphous solids.

Testing in 3D systems with many more constituent particles

A confocal rheometer is a classic cone and plate rheometer, but with a confocal microscope included for rapid imaging. The five channel confocal microscope is capable of constructing 3D images of particle systems by stacking 2D slices. The main challenge is in minimizing the amount of vibrations passed from the rheometer's motor to the piezoelectric device that runs the microscope's scanning. While this has been achieved a couple times before, it represents a not insignificant engineering challenge on its own. Past solutions have focused on integrating the two systems using a large visco-elastic, polymer component to damp any vibrations. Once this design process is completed, the system can be used to address a myriad of physics and biology subjects.

The yield transition is a prime example of an area that can be illuminated by the confocal rheometer. The obvious contribution would be to investigate the role of all relations mentioned throughout the thesis, but expanding to three dimensions.

While certain aspects of research may be slightly limited (the confocal's frame rate is not expected to quite match that of the Flare, the camera used with the interfacial stress rheometer), other aspects will be expanded greatly. For instance, the number of particles imaged within each system will be ~ $1,000,000$. In addition, it is possible to precisely tune attraction within 3D colloids by using depletion forces [9, 84]. With this experimental apparatus in place it will be possible to verify that all the results presented in this thesis exist in 3D as well as 2D model systems. Moreover, the role inter-particle attraction plays in colloidal systems can be expanded to rheology by exploring particle dynamics.

Aggregation dynamics as a way of probing attractive interactions

A separate experimental system to the interfacial stress rheometer introduced, allows us to explore particle dynamics across wide ranges in applied strain (both steady and oscillatory), particle packing fraction, and strength of inter-particle forces. Playfully this apparatus is called the inertial flow cell because of its ability to probe particulate fluid flows dominated by inertia instead of viscosity. During my time at the University of Pennsylvania I have had a hand in designing this system and have assembled and verified its functionality. Particles are suspended at an interface by capillary forces, but are free to move within the interfacial plain. The fluid (typically water with dissolved NaCl) is driven via Lorentz forces. These forces are generated by including an array of magnets below the cell and passing a current through the fluid. The movements of the fluid impart drag forces on the particles. Light (point source) shines through the bottom of the cell at a 45 degree angle; this angle imparts a gradient in light intensity across the cell, which would inhibit tracking of all particles. Polystyrene particles (diameters: 0.4-1.0mm), act as small, individual lenses, focusing light upward to the camera lens. To mitigate the gradient in light intensity reaching the camera sensor, I have mounted the camera at 15 degrees from vertical and set the focal plain on the particles at the center of the cell. The particles on either side of the center of the cell are therefore slightly out of focus; those below the focal plain have decreased intensity and those above have an increase. Particle trajectories are assembled via standard feature finding and linking mechanisms.

With this system it is possible to adjust the area fraction of particles being studied by simply adjusting the number of particles added. The Reynolds and Stokes numbers can be tuned by changing the concentration of NaCl added and by altering the amount of current running through the cell. Our particles are naturally hydrophobic which in combination with gravity forcing the particles downward, results in a deformed interface. It is energetically favorable for two particles with overlapping capillaries to further minimize the areas of the interface by coming closer together. (Gibbs free energy, G is the surface tension, γ multiplied by surface area, A.) Attraction results from this energetic scenario. The intensity of this attraction can be tuned by changing the surface tension. Additionally, repulsion can be introduced by charging the surfaces of the particles. These three axes of variation allow for the exploration of a huge phase space, which isn't typically available in experiments.

In the context of the yield transition, illuminating experiments with this system would explore the influence of inter-particle attraction on particle dynamics in particulate suspensions undergoing shear. Do the relations outlined above and found using the interfacial stress hheometer and simulations apply when particles are instead attracted to each other? Do they occur when particles interact with friction? A second area of geologic interest, would be to investigate how yield emerges as the dilute limit is surpassed. It is possible that the coordinated motions within the above yield behavior are in some ways similar to birth/death dynamics of aggregates in the dilute limit. This brings to mind the question, are there more generalized forms of the dynamical relationships shown above?

5.3 Perspectives

Around 55BCE, Lucretius wrote in a ferverish excitement of the implications of the void within matter in *De Natura Rerum* (The Nature of Things)[131]:

> Here I must run ahead, warn you what some wrongly declare,

Lest you be detoured from the truth. For certain people swear

That waters yield to scaly fishes nosing through and make

Liquid channels open up, since fish leave in their wake

Room for the yielding waves to flow together, so however

Full the universe, things can change places with each other.

I'll have you know this line of reasoning can have no base.

For where can scaly fishes swim if water won't give place?

And where can water flow back into if the fish can't budge?

So matter is either deprived of movement, or else we must judge

Void is enmeshed in things, and is where movement gets its start.

Periodically since ancient times people have hypothesized that the deformation of matter occurs by particles shifting within surrounding void spaces. Until relatively recently, it remained outside our abilities to confirm these hypothesis with observations or sophisticated mathematical deduction. In modern times we have confirmed that indeed elements exist within empty space and that allows for deformations. The natures of materials [192] are determined by the degree of randomized motion that those particles exhibit, the strength of their interactions, and their configurations.

We saw in the introduction that materials with particles arranged into patterns can deform smoothly in a unified manner. However, materials with constituents arranged in a random way frustrate deformation. If the strength of the interactions is low compared to the underlying thermal motions, then a material will likely be liquid and not support load.

Bibliography

[1] E. H. Abramson. Viscosity of carbon dioxide measured to a pressure of 8 gpa and temperature of 673 k. *Phys. Rev. E*, 80:021201, Aug 2009.

[2] Dan Allan, Casper van der Wel, Nathan Keim, Thomas A Caswell, Devin Wieker, Ruben Verweij, Chaz Reid, Thierry, Lars Grueter, Kieran Ramos, apiszcz, zoeith, Rebecca W Perry, François Boulogne, Prashant Sinha, pfigliozzi, Nicolas Bruot, Leonardo Uieda, Jan Katins, Hadrien Mary, and Aron Ahmadia. soft-matter/trackpy: Trackpy v0.4.2, October 2019.

[3] D.B. Allen, T. Caswell, N.C. Keim, and C.M. van der Wel. Trackpy v0.4.1. `https://zenodo.org/record/1226458`, 2018. DOI:10.5281/zenodo.1226458.

[4] J. A. Anderson, C. D. Lorenz, and A. Travesset. General purpose molecular dynamics simulations fully implemented on graphics processing units. *J. Comput. Phys.*, 227(10):5342–5359, 2008.

[5] R.S. Anderson and S.P. Anderson. *Geomorphology: The mechanics and chemistry of landscapes*. Cambridge University Press, 2010.

[6] Roberta Angelini, Emanuela Zaccarelli, Flavio Augusto de Melo Marques, Michael Sztucki, Andrei Fluerasu, Giancarlo Ruocco, and Barbara Ruzicka. Glass–glass transition during aging of a colloidal clay. *Nature Communications*, 5:4049, Jun 2014.

[7] Ansys. Material property charts, 2022. [Online; accessed 10-March-2022].

[8] A.S Argon. Plastic deformation in metallic glasses. *Acta Metal.*, 27(1):47 – 58, 1979.

[9] Sho Asakura and Fumio Oosawa. Interaction between particles suspended in solutions of macromolecules. *Journal of Polymer Science*, 33(126):183–192, 1958.

[10] R. Aveyard, B. P. Binks, J. H. Clint, P. D. I. Fletcher, T. S. Horozov, B. Neumann, V. N. Paunov, J. Annesley, S. W. Botchway, D. Nees, A. W. Parker, A. D. Ward, and A. N. Burgess. Measurement of long-range repulsive forces between charged particles at an oil-water interface. *Phys. Rev. Lett.*, 88:246102, Jun 2002.

[11] Robert Aveyard, John H. Clint, Dieter Nees, and Vesselin N. Paunov. Compression and structure of monolayers of charged latex particles at air/water and octane/water interfaces. *Langmuir*, 16(4):1969–1979, 2000.

[12] R.A. Bagnold. *The physics of blown sand and deasert dunes.* Dover, 1954.

[13] Gregory L. Baker and Jerry P. Gollub. *Chaotic Dynamics: An Introduction.* Cambridge University Press, 1996.

[14] Neil J. Balmforth, Ian A. Frigaard, and Guillaume Ovarlez. Yielding to stress: Recent developments in viscoplastic fluid mechanics. *Annual Review of Fluid Mechanics*, 46(1):121–146, 2014.

[15] V. Bapst, T. Keck, A. Grabska-Barwińska, C. Donner, E. D. Cubuk, S. S. Schoenholz, A. Obika, A. W. R. Nelson, T. Back, D. Hassabis, and P. Kohli. Unveiling the predictive power of static structure in glassy systems. *Nat. Phys.*, 16:448–454, 2020.

[16] Andras Baranyai and Denis J. Evans. Direct entropy calculation from computer simulation of liquids. *Phys. Rev. A*, 40:3817–3822, Oct 1989.

[17] Howard A. Barnes. The yield stress—a review or everything flows? *Journal of Non-Newtonian Fluid Mechanics*, 81(1):133–178, 1999.

[18] R.P. Behringer and B. Chakraborty. The physics of jamming for granular materials: a review. *Rep. Prog. Phys*, 82(1):012601, nov 2018.

[19] Ludovic Berthier, Jean-Louis Barrat, and Jorge Kurchan. A two-time-scale, two-temperature scenario for nonlinear rheology. *Phys. Rev. E*, 61:5464–5472, May 2000.

[20] Dapeng Bi, Silke Henkes, Karen E. Daniels, and Bulbul Chakraborty. The statistical physics of athermal materials. *Annu. Rev. of Condens. Matter Phys.*, 6:63–83, 2015.

[21] Ephraim S. Bililign, Jonathan E. Kollmer, and Karen E. Daniels. Protocol dependence and state variables in the force-moment ensemble. *Phys. Rev. Lett.*, 122:038001, Jan 2019.

[22] E.C. Bingham. *An Investigation of the Laws of Plastic Flow.* Number no. 278 in Bulletin of the Bureau of Standards. U.S. Government Printing Office, 1917.

[23] B. Binks and T. Horozov. *Colloidal Particles at Liquid Interfaces.* Cambridge University Press, 2006.

[24] Erik Bitzek, Pekka Koskinen, Franz Gähler, Michael Moseler, and Peter Gumbsch. Structural relaxation made simple. *Phys. Rev. Lett.*, 97:170201, Oct 2006.

[25] Elena Blanco, Daniel J. M. Hodgson, Michiel Hermes, Rut Besseling, Gary L. Hunter, Paul M. Chaikin, Michael E. Cates, Isabella Van Damme, and Wilson C. K. Poon. Conching chocolate is a prototypical transition from frictionally jammed solid to flowable suspension with maximal solid content. *PNAS*, 116(21):10303–10308, 2019.

[26] Daniel Bonn, Morton M. Denn, Ludovic Berthier, Thibaut Divoux, and Sébastien Manneville. Yield stress materials in soft condensed matter. *Rev. Mod. Phys.*, 89:035005, Aug 2017.

[27] Roger T. Bonnecaze, Fardin Khabaz, Lavanya Mohan, and Michel Cloitre. Excess entropy scaling for soft particle glasses. *J. Rheol.*, 64(2):423–431, 2020.

[28] Rajendra P. Borwankar. Food texture and rheology: A tutorial review. *Journal of Food Engineering*, 16(1):1–16, 1992. Rheology of Foods.

[29] Eran Bouchbinder and J. S. Langer. Nonequilibrium thermodynamics of driven amorphous materials. i. internal degrees of freedom and volume deformation. *Phys. Rev. E*, 80:031131, Sep 2009.

[30] Eran Bouchbinder and J. S. Langer. Nonequilibrium thermodynamics of driven amorphous materials. ii. effective-temperature theory. *Phys. Rev. E*, 80:031132, Sep 2009.

[31] Eran Bouchbinder and J. S. Langer. Nonequilibrium thermodynamics of driven amorphous materials. iii. shear-transformation-zone plasticity. *Phys. Rev. E*, 80:031133, Sep 2009.

[32] Eran Bouchbinder and J. S. Langer. Shear-transformation-zone theory of linear glassy dynamics. *Phys. Rev. E*, 83:061503, Jun 2011.

[33] Fran çois Boyer, Élisabeth Guazzelli, and Olivier Pouliquen. Unifying suspension and granular rheology. *Phys. Rev. Lett.*, 107:188301, Oct 2011.

[34] J. M. Brader, Th. Voigtmann, M. E. Cates, and M. Fuchs. Dense colloidal suspensions under time-dependent shear. *Phys. Rev. Lett.*, 98:058301, Jan 2007.

[35] Carlton F. Brooks, Gerald G. Fuller, Curtis W. Frank, and Channing R. Robertson. An interfacial stress rheometer to study rheological transitions in monolayers at the air/water interface. *Langmuir*, 15(7):2450–2459, 1999.

[36] Ivo Buttinoni, Mathias Steinacher, Hendrik Th. Spanke, Juho Pokki, Severin Bahmann, Bradley Nelson, Giuseppe Foffi, and Lucio Isa. Colloidal polycrystalline monolayers under oscillatory shear. *Phys. Rev. E*, 95:012610, Jan 2017.

[37] Herbert B. Callen. *Thermodynamics and an Introduction to Thermostatistics*. Wiley, 1991.

[38] R.J.G.B. Campello, D. Moulavi, and J. Sander. Density-based clustering based on hierarchical density estimates. In K.-Y. Whang, K. Shim J. Jeon, and J. Srivatava, editors, *Advances in Knowledge Discovery and Data Mining*, pages 160–172. Springer, 2013.

[39] Yunus Cengel, Michael Boles, and Mehmet Kanoglu. *Thermodynamics: An Engineering Approach*. McGraw-Hill Education, 2018.

[40] David Chandler. *Introduction to Modern Statistical Mechanics*. Oxford University Press, 1987.

[41] Chialu Chang, Fernando Alvarez-Nunez, Joseph Rinella, Lars-Erik Magnusson, and Katsuhiko Sueda. Roller compaction, granulation and capsule product dissolution of drug formulations containing a lactose or mannitol filler, starch, and talc. *AAPS PharmSciTech*, 9:597–604, 02 2008.

[42] Daniel T.N. Chen, Qi Wen, Paul A. Janmey, John C. Crocker, and Arjun G. Yodh. Rheology of soft materials. *Annu. Rev. of Condens. Matter Phys.*, 1(1):301–322, 2010.

[43] Ke Chen, Wouter G. Ellenbroek, Zexin Zhang, Daniel T. N. Chen, Peter J. Yunker, Silke Henkes, Carolina Brito, Olivier Dauchot, Wim van Saarloos, Andrea J. Liu, and A. G. Yodh. Low-frequency vibrations of soft colloidal glasses. *Phys. Rev. Lett.*, 105:025501, Jul 2010.

[44] Ke Chen, M. L. Manning, Peter J. Yunker, Wouter G. Ellenbroek, Zexin Zhang, Andrea J. Liu, and A. G. Yodh. Measurement of correlations be-

tween low-frequency vibrational modes and particle rearrangements in quasi-two-dimensional colloidal glasses. *Phys. Rev. Lett.*, 107:108301, Aug 2011.

[45] Xiang Cheng, Jonathan H. McCoy, Jacob N. Israelachvili, and Itai Cohen. Imaging the microscopic structure of shear thinning and thickening colloidal suspensions. *Science*, 333(6047):1276–1279, 2011.

[46] Luca Cipelletti, S. Manley, R. C. Ball, and D. A. Weitz. Universal aging features in the restructuring of fractal colloidal gels. *Phys. Rev. Lett.*, 84:2275–2278, Mar 2000.

[47] Luca Cipelletti, Kirsten Martens, and Laurence Ramos. Microscopic precursors of failure in soft matter. *Soft Matter*, 16:82–93, 2020.

[48] Wikimedia Commons. File:coralpinksanddunessand.jpg — wikimedia commons, the free media repository, 2021. [Online; accessed 10-March-2022].

[49] Wikimedia Commons. File:crystalgrain.jpg — wikimedia commons, the free media repository, 2022. [Online; accessed 10-March-2022].

[50] E. D. Cubuk, R. J. S. Ivancic, S. S. Schoenholz, D. J. Strickland, A. Basu, Z. S. Davidson, J. Fontaine, J. L. Hor, Y.-R. Huang, Y. Jiang, N. C. Keim, K. D. Koshigan, J. A. Lefever, T. Liu, X.-G. Ma, D. J. Magagnosc, E. Morrow, C. P. Ortiz, J. M. Rieser, A. Shavit, T. Still, Y. Xu, Y. Zhang, K. N. Nordstrom, P. E. Arratia, R. W. Carpick, D. J. Durian, Z. Fakhraai, D. J. Jerolmack, Daeyeon Lee, Ju Li, R. Riggleman, K. T. Turner, A. G. Yodh, D. S. Gianola, and Andrea J. Liu. Structure-property relationships from universal signatures of plasticity in disordered solids. *Science*, 358(6366):1033–1037, 2017.

[51] E. D. Cubuk, S. S. Schoenholz, J. M. Rieser, B. D. Malone, J. Rottler, D. J. Durian, E. Kaxiras, and A. J. Liu. Identifying structural flow defects in disordered solids using machine-learning methods. *Phys. Rev. Lett.*, 114:108001, Mar 2015.

[52] Pallabi Das, H. A. Vinutha, and Srikanth Sastry. Unified phase diagram of reversible–irreversible, jamming, and yielding transitions in cyclically sheared soft-sphere packings. *PNAS*, 117(19):10203–10209, 2020.

[53] Pablo G. Debenedetti and Frank H. Stillinger. Supercooled liquids and the glass transition. *Nature*, 410:259–467, 2001.

[54] Dmitry V. Denisov, Minh Triet Dang, Bernd Struth, Alessio Zaccone, and Gerard H. Wegdam. Sharp symmetry-change marks the mechanical failure transition of glasses. *Sci. Rep.*, 5:14359, 2015.

[55] D.V. Denisov, M.T. Dang, B. Struth, A. Zaccone, G.H. Wegdam, and P. Schall. Sharp symmetry-change marks the mechanical failure transition of glasses. *Sci. Rep.*, 5:14359, 2015.

[56] Nakul S. Deshpande, David J. Furbish, Paulo E. Arratia, and Douglas J. Jerolmack. The perpetual fragility of creeping hillslopes. *Nat. Comm.*, 12(1):3909, 2021.

[57] Yajun Ding and Jeetain Mittal. Equilibrium and nonequilibrium dynamics of soft sphere fluids. *Soft Matter*, 11:5274–5281, 2015.

[58] S. L. Dixon and Cesare Hall. *Fluid Mechanics and Thermodynamics of Turbomachinery*. Butterworth-Heinemann, 2013.

[59] Jacek Dudowicz, Karl F. Freed, and Jack F. Douglas. *Generalized Entropy Theory of Polymer Glass Formation*, chapter 3, pages 125–222. John Wiley & Sons, Ltd, 2007.

[60] Jeppe C. Dyre. Hidden scale invariance in condensed matter. *The Journal of Physical Chemistry B*, 118(34):10007–10024, 2014. PMID: 25011702.

[61] Jeppe C. Dyre. Perspective: Excess-entropy scaling. *J. Chem. Phys.*, 149(21):210901, 2018.

[62] Mikhail Dzugutov. A universal scaling law for atomic diffusion in condensed matter. *Nature*, 381:137–139, 1996.

[63] S.F. Edwards and R.B.S. Oakeshott. Theory of powders. *Physica A: Statistical Mechanics and its Applications*, 157(3):1080–1090, 1989.

[64] Emily Elhacham, Liad Ben-Uri, Jonathan Grozovski, Yinon M. Bar-On, and Ron Milo. Global human-made mass exceeds all living biomass. *Nature*, 588(7838):442–444, 2020.

[65] Olaf Engler and Jürgen Hirsch. Texture control by thermomechanical processing of aa6xxx al–mg–si sheet alloys for automotive applications—a review. *Materials Science and Engineering: A*, 336(1):249 – 262, 2002.

[66] M. L. Falk and J. S. Langer. Dynamics of viscoplastic deformation in amorphous solids. *Phys. Rev. E*, 57:7192–7205, Jun 1998.

[67] Michael L. Falk and J.S. Langer. Deformation and failure of amorphous, solid-like materials. *Annu. Rev. Condens. Matter Phys.*, 2(1):353–373, 2011.

[68] Behrooz Ferdowsi, Carlos P. Ortiz, and Douglas J. Jerolmack. Glassy dynamics of landscape evolution. *Proceedings of the National Academy of Sciences*, 115(19):4827–4832, 2018.

[69] Davide Fiocco, Giuseppe Foffi, and Srikanth Sastry. Encoding of memory in sheared amorphous solids. *Phys. Rev. Lett.*, 112:025702, Jan 2014.

[70] Sean Fitzgibbon, Eric S. G. Shaqfeh, Gerald G. Fuller, and Travis W. Walker. Scaling analysis and mathematical theory of the interfacial stress rheometer. *Journal of Rheology*, 58(4):999–1038, 2014.

[71] Derek Frydel and Martin Oettel. Charged particles at fluid interfaces as a probe into structural details of a double layer. *Phys. Chem. Chem. Phys.*, 13:4109–4118, 2011.

[72] Matthias Fuchs. *Nonlinear Rheological Properties of Dense Colloidal Dispersions Close to a Glass Transition Under Steady Shear*, pages 55–115. Springer Berlin Heidelberg, Berlin, Heidelberg, 2010.

[73] F. Gadala-Maria and Andreas Acrivos. Shear-induced structure in a concentrated suspension of solid spheres. *J. Rheol.*, 24(6):799–814, 1980.

[74] Paula A. Gago and Stefan Boettcher. Universal features of annealing and aging in compaction of granular piles. *Proceedings of the National Academy of Sciences*, 117(52):33072–33076, 2020.

[75] K. L. Galloway, E. G. Teich, X. G. Ma, Ch. Kammer, I. R. Graham, N. C. Keim, C. Reina, D. J. Jerolmack, A. G. Yodh, and P. E. Arratia. Relationships between structure, memory and flow in sheared disordered materials. *Nat. Phys.*, 2022.

[76] K. Lawrence Galloway, Douglas J. Jerolmack, and Paulo E. Arratia. Quantification of plasticity via particle dynamics above and below yield in a 2d jammed suspension. *Soft Matter*, 16:4373–4382, 2020.

[77] K. Lawrence Galloway, Xiaoguang Ma, Nathan C. Keim, Douglas J. Jerolmack, Arjun G. Yodh, and Paulo E. Arratia. Scaling of relaxation and excess entropy in plastically deformed amorphous solids. *Proceedings of the National Academy of Sciences*, 117(22):11887–11893, 2020.

[78] Jens Glaser, Trung Dac Nguyen, Joshua A. Anderson, Pak Lui, Filippo Spiga, Jaime A. Millan, David C. Morse, and Sharon C. Glotzer. Strong scaling of general-purpose molecular dynamics simulations on gpus. *Comput. Phys. Commun.*, 192:97 – 107, 2015.

[79] Nicoletta Gnan, Thomas B. Schrøder, Ulf R. Pedersen, Nicholas P. Bailey, and Jeppe C. Dyre. Pressure-energy correlations in liquids. iv. “isomorphs” in liquid phase diagrams. *The Journal of Chemical Physics*, 131(23):234504, 2009.

[80] Nicoletta Gnan and Emanuela Zaccarelli. The microscopic role of deformation in the dynamics of soft colloids. *Nature Physics*, 15(7):683, 2019.

[81] Oscar Gonzalez and Andrew M. Stuart. *A First Course in Continuum Mechanics*. Cambridge Texts in Applied Mathematics. Cambridge University Press, 2008.

[82] A. D. Gopal and D. J. Durian. Nonlinear bubble dynamics in a slowly driven foam. *Phys. Rev. Lett.*, 75:2610–2613, Sep 1995.

[83] W. Götze. *Complex Dynamics of Glass-Forming Liquids: A Mode-Coupling Theory*. Oxford University Press, New York, 2008.

[84] Matthew D. Gratale, Tim Still, Caitlin Matyas, Zoey S. Davidson, Samuel Lobel, Peter J. Collings, and A. G. Yodh. Tunable depletion potentials driven by shape variation of surfactant micelles. *Phys. Rev. E*, 93:050601, May 2016.

[85] Élisabeth Guazzelli and Olivier Pouliquen. Rheology of dense granular suspensions. *J. Fluid Mech.*, 852:P1, 2018.

[86] James E. Hallett, Francesco Turci, and C. Patrick Royall. Local structure in deeply supercooled liquids exhibits growing lengthscales and dynamical correlations. *Nat. Commun.*, 9:1–10, 2018.

[87] Toshiyuki Hamanaka, Hayato Shiba, and Akira Onuki. Plastic flow in polycrystal states in a binary mixture. *Phys. Rev. E*, 77:042501, Apr 2008.

[88] Thomas K. Haxton. Ratio of effective temperature to pressure controls the mobility of sheared hard spheres. *Phys. Rev. E*, 85:011503, Jan 2012.

[89] Donald Haynie. *Biological Thermodynamics*. Cambridge University Press, 2008.

[90] Terrell L. Hill. Thermodynamics of small systems. *The Journal of Chemical Physics*, 36(12):3182–3197, 1962.

[91] K. Hima Nagamanasa, Shreyas Gokhale, A. K. Sood, and Rajesh Ganapathy. Publisher's note: Experimental signatures of a nonequilibrium phase transition governing the yielding of a soft glass [phys. rev. e 89, 062308 (2014)]. *Phys. Rev. E*, 90:049904, Oct 2014.

[92] M. Houssais, C. P. Ortiz, D. J. Durian, and D. J. Jerolmack. Rheology of sediment transported by a laminar flow. *Phys. Rev. E*, 94:062609, Dec 2016.

[93] M. Houssais, C.P. Ortiz, D.J. Durian, and D.J. Jerolmack. Onset of sediment transport is a continuous transition driven by fluid shear and granular creep. *Nat. Commun.*, 6:6527, 2015.

[94] J. J. Hoyt, M. Asta, and B. Sadigh. Test of the universal scaling law for the diffusion coefficient in liquid metals. *Phys. Rev. Lett.*, 85:594–597, Jul 2000.

[95] A J Hurd. The electrostatic interaction between interfacial colloidal particles. *Journal of Physics A: Mathematical and General*, 18(16):L1055–L1060, nov 1985.

[96] Trond S. Ingebrigtsen and Hajime Tanaka. Structural predictor for nonlinear sheared dynamics in simple glass-forming liquids. *PNAS*, 115(1):87–92, 2018.

[97] Katerina Ioannidou, Konrad J. Krakowiak, Mathieu Bauchy, Christian G. Hoover, Enrico Masoero, Sidney Yip, Franz-Josef Ulm, Pierre Levitz, Roland J.-M. Pellenq, and Emanuela Del Gado. Mesoscale texture of cement hydrates. *PNAS*, 113(8):2029–2034, 2016.

[98] Jacob N Israelachvili. *Intermolecular and Surface Forces*. Academic Press, 2011.

[99] Ted Jacobson. Thermodynamics of spacetime: The einstein equation of state. *Phys. Rev. Lett.*, 75:1260–1263, Aug 1995.

[100] Liesbeth M. C. Janssen. Mode-coupling theory of the glass transition: A primer. *Front. Phys.*, 6, Oct 2018.

[101] Douglas J. Jerolmack and Karen E. Daniels. Viewing earth's surface as a soft-matter landscape. *Nat. Rev. Phys.*, 1:716–730, 2019.

[102] Jiali Jiang, Bachtiar Erik Valentine, Jianxiong Lu, and Peter Niemz. Time dependence of the orthotropic compression young's moduli and poisson's ratios of chinese fir wood. *Holzforschung*, 70(11):1093–1101, 2016.

[103] H. Katsuragi, A. R. Abate, and D. J. Durian. Jamming and growth of dynamical heterogeneities versus depth for granular heap flow. *Soft Matter*, 6:3023–3029, 2010.

[104] Takeshi Kawasaki and Ludovic Berthier. Macroscopic yielding in jammed solids is accompanied by a nonequilibrium first-order transition in particle trajectories. *Phys. Rev. E*, 94:022615, Aug 2016.

[105] Nathan C. Keim and Paulo E. Arratia. Yielding and microstructure in a 2d jammed material under shear deformation. *Soft Matter*, 9:6222–6225, 2013.

[106] Nathan C. Keim and Paulo E. Arratia. Mechanical and microscopic properties of the reversible plastic regime in a 2d jammed material. *Phys. Rev. Lett.*, 112:028302, Jan 2014.

[107] Nathan C. Keim and Paulo E. Arratia. Role of disorder in finite-amplitude shear of a 2d jammed material. *Soft Matter*, 11:1539–1546, 2015.

[108] Nathan C. Keim, Jacob Hass, Brian Kroger, and Devin Wieker. Global memory from local hysteresis in an amorphous solid. *Phys. Rev. Research*, 2:012004, Jan 2020.

[109] Nathan C. Keim and Sidney R. Nagel. Generic transient memory formation in disordered systems with noise. *Phys. Rev. Lett.*, 107:010603, Jun 2011.

[110] Nathan C. Keim, Joseph D. Paulsen, and Sidney R. Nagel. Multiple transient memories in sheared suspensions: Robustness, structure, and routes to plasticity. *Phys. Rev. E*, 88:032306, Sep 2013.

[111] Nathan C. Keim, Joseph D. Paulsen, Zorana Zeravcic, Srikanth Sastry, and Sidney R. Nagel. Memory formation in matter. *Rev. Mod. Phys.*, 91:035002, Jul 2019.

[112] Fardin Khabaz and Roger T. Bonnecaze. Thermodynamics of shear-induced phase transition of polydisperse soft particle glasses. *Physics of Fluids*, 33(1):013315, 2021.

[113] Fardin Khabaz, Michel Cloitre, and Roger T. Bonnecaze. Particle dynamics predicts shear rheology of soft particle glasses. *J. Rheol.*, 64(2):459–468, 2020.

[114] T. R. Kirkpatrick, D. Thirumalai, and P. G. Wolynes. Scaling concepts for the dynamics of viscous liquids near an ideal glassy state. *Phys. Rev. A*, 40:1045–1054, Jul 1989.

[115] Teruhisa S. Komatsu, Shio Inagaki, Naoko Nakagawa, and Satoru Nasuno. Creep motion in a granular pile exhibiting steady surface flow. *Phys. Rev. Lett.*, 86:1757–1760, Feb 2001.

[116] D. Kondepudi and I. Prigogine. *Modern thermodynamics, From heat engines to dissipative structures.* John Wiley & Sons, 1998.

[117] Peter A. Kralchevsky and Kuniaki Nagayama. Capillary interactions between particles bound to interfaces, liquid films and biomembranes. *Advances in Colloid and Interface Science*, 85(2):145 – 192, 2000.

[118] W. P. Krekelberg, M. J. Pond, G. Goel, V. K. Shen, J. R. Errington, and T. M. Truskett. Generalized rosenfeld scalings for tracer diffusivities in not-so-simple fluids: Mixtures and soft particles. *Phys. Rev. E*, 80:061205, Dec 2009.

[119] William P. Krekelberg, Venkat Ganesan, and Thomas M. Truskett. Shear-rate-dependent structural order and viscosity of a fluid with short-range attractions. *Phys. Rev. E*, 78:010201, Jul 2008.

[120] William P. Krekelberg, Venkat Ganesan, and Thomas M. Truskett. Structural signatures of mobility on intermediate time scales in a supercooled fluid. *The Journal of Chemical Physics*, 132(18):184503, 2010.

[121] L. D. Landau and E.M. Lifshitz. *Statistical physics / by L.D. Landau and E.M. Lifshitz ; translated from the Russian by J.R. Sykes and M.J. Kearsley.* Their Course of theoretical physics ; v.5. Pergamon Press, 2nd ed. edition, 1969.

[122] R.G. Larson. *The structure and rheology of complex fluids.* Oxford University Press, 2010.

[123] Adam D. Law, Mélodie Auriol, Dean Smith, Tommy S. Horozov, and D. Martin A. Buzza. Self-assembly of two-dimensional colloidal clusters by tuning the hydrophobicity, composition, and packing geometry. *Phys. Rev. Lett.*, 110:138301, Mar 2013.

[124] Mathieu Leocmach, John Russo, and Hajime Tanaka. Importance of many-body correlations in glass transition: An example from polydisperse hard spheres. *J. Chem. Phys.*, 138(12):12A536, 2013.

[125] Bo Li, Xiuming Xiao, Kai Lou, Shuxia Wang, Weijia Wen, and Ziren Wang. Breakdown of diffusivity-entropy scaling in colloidal glass-forming liquids. *Communications Physics*, 1(1):79, 2018.

[126] A. Liu and S. Nagel. Jamming is not just cool anymore. *Nature*, 396:21–22, 1998.

[127] Andrea J. Liu and Sidney R. Nagel. The jamming transition and the marginally jammed solid. *Annu. Rev. Condens. Matter Phys.*, 1(1):347–369, 2010.

[128] Y. Z. Lu, M. Q. Jiang, X. Lu, Z. X. Qin, Y. J. Huang, and J. Shen. Dilatancy of shear transformations in a colloidal glass. *Phys. Rev. Applied*, 9:014023, Jan 2018.

[129] Z. P. Lu, C. T. Liu, J. R. Thompson, and W. D. Porter. Structural amorphous steels. *Phys. Rev. Lett.*, 92:245503, Jun 2004.

[130] Vassiliy Lubchenko. Shear thinning in deeply supercooled melts. *Proceedings of the National Academy of Sciences*, 106(28):11506–11510, 2009.

[131] Titus Lucretius and Alicia Stallings. *De Rerum Natura.* Penguin Classics, 2007.

[132] Micah Lundberg, Kapilanjan Krishan, Ning Xu, Corey S. O'Hern, and Michael Dennin. Reversible plastic events in amorphous materials. *Phys. Rev. E*, 77:041505, Apr 2008.

[133] Xiaoguang Ma, Wei Chen, Ziren Wang, Yuan Peng, Yilong Han, and Penger Tong. Test of the universal scaling law of diffusion in colloidal monolayers. *Phys. Rev. Lett.*, 110:078302, Feb 2013.

[134] Xiaoguang Ma, Zoey S. Davidson, Tim Still, Robert J. S. Ivancic, S. S. Schoenholz, A. J. Liu, and A. G. Yodh. Heterogeneous activation, local structure, and softness in supercooled colloidal liquids. *Phys. Rev. Lett.*, 122:028001, Jan 2019.

[135] Xiaoguang Ma, Jiachen Liu, Yikang Zhang, Piotr Habdas, and A. G. Yodh. Excess entropy and long-time diffusion in colloidal fluids with short-range interparticle attraction. *The Journal of Chemical Physics*, 150(14):144907, 2019.

[136] Christopher W. Macosko. *Rheology: Principles, Measurements, and Applications.* Wiley-VCH, 1996.

[137] Anders Madsen, Robert L Leheny, Hongyu Guo, Michael Sprung, and Orsolya Czakkel. Beyond simple exponential correlation functions and equilibrium dynamics in x-ray photon correlation spectroscopy. *New Journal of Physics*, 12(5):055001, may 2010.

[138] Armando Maestro and Alessio Zaccone. Nonaffine deformation and tunable yielding of colloidal assemblies at the air–water interface. *Nanoscale*, 9:18343–18351, 2017.

[139] M. L. Manning and A. J. Liu. Vibrational modes identify soft spots in a sheared disordered packing. *Phys. Rev. Lett.*, 107:108302, Aug 2011.

[140] L.M. Martinez and C. A. Angell. A thermodynamic connection to the fragility of glass-forming liquids. *Nature*, 410:663–667, 2001.

[141] D El Masri, M Pierno, L Berthier, and L Cipelletti. Ageing and ultra-slow equilibration in concentrated colloidal hard spheres. *Journal of Physics: Condensed Matter*, 17(45):S3543–S3549, oct 2005.

[142] Kasper Masschaele, Bum Jun Park, Eric M. Furst, Jan Fransaer, and Jan Vermant. Finite ion-size effects dominate the interaction between charged colloidal particles at an oil-water interface. *Phys. Rev. Lett.*, 105:048303, Jul 2010.

[143] Sylvain Mazoyer, Luca Cipelletti, and Laurence Ramos. Direct-space investigation of the ultraslow ballistic dynamics of a soft glass. *Phys. Rev. E*, 79:011501, Jan 2009.

[144] L. McInnes and J. Healy. Accelerated hierarchical density based clustering. In *2017 IEEE International Conference on Data Mining Workshops (ICDMW)*, pages 33–42. IEEE, 2017.

[145] G.H. McKinley. A hitchhiker's guide to complex fluids, 2015.

[146] Donald A. McQuarrie. *Statistical Mechanics*. Harper and Row, 1976.

[147] J. Mittal, J. R. Errington, and T. M. Truskett. Thermodynamics predicts how confinement modifies the dynamics of the equilibrium hard-sphere fluid. *Phys. Rev. Lett.*, 96:177804, May 2006.

[148] Raymond D. Mountain and Harold J. Raveché. Entropy and molecular correlation functions in open systems. ii two- and three-body correlations. *The Journal of Chemical Physics*, 55(5):2250–2255, 1971.

[149] Srimayee Mukherji, Neelima Kandula, A.K. Sood, and Rajesh Ganapathy. Strength of mechanical memories is maximal at the yield point of a soft glass. *Phys. Rev. Lett.*, 122(15), Apr 2019.

[150] Muhittin Mungan, Srikanth Sastry, Karin Dahmen, and Ido Regev. Networks and hierarchies: How amorphous materials learn to remember. *Phys. Rev. Lett.*, 123:178002, Oct 2019.

[151] Bruce Munson, Donald Young, Theodore Okiishi, and Wade Huebsch. *Fundamentals of Fluid Mechanics.* John Wiley & Sons, 2013.

[152] Ronny Möbius and Claus Heussinger. (ir)reversibility in dense granular systems driven by oscillating forces. *Soft Matter*, 10:4806–4812, 2014.

[153] Sidney R. Nagel. Experimental soft-matter science. *Rev. Mod. Phys.*, 89:025002, Apr 2017.

[154] Alexandre Nicolas, Ezequiel E. Ferrero, Kirsten Martens, and Jean-Louis Barrat. Deformation and flow of amorphous solids: Insights from elastoplastic models. *Rev. Mod. Phys.*, 90:045006, Dec 2018.

[155] S. Nie, Q. Jiang, L. Cui, and C. Zhang. Investigation on solid-liquid transition of soft mud under steady and oscillatory shear loads. *Sediment. Geol.*, 397:105570, 2020.

[156] Luhui Ning, Peng Liu, Yiwu Zong, Rui Liu, Mingcheng Yang, and Ke Chen. Universal scaling law for colloidal diffusion in complex media. *Phys. Rev. Lett.*, 122:178002, May 2019.

[157] M. Oettel and S. Dietrich. Colloidal interactions at fluid interfaces. *Langmuir*, 24(4):1425–1441, 2008.

[158] Ian K. Ono, Corey S. O'Hern, D. J. Durian, Stephen A. Langer, Andrea J. Liu, and Sidney R. Nagel. Effective temperatures of a driven system near jamming. *Phys. Rev. Lett.*, 89:095703, Aug 2002.

[159] Misaki Ozawa, Ludovic Berthier, Giulio Biroli, Alberto Rosso, and Gilles Tarjus. Random critical point separates brittle and ductile yielding transitions in amorphous materials. *PNAS*, 115(26):6656–6661, 2018.

[160] Tomasz Ozyhar, Stefan Hering, and Peter Niemz. Viscoelastic characterization of wood: Time dependence of the orthotropic compliance in tension and compression. *Journal of Rheology*, 57(2):699–717, 2013.

[161] Bum Jun Park, John P. Pantina, Eric M. Furst, Martin Oettel, Sven Reynaert, and Jan Vermant. Direct measurements of the effects of salt and surfactant on interaction forces between colloidal particles at water/oil interfaces. *Langmuir*, 24(5):1686–1694, 2008. PMID: 18201109.

[162] Bum Jun Park, Jan Vermant, and Eric M. Furst. Heterogeneity of the electrostatic repulsion between colloids at the oil/water interface. *Soft Matter*, 6:5327–5333, 2010.

[163] Bum Jun Park, Jan Vermant, and Eric M. Furst. Heterogeneity of the electrostatic repulsion between colloids at the oil–water interface. *Soft Matter*, 6:5327–5333, 2010.

[164] F. Parsi and F. Gadala-Maria. Fore-and-aft asymmetry in a concentrated suspension of solid spheres. *J. Rheol.*, 31(8):725–732, 1987.

[165] Nidhi Pashine, Daniel Hexner, Andrea J. Liu, and Sidney R. Nagel. Directed aging, memory, and nature's greed. *Sci. Adv.*, 5(12), 2019.

[166] Sylvain Patinet, Armand Barbot, Matthias Lerbinger, Damien Vandembroucq, and Anaël Lemaitre. Origin of the bauschinger effect in amorphous solids. *Phys. Rev. Lett.*, 124:205503, May 2020.

[167] Sylvain Patinet, Damien Vandembroucq, and Michael L. Falk. Connecting local yield stresses with plastic activity in amorphous solids. *Phys. Rev. Lett.*, 117:045501, Jul 2016.

[168] Joseph D. Paulsen, Nathan C. Keim, and Sidney R. Nagel. Multiple transient memories in experiments on sheared non-brownian suspensions. *Phys. Rev. Lett.*, 113:068301, Aug 2014.

[169] Nathan Perchikov and Eran Bouchbinder. Variable-amplitude oscillatory shear response of amorphous materials. *Phys. Rev. E*, 89:062307, Jun 2014.

[170] Nikolay Perunov, Robert A. Marsland, and Jeremy L. England. Statistical physics of adaptation. *Phys. Rev. X*, 6:021036, Jun 2016.

[171] K. N. Pham, G. Petekidis, D. Vlassopoulos, S. U. Egelhaaf, W. C. K. Poon, and P. N. Pusey. Yielding behavior of repulsion- and attraction-dominated colloidal glasses. *J. Rheol.*, 52(2):649–676, 2008.

[172] Pawel Pieranski. Two-dimensional interfacial colloidal crystals. *Phys. Rev. Lett.*, 45:569–572, Aug 1980.

[173] D. J. Pine, J. P. Gollub, J. F. Brady, and A. M. Leshansky. Chaos and threshold for irreversibility in sheared suspensions. *Nature*, 438:997–1000, 2005.

[174] Steve Plimpton. Fast parallel algorithms for short-range molecular dynamics. Technical report, Sandia National Labs., Albuquerque, NM (United States), 1993.

[175] M. J. Pond, J. R. Errington, and T. M. Truskett. Communication: Generalizing rosenfeld's excess-entropy scaling to predict long-time diffusivity in dense fluids of brownian particles: From hard to ultrasoft interactions. *The Journal of Chemical Physics*, 134(8):081101, 2011.

[176] Nikolai V. Priezjev. Heterogeneous relaxation dynamics in amorphous materials under cyclic loading. *Physical Review E*, 87(5), May 2013.

[177] Ilya Prigogine. Time, structure, and fluctuations. *Science*, 201(4358):777–785, 1978.

[178] Ilya Prigogine. *The End of Certainty.* Free Press, 1997.

[179] Harold J. Raveché. Entropy and molecular correlation functions in open systems. i. derivation. *The Journal of Chemical Physics*, 55(5):2242–2250, 1971.

[180] I. Regev, J Weber, C Reichhardt, K.A. Dahmen, and T. Lookman. Reversibility and criticality in amorphous solids. *Nat. Commun.*, 6:8805, 2014.

[181] Ido Regev, Turab Lookman, and Charles Reichhardt. Onset of irreversibility and chaos in amorphous solids under periodic shear. *Phys. Rev. E*, 88:062401, Dec 2013.

[182] Sven Reynaert, Carlton F. Brooks, Paula Moldenaers, Jan Vermant, and Gerald G. Fuller. Analysis of the magnetic rod interfacial stress rheometer. *J. Rheol.*, 52(1):261–285, 2008.

[183] Sven Reynaert, Paula Moldenaers, and Jan Vermant. Control over colloidal aggregation in monolayers of latex particles at the oil/water interface. *Langmuir*, 22(11):4936–4945, 2006. PMID: 16700578.

[184] James Rhodest and Domingo Carreira. Prediction of creep, shrinkage, and temperature effects in concrete structures. 1997.

[185] D. Richard, M. Ozawa, S. Patinet, E. Stanifer, B. Shang, S. A. Ridout, B. Xu, G. Zhang, P. K. Morse, J.-L. Barrat, L. Berthier, M. L. Falk, P. Guan, A. J. Liu, K. Martens, S. Sastry, D. Vandembroucq, E. Lerner, and M. L. Manning. Predicting plasticity in disordered solids from structural indicators. *Phys. Rev. Materials*, 4:113609, Nov 2020.

[186] Frank Rietz, Charles Radin, Harry L. Swinney, and Matthias Schröter. Nucleation in sheared granular matter. *Phys. Rev. Lett.*, 120:055701, Feb 2018.

[187] Yaakov Rosenfeld. Relation between the transport coefficients and the internal entropy of simple systems. *Phys. Rev. A*, 15:2545–2549, Jun 1977.

[188] Yaakov Rosenfeld. A quasi-universal scaling law for atomic transport in simple fluids. *J. Phys. Condens. Matter*, 11(28):5415–5427, jan 1999.

[189] Jenn Stroud Rossmann, Clive L. Dym, and Lori Bassman. *Introduction to Engineering Mechanics: A Continuum Approach.* CRC Press, 2015.

[190] A. Samanta, Sk. M. Ali, and S. K. Ghosh. Universal scaling laws of diffusion in a binary fluid mixture. *Phys. Rev. Lett.*, 87:245901, Nov 2001.

[191] Alok Samanta, Sk. Musharaf Ali, and Swapan K. Ghosh. New universal scaling laws of diffusion and kolmogorov-sinai entropy in simple liquids. *Phys. Rev. Lett.*, 92:145901, Apr 2004.

[192] Jim Schaffer. *Nature of Engineering Material.* Lafayette College, 2010.

[193] Peter Schall, David A. Weitz, and Frans Spaepen. Structural rearrangements that govern flow in colloidal glasses. *Science*, 318(5858):1895–1899, 2007.

[194] S. S. Schoenholz, E. D. Cubuk, D. M. Sussman, E. Kaxiras, and A. J. Liu. A structural approach to relaxation in glassy liquids. *Nature Physics*, 12:469–471, 2016.

[195] Samuel S. Schoenholz, Ekin D. Cubuk, Efthimios Kaxiras, and Andrea J. Liu. Relationship between local structure and relaxation in out-of-equilibrium glassy systems. *PNAS*, 114(2):263–267, 2017.

[196] Carl F. Schreck, Robert S. Hoy, Mark D. Shattuck, and Corey S. O'Hern. Particle-scale reversibility in athermal particulate media below jamming. *Phys. Rev. E*, 88:052205, Nov 2013.

[197] Eric M. Schwen, Meera Ramaswamy, Chieh-Min Cheng, Linda Jan, and Itai Cohen. Embedding orthogonal memories in a colloidal gel through oscillatory shear. *Soft Matter*, 16:3746–3752, 2020.

[198] F. Sciortino, W. Kob, and P. Tartaglia. Inherent structure entropy of supercooled liquids. *Phys. Rev. Lett.*, 83:3214–3217, Oct 1999.

[199] Leila Separdar, Nicholas P. Bailey, Thomas B. Schrøder, Saeid Davatolhagh, and Jeppe C. Dyre. Isomorph invariance of couette shear flows simulated by the sllod equations of motion. *The Journal of Chemical Physics*, 138(15):154505, 2013.

[200] Jyoti R. Seth, Lavanya Mohan, Clémentine Locatelli-Champagne, Michel Cloitre, and Roger T. Bonnecaze. A micromechanical model to predict the flow of soft particle glasses. *Nature Materials*, 10(11):838–843, 2011.

[201] Jyoti R. Seth, Lavanya Mohan, Clémentine Locatelli-Champagne, Michel Cloitre, and Roger T. Bonnecaze. A micromechanical model to predict the flow of soft particle glasses. *Nat. Mater.*, 10:838–843, 2011.

[202] G.T. Shahin. *The stress deformation interfacial rheometer.* Ph.D. thesis, University of Pennsylvania, 1986.

[203] C. E. Shannon. A mathematical theory of communication. *The Bell System Technical Journal*, 27(3):379–423, 1948.

[204] Hayato Shiba and Akira Onuki. Plastic deformations in crystal, polycrystal, and glass in binary mixtures under shear: Collective yielding. *Phys. Rev. E*, 81:051501, May 2010.

[205] Miriam Siebenbürger, Matthias Fuchs, Henning Winter, and Matthias Ballauff. Viscoelasticity and shear flow of concentrated, noncrystallizing colloidal suspensions: Comparison with mode-coupling theory. *J. Rheol.*, 53(3):707–726, 2009.

[206] Joseph H. Simmons, Robert K. Mohr, and C. J. Montrose. Non-newtonian viscous flow in glass. *Journal of Applied Physics*, 53(6):4075–4080, 1982.

[207] Steven Slotterback, Mitch Mailman, Krisztian Ronaszegi, Martin van Hecke, Michelle Girvan, and Wolfgang Losert. Onset of irreversibility in cyclic shear of granular packings. *Phys. Rev. E*, 85:021309, Feb 2012.

[208] Vaclav Smil. *Energy and Civilization a History.* MIT Press, 2017.

[209] Edward J. Stancik and Gerald G. Fuller. Connect the drops: Using solids as adhesives for liquids. *Langmuir*, 20(12):4805–4808, 2004. PMID: 15984234.

[210] Edward J. Stancik, Grant T. Gavranovic, Martin J. O. Widenbrant, Alex T. Laschitsch, Jan Vermant, and Gerald G. Fuller. Structure and dynamics of particle monolayers at a liquid–liquid interface subjected to shear flow. *Faraday Discuss.*, 123:145–156, 2003.

[211] S.H. Strogatz. *Nonlinear dynamics and chaos.* Perseus Books, 1994.

[212] Yonghao Sun, Amadeu Concustell, and A. Lindsay Greer. Thermomechanical processing of metallic glasses: extending the range of the glassy state. *Nature Reviews Materials*, 1(9):16039, 2016.

[213] Daniel M. Sussman, Samuel S. Schoenholz, Ekin D. Cubuk, and Andrea J. Liu. Disconnecting structure and dynamics in glassy thin films. *PNAS*, 114(40):10601–10605, 2017.

[214] J. Tajuelo, J. M. Pastor, and M. A. Rubio. A magnetic rod interfacial shear rheometer driven by a mobile magnetic trap. *Journal of Rheology*, 60(6):1095–1113, 2016.

[215] Elisa Tamborini, Luca Cipelletti, and Laurence Ramos. Plasticity of a colloidal polycrystal under cyclic shear. *Phys. Rev. Lett.*, 113:078301, Aug 2014.

[216] Hajime Tanaka, Takeshi Kawasaki, Hiroshi Shintani, and Keiji Watanabe. Critical-like behaviour of glass-forming liquids. *Nature Materials*, 9(4):324–331, 2010.

[217] Erin G. Teich, K.L. Galloway, Paulo E. Arratia, and Danielle S. Bassett. Crystalline shielding mitigates structural rearrangement and localizes memory in jammed systems under oscillatory shear. *Science Advances*, 7(20), 2021.

[218] Brian P. Tighe, Adrianne R. T. van Eerd, and Thijs J. H. Vlugt. Entropy maximization in the force network ensemble for granular solids. *Phys. Rev. Lett.*, 100:238001, Jun 2008.

[219] Brian P Tighe and Thijs J H Vlugt. Stress fluctuations in granular force networks. *J. Stat.*, 2011(04):P04002, apr 2011.

[220] M van Hecke. Jamming of soft particles: geometry, mechanics, scaling and isostaticity. *J. Phys. Condens.*, 22(3):033101, dec 2009.

[221] J Vermant and M J Solomon. Flow-induced structure in colloidal suspensions. *J. Phys. Condens.*, 17(4):R187–R216, jan 2005.

[222] Tom Verwijlen, Paula Moldenaers, Howard A. Stone, and Jan Vermant. Study of the flow field in the magnetic rod interfacial stress rheometer. *Langmuir*, 27(15):9345–9358, 2011.

[223] Duane C. Wallace. On the role of density fluctuations in the entropy of a fluid. *The Journal of Chemical Physics*, 87(4):2282–2284, 1987.

[224] C.-H. Wang, S.-H. Yu, and P. Chen. Universal scaling laws of diffusion in two-dimensional granular liquids. *Phys. Rev. E*, 91:060201, Jun 2015.

[225] J. G. Wang, Y. C. Hu, P. F. Guan, K. K. Song, L. Wang, G. Wang, Y. Pan, B. Sarac, and J. Eckert. Hardening of shear band in metallic glass. *Scientific Reports*, 7:7076, 2017.

[226] Ziren Wang, Ahmed M. Alsayed, Arjun G. Yodh, and Yilong Han. Two-dimensional freezing criteria for crystallizing colloidal monolayers. *The Journal of Chemical Physics*, 132(15):154501, 2010.

[227] John D. Weeks, David Chandler, and Hans C. Andersen. Role of repulsive forces in determining the equilibrium structure of simple liquids. *The Journal of Chemical Physics*, 54(12):5237–5247, 1971.

[228] Michael Widom, Katherine J Strandburg, and Robert H Swendsen. Quasicrystal equilibrium state. *Phys. Rev. Lett.*, 58(7):706, 1987.

[229] Xiaoyu Xia and Peter G. Wolynes. Fragilities of liquids predicted from the random first order transition theory of glasses. *PNAS*, 97(7):2990–2994, 2000.

[230] Ning Xu, Matthieu Wyart, Andrea J. Liu, and Sidney R. Nagel. Excess vibrational modes and the boson peak in model glasses. *Phys. Rev. Lett.*, 98:175502, Apr 2007.

[231] Ryoichi Yamamoto and Akira Onuki. Dynamics of highly supercooled liquids: Heterogeneity, rheology, and diffusion. *Phys. Rev. E*, 58:3515–3529, Sep 1998.

[232] Peter J. Yunker, Ke Chen, Zexin Zhang, and A. G. Yodh. Phonon spectra, nearest neighbors, and mechanical stability of disordered colloidal clusters with attractive interactions. *Phys. Rev. Lett.*, 106:225503, Jun 2011.